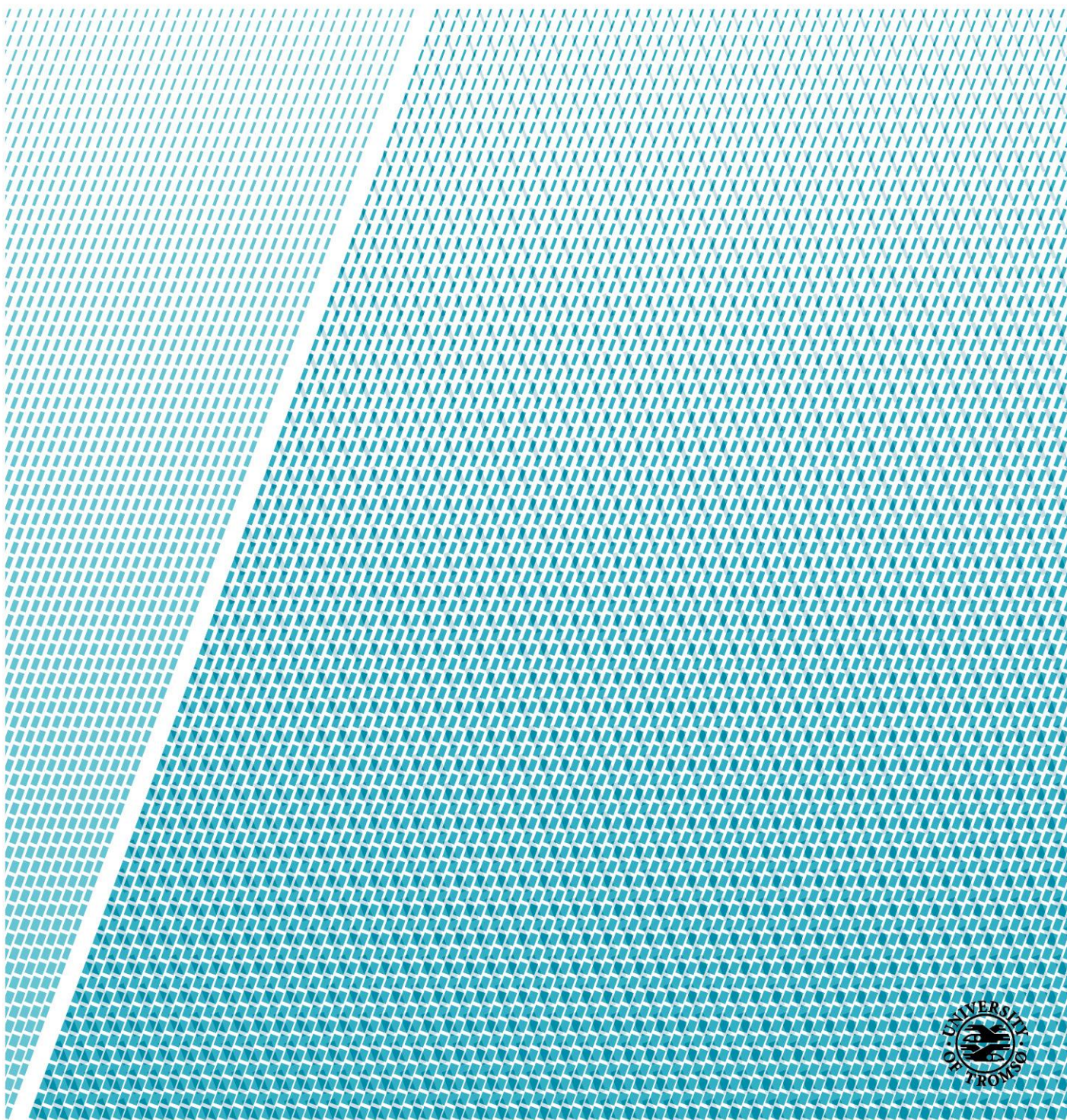


# Combining the Polarizable Continuum Model with Multiresolution analysis: a cavity-free approach to solvent effects

—  
Gabriel Adolfo Gerez Sazo

*KJE-3907 Master's thesis in chemistry and education, year 8–13 – June 2019*







# Contents

<b>Aknowledgements</b>	<b>v</b>
<b>1 Introduction</b>	<b>1</b>
1.1 Background . . . . .	1
1.2 Summary of results . . . . .	1
1.3 Structure of the thesis . . . . .	1
1.4 Notation . . . . .	2
<b>2 Quantum Chemistry</b>	<b>3</b>
2.1 Quantum Mechanics . . . . .	3
2.1.1 The postulates of quantum mechanics . . . . .	3
2.1.2 The Schrödinger equation . . . . .	5
2.2 Two-particle system . . . . .	6
2.3 Many-body systems . . . . .	6
2.3.1 The Born–Oppenheimer approximation . . . . .	7
2.3.2 Variational principle . . . . .	8
2.3.3 Self-consistent field . . . . .	9
2.3.4 Density Functional Theory . . . . .	12
<b>3 Multiwavelet Basis</b>	<b>15</b>
3.1 Different types of basis sets . . . . .	15
3.1.1 Atom centered basis sets . . . . .	15
3.1.2 Periodic basis sets . . . . .	16
3.2 Multiresolution analysis . . . . .	17
3.2.1 Definition . . . . .	17
3.2.2 The Haar wavelet . . . . .	17
3.2.3 Projecting a Gaussian function example . . . . .	19
3.3 Multiwavelet Multiresolution Analysis (MRA) . . . . .	19
3.3.1 Constructing the basis functions in one dimension . . . . .	19
3.3.2 Choices of scaling functions . . . . .	21
3.4 Operators . . . . .	22
3.4.1 Non-standard form representation of operators . . . . .	22
3.4.2 Examples of operators . . . . .	24
3.5 Self-Consistent Field (SCF) method in multiwavelet basis . . . . .	26
<b>4 Solvent Effect</b>	<b>27</b>
4.1 Outlining the problem . . . . .	28
4.1.1 Reaction field . . . . .	28
4.2 Explicit solvation models . . . . .	29

4.3	Implicit solvation models . . . . .	29
4.3.1	Cavity . . . . .	30
4.3.2	Boundary conditions . . . . .	32
4.3.3	Approaches to a solution . . . . .	32
4.3.4	Solving the generalized Poisson equation in multiwavelet basis . . .	34
4.4	Variational formulation of the Generalized Poisson equation . . . . .	36
<b>5</b>	<b>Implementation of the generalized Poisson equation</b>	<b>39</b>
5.1	Generalized Poisson equation on multiwavelet basis . . . . .	39
5.1.1	Cavity Function . . . . .	39
5.1.2	Dielectric Function . . . . .	39
5.1.3	Effective volume charge distribution . . . . .	41
5.1.4	Surface charge distribution . . . . .	41
5.1.5	The iterative Self-Consistent Reaction Field (SCRf) method . . . .	42
5.2	Variational implementation . . . . .	43
5.3	Software used . . . . .	43
<b>6</b>	<b>Results</b>	<b>45</b>
6.1	Overview of tests . . . . .	45
6.2	Data . . . . .	46
6.2.1	Theoretical correctness tests . . . . .	46
6.2.2	Parametrization Tests . . . . .	48
6.2.3	Comparison Tests . . . . .	54
6.2.4	Variational implementation tests . . . . .	58
6.3	Discussion . . . . .	60
6.3.1	Theoretical correctness . . . . .	60
6.3.2	Parametrization . . . . .	60
6.3.3	Comparison . . . . .	61
6.3.4	Variational implementation . . . . .	62
6.4	Concluding remarks . . . . .	62
6.5	Areas of improvement/future development . . . . .	63
<b>A</b>	<b>Data tables</b>	<b>69</b>
<b>B</b>	<b>Test Figures</b>	<b>77</b>

# Acknowledgements

First and foremost I would like to thank my supervisor Luca Frediani for all the assistance, knowledge and patience he has provided.

I would like to thank my co-supervisors Stig Rune Jensen and Magnar Bjørgve who were quick to help me whenever I needed assistance.

I would like to thank all the people of the MRChem group for their welcoming attitude and help throughout these past semesters.

Lastly, I would like to thank my family for their support throughout these years, and Jeanette, who has supported me all the way.



# List of Figures

3.1	Projecting a Gaussian function with Haar basis . . . . .	20
4.1	SAS and SES surfaces . . . . .	31
5.1	Interlocking spheres cavity for water . . . . .	40
5.2	Reaction potential of water across the XZ plane . . . . .	44
6.1	Reaction field energy of H <sub>2</sub> O . . . . .	50
6.2	Reaction field energy of Li <sup>+</sup> . . . . .	50
6.3	Relative difference of H <sub>2</sub> O against Gaussian double augmented results . . .	51
6.4	Relative difference of Li <sup>+</sup> against Gaussian double augmented results . . .	51
6.5	Relative difference of shifted radius H <sub>2</sub> O against Gaussian double augmented results . . . . .	52
6.6	Relative difference of shifted radius Li <sup>+</sup> against Gaussian double augmented results . . . . .	52
6.7	Relative difference of Li <sup>+</sup> with varied precision against Gaussian results . .	53
6.8	Energy plots for NO <sup>+</sup> . . . . .	56
6.9	Energy plots for CN <sup>-</sup> . . . . .	56
6.10	Relative difference between NO <sup>+</sup> and double augmented Gaussian results .	57
6.11	Relative difference between CN <sup>-</sup> and double augmented Gaussian results .	57
6.12	Reaction field energy for H <sub>2</sub> O in water using the variational and iterative implementation . . . . .	58
6.13	Reaction field energy for Li <sup>+</sup> in water using the variational and iterative implementation . . . . .	58
6.14	Relative difference between the reaction field energy of H <sub>2</sub> O calculated with the variational implementation against the iterative implementation . . . .	59
6.15	Relative difference between the reaction field energy of Li <sup>+</sup> calculated with the variational implementation against the iterative implementation . . . .	59
B.1	Reaction field energy of H <sub>2</sub> O . . . . .	78
B.2	Reaction field energy of Li <sup>+</sup> . . . . .	79
B.3	Relative difference between methods for H <sub>2</sub> O . . . . .	80
B.4	Relative difference between methods for Li <sup>+</sup> . . . . .	81
B.5	Relative difference between methods for H <sub>2</sub> O with radius +0.2 Bohr . . . .	82
B.6	Relative difference between methods for Li <sup>+</sup> with radius +0.2 Bohr . . . .	83
B.7	Energy plots for NO <sup>+</sup> . . . . .	84
B.8	Energy plots for CN <sup>-</sup> . . . . .	85
B.9	Relative difference between methods for NO <sup>+</sup> . . . . .	86
B.10	Relative difference between methods for CN <sup>-</sup> . . . . .	87





# List of Tables

1.1	Notation used in this thesis . . . . .	2
6.1	Reaction charge for $\epsilon_{out} = 2$ . . . . .	47
6.2	Reaction charge for $\epsilon_{out} = 80$ . . . . .	47
6.3	Reaction field energy for a point charge of $\epsilon_{out} = 2$ . . . . .	47
6.4	Reaction field energy for a point charge of $\epsilon_{out} = 80$ . . . . .	47
6.5	$E_{tot}$ for H <sub>2</sub> O in Water sample . . . . .	48
6.6	[ $E_r$ for H <sub>2</sub> O in Water sample]Reaction Field Energy Calculations example for H <sub>2</sub> O in water, Energy in Hartree and radii of the cavity in Bohr . . . .	49
6.7	Relative difference between Gaussian and MRCHEM results for H <sub>2</sub> O . . . .	54
6.8	Relative difference between Gaussian and MRCHEM results for NO <sup>+</sup> . . . .	55
6.9	Relative difference between Gaussian and MRCHEM results for CN <sup>-</sup> . . . .	55
6.10	Relative difference between Gaussian and MRCHEM results for CH <sub>3</sub> CONH <sub>2</sub>	55
A.1	Total Energy of H <sub>2</sub> O. Radius in top row in Bohr and energies in Hartree .	70
A.2	Total Energy of NO <sup>+</sup> . Radius in top row in Bohr and energies in Hartree .	70
A.3	Total Energy of CN <sup>-</sup> . Radius in top row in Bohr and energies in Hartree .	70
A.4	Total energy of Li <sup>+</sup> . Radius on top row in Bohr and energies in Hartree . .	71
A.5	Reaction field energy of Li <sup>+</sup> . Radius on top row in Bohr and energies in Hartree . . . . .	71
A.6	Reaction field energy of H <sub>2</sub> O. Radius on top row in Bohr and energies in Hartree . . . . .	72
A.7	Reaction field energy of NO <sup>+</sup> . Radius on top row in Bohr and energies in Hartree . . . . .	72
A.8	Reaction field energy of CN <sup>-</sup> . Radius on top row in Bohr and energies in Hartree . . . . .	72
A.9	Total energies for CH <sub>3</sub> CONH <sub>2</sub> with molecular shaped cavity, radii in Bohr and energies in Hartree . . . . .	73
A.10	Total energies for H <sub>2</sub> O with molecular shaped cavity . . . . .	73
A.11	Total energies for NO <sup>+</sup> with molecular shaped cavity . . . . .	74
A.12	Total energies for CN <sup>-</sup> with molecular shaped cavity . . . . .	74
A.13	Reaction field energies for H <sub>2</sub> O with molecular shaped cavity . . . . .	75
A.14	Reaction field energies for NO <sup>+</sup> with molecular shaped cavity . . . . .	75
A.15	Reaction field energies for CN <sup>-</sup> with molecular shaped cavity . . . . .	76
A.16	Reaction field energies for CH <sub>3</sub> CONH <sub>2</sub> with molecular shaped cavity . . . .	76



# Chapter 1

## Introduction

### 1.1 Background

Gas phase calculations for Quantum chemical systems have well defined and reliable results which can be used to predict properties from several systems in vacuum. Although, it is rare for an experimental chemist to work with gas phase properties. Most of the processes of interest chemical processes and mechanisms happen while in a solvent [1]. Therefore it is important to be able to produce reliable results when working with these systems. Many models exist to solve this system, outlined in chapter 4, but, in this thesis, we will mainly focusing on Polarizable Continuum Model (PCM).

A big hurdle for PCM is working with the sharp transition between solvent and solute. Numerous methods have been implemented in order to minimize the discontinuity at this boundary [2]. Our approach is to define both the solvent and substrate environments as an analytical function represented with Multiwavelet (MW) basis.

MW are a part of a family of basis classified under MRA. MW basis sets have useful characteristics for development of solutions of partial differential equations. These are orthogonality of wavelet spaces, vanishing moments and locally adaptive representations of functions, which allow for further refining critical areas of a system.

### 1.2 Summary of results

The main goal with this project was to have a working implementation of solvent effect in MW basis by following in Fosso-tande's footsteps [1]. Another objective was to implement a variational formulation of the Generalized Poisson Equation (GPE) as defined in [3].

We found that the implementation managed to produce values that did not differ significantly from exact calculations of the properties tested, these being the Born energy of the solvent [4] and Gauss' theorem as defined in [5]. The energy calculations yielded results that converged towards Gaussian results as the radii increased. We also tested the Variational formulation of the GPE shown in [3], which gave promising results for small systems, such as  $\text{Li}^+$ , but showed room for improvement for bigger systems.

### 1.3 Structure of the thesis

In chapter 2 of this thesis the quantum and computational Chemical formalism will be presented along with methods used to solve systems. Among these are the Born-

Oppenheimer approximation, variational principle, Hartree–Fock (HF) method and Density Functional Theory (DFT).

Some examples of Wavelet basis are shown and Chapter 3 will mention some basis sets and define MW the implementation of different operators is described.

Chapter 4 describes the particular system we work with in this thesis, namely, solvent effect and the reaction potential. This chapter will also introduce a new variational formulation of the GPE used in solving the electrostatic reaction field problem.

Chapter 5 describes how the reaction field Potential was implemented using MRCHEM. It will also describe the way the variational formulation was implemented.

Chapter 6 Goes through the systems that were used to test the implementation, along with the type of tests that were performed. The results will be tabulated and some figures will be shown. Finally an analysis and discussion of the results will be presented along with points of improvement and future development.

## 1.4 Notation

Notation differs slightly between works in computational and Quantum Chemistry. Most of the equations and formulas use the same standard notation, while others might differ slightly in accents and other details in their notations. Therefore in this section a summarization of notation used in this thesis will be given.

The following Table 1.1 shows most of the notation used for common objects in mathematics and quantum mechanics.

Object	Description of notation	Examples
vectors	lower case letter, or symbol, with an arrow above them	$\vec{r}, \vec{x}, \vec{\Psi}$
vector elements	lower case letter, or symbol, with an arrow above them and index subscripts	$\vec{r}_i, \vec{x}_1, \vec{\Psi}_x$
matrices	Upper case letter or symbols with a line above them	$\bar{A}, \bar{F}, \bar{S}$
matrix elements	Upper case letter with a line above them and index subscripts (rows, columns)	$\bar{A}_{ij}, \bar{F}_{11}, \bar{S}_{\mu\nu}$
Operators	Presented as a symbol with a $\hat{\ } above it$	$\hat{O}, \hat{H}, \hat{F}$
functions	presented by a letter with their input variables enclosed in parentheses ()	$f(x), \Psi(\vec{r})$
functionals	presented by a letter with their input functions enclosed in square brackets []	$E[f], F[\Psi]$

Table 1.1: Notation used in this thesis

Because we are working with atomic units, many of the common constants are reduced to unit value. The constants used in this thesis are the elementary charge  $e$  the reduced Planck constant  $\hbar$ , the electron mass  $m_e$  and vacuum permittivity  $\epsilon_{in}$  are all unit value.

Finally, we will be working in Dirac notation, which means we write a state vector of a wave function  $\Psi$  as  $|\Psi\rangle$  and its complex conjugate as  $\langle\Psi|$ . The scalar product in Dirac notation is defined as

$$\langle\Psi|\Phi\rangle = \int_{\mathbb{R}^3} \Psi^* \Phi d\vec{r} \quad (1.1)$$

# Chapter 2

## Quantum Chemistry

### 2.1 Quantum Mechanics

#### 2.1.1 The postulates of quantum mechanics

Quantum Mechanics (QM) are based on a set rules that define operations and states. We will present these rules as six different postulates of QM (sometimes divided as 5) [6, 7].

##### First postulate

The first postulate states that everything known about a physical system can be extracted from the wave function  $\Psi(x, t)$  of that system [6]. The wave function is defined as a function vector, or state vector,  $|\Psi(t_0)\rangle \in L^2$  that has a defined finite scalar product as shown in Equation 1.1 [7]

##### Second postulate

A generic observable  $O$  is represented by a generic operator  $\hat{O}$ . Two such observables are the position and momentum of a particle. These are represented by  $\hat{q}_i$  and  $\hat{p}_i$  respectively, where  $i = \{x, y, z\}$ . These operators fulfill the following commutation relations [6, 7]:

$$\begin{aligned} [q_i, p_j] &= i\hbar\delta_{ij} \\ [q_i, q_j] &= 0 \\ [p_i, p_j] &= 0 \end{aligned} \tag{2.1}$$

The Operators that represent observables are linear and Hermitian.

##### Third postulate

When measuring an observable  $O$  on a system  $|\Psi\rangle$ , the only possible values of the measurement are eigenvalues of the corresponding operator  $\hat{O}$  onto the measured system  $\Psi$  at its current state  $|\Psi_i\rangle$ . The eigenvalues are solutions to the following equation [7]

$$\hat{O} |\Psi_i\rangle = o_i |\Psi_i\rangle \tag{2.2}$$

This holds true even if the state measured is not an eigenstate of  $\hat{O}$ .

A system state vector  $|\Psi\rangle$  that is not an eigenstate of  $\hat{O}$  as a linear combination of eigenstates  $|i\rangle$  of the operator can be represented as

$$|\Psi\rangle = \sum_i c_i |i\rangle \quad (2.3)$$

where the coefficients  $c_i$  are computed as the projection of  $|\Psi\rangle$  onto the eigenstates of the operator

$$c_i = \langle i|\Psi\rangle. \quad (2.4)$$

Let us say that we apply the generic operator on one of its eigenstates that is multiplied with the projection coefficient  $c_i$  from Equation 2.4. This gives us

$$\hat{O}c_i |i\rangle = c_i \hat{O} |i\rangle = c_i o_i |i\rangle = o_i c_i |i\rangle \quad (2.5)$$

Since  $c_i |i\rangle$  is one of the components in the eigenstate  $|\Psi\rangle$  applying the operator on it will always give us exactly one of its eigenvalues, with different probabilities depending on its projection on the set of eigenstates of the operator [7].

#### Fourth postulate

The fourth postulate states the possible probabilities of getting a specific eigenvalue for a given measurement. Let  $|i\rangle$  be an eigenfunction of  $\hat{O}$  such that:

$$\hat{O} |i\rangle = o_i |i\rangle \quad (2.6)$$

and

$$|\Psi\rangle = \sum_i c_i |i\rangle \quad (2.7)$$

has no degenerate eigenvalue. The probability of measuring eigenvalue  $o_i$  from  $|\Psi\rangle$  is given by [7]:

$$\begin{aligned} \mathcal{P}(o_i) &= |\langle i|\Psi\rangle|^2 \\ &= \sum_j c_i^* c_j \langle i|j\rangle \\ &= \sum_j c_i^* c_j \delta_{ij} \\ &= |c_i|^2 \end{aligned} \quad (2.8)$$

Following the Equation 2.8 the probability of measuring the eigenvalue  $o_i$  from  $|\Psi_i\rangle$  is just one. The sum of all the probabilities for each eigenvalue is:

$$\sum_i \mathcal{P}(o_i) = \sum_i |c_i|^2 = 1 \quad (2.9)$$

Here we have ignored the case for degenerate eigenvalues and continuous spectra of eigenvalues, where the method is analogous to the one used above. The reader is invited to look them up themselves in [6, 7].



### Fifth postulate

The fifth postulate states that immediately after a measurement where the eigenvalue was  $o_i$  the state of the system  $|\Psi\rangle$  collapses into a state where the only value one can measure is  $o_i$ , which is  $|i\rangle$  using the conventions stated in postulate 3 and 4. This is because before measuring, the probabilities for any eigenvalue is as stated in the fourth postulate. When the value has been measured the uncertainty does not exist, as the state of the system must be one that gives exactly that value. The following Equation 2.10 represents the postulate.

$$|\Psi\rangle \xrightarrow{o_i} |\Psi_i\rangle \quad (2.10)$$

### Sixth postulate

When undisturbed, the system changes in a deterministic way [7]. This change is governed by the time dependent Schrödinger Equation (SE) [7, 6]:

$$i\hbar \frac{\partial}{\partial t} |\Psi\rangle = \hat{H} |\Psi\rangle \quad (2.11)$$

Where  $\hat{H}$  is the Hamiltonian operator which has the total energy of the system as its eigenvalues.

## 2.1.2 The Schrödinger equation

Lets consider the following SE for a particle allowed to move in only one dimension and where its potential energy varies with position (e.g., the Harmonic oscillator model [7, 8]).

$$\hat{H}\Psi = \left( -\frac{\hbar^2}{2m} \frac{\partial^2}{\partial x^2} + \hat{V}(x) \right) \Psi = i\hbar \frac{\partial}{\partial t} \Psi \quad (2.12)$$

We can substitute

$$\Psi(x, t) = \psi(x)\tau(t)$$

into 2.12 by assuming that the wave function can be separated into spatial and time dependent functions [6]:

$$\begin{aligned} \left( -\frac{\hbar^2}{2m} \frac{\partial^2}{\partial x^2} + \hat{V}(x) \right) \psi\tau &= i\hbar \frac{\partial}{\partial t} \psi\tau \\ -\frac{\hbar^2}{2m} \tau \frac{d^2\psi}{dx^2} + \hat{V}(x)\psi\tau &= i\hbar\psi \frac{d\tau}{dt} \\ -\frac{\hbar^2}{2m} \frac{1}{\psi} \frac{d^2\psi}{dx^2} + \hat{V}(x) &= i\hbar \frac{1}{\tau} \frac{d\tau}{dt} \end{aligned} \quad (2.13)$$

In the last step of the Equation 2.13 we divided both sides with  $\frac{1}{\tau\psi}$ . This shows that, since the left-hand side of the equation is only dependent on  $x$  and the right-hand side is only dependent on  $t$ , no matter how much we change each of the coordinates, they must always equal to a constant. This constant will be denoted by  $E$  as it is the energy of the system. This gives us the following set of equations [6]:

$$-\frac{\hbar^2}{2m} \frac{d^2\psi}{dx^2} + \hat{V}(x)\psi = E\psi \quad (2.14a)$$

$$i\hbar \frac{d\tau}{dt} = E\tau \quad (2.14b)$$

Equation 2.14b can be solved by observation as [6, 7] :

$$\tau(t) = e^{-iE\frac{t}{\hbar}} \quad (2.15)$$

while the remaining Equation 2.14a can be rewritten as

$$\hat{H}\psi = E\psi \quad (2.16)$$

which is the time-independent SE.

The energy of the system can be calculated as follows [9]:

$$\frac{\langle \psi | \hat{H} | \psi \rangle}{\langle \psi | \psi \rangle} = E \quad (2.17)$$

If the wave function is normalized the denominator becomes 1.

## 2.2 Two-particle system

A two-particle system (such as the H or the He<sup>+</sup> atoms) has a simple Hamiltonian of the form

$$\hat{H} = \hat{T}_N + \hat{T}_e + \hat{V} \quad (2.18)$$

where  $\hat{T}_N$  and  $\hat{T}_e$  are the kinetic energy operators of the nucleus  $N$  and of the electron  $e$  and  $\hat{V}$  is the Coulomb potential for two-particles [8, 10]. This system has an analytical solution in which one follows these steps:

1. Set a center of mass coordinate system.
2. Change to spherical coordinates so that the potential operator becomes a simple function of the radius.
3. Separate into radial function  $R(r)$  and angular function  $Y(\theta, \phi)$ . The angular function can be separated into two more functions  $\Theta(\theta)$  and  $\Phi(\phi)$ .
4. Solve as three sets of differential equations [11].

Following the steps above, the two-particle system is analytically solvable for the center of mass and angular motion when the potential energy is defined as function of only the distance between the nucleus and the electron. Examples are the harmonic oscillator and the Coulomb potential.

## 2.3 Many-body systems

For bigger systems, there is no practical way to analytically solve the SE [10]. For one, for each particle, the amount of dimensions that need to be evaluated increases by three, that is, one can expect the wave function dimension to increase by a factor of  $3N$  for each particle  $N$  [9].

Additionally, the potential energy operator becomes more complicated, as it would not just have the attractive forces between electron-nuclei, but also the repulsive forces between all the electrons and between all the nuclei. Both of these problems add more terms per particle and thus would be impossible to be solved in a realistic time frame [10].

### 2.3.1 The Born–Oppenheimer approximation

A many-body system consists of  $N$  nuclei with mass  $m_I$  for each nucleus  $I$  and  $n$  electrons with mass  $m_i$  for each electron  $i$ . Each nucleus has a charge  $Z_I e$  and each electron has a charge  $-e$ , where  $Z_I$  is the atomic number of the nucleus  $I$  and  $e$  is the elementary charge [8]. The  $N$  nuclei and  $n$  electrons are located in a three-dimensional coordinate system where each nucleus  $I$  has coordinates  $\vec{R}_I = (x_I, y_I, z_I)$  and each electron has coordinates  $\vec{r}_i = (x_i, y_i, z_i)$ .

To calculate the total energy and wave functions of the system we define a time independent SE where the wave function is dependent on the coordinates of both the electrons and the nuclei, which we will use a single  $\vec{R}$  to the coordinates of all the nuclei and a single  $\vec{r}$  to denote the coordinates of all the electrons.

$$\hat{H}\Psi(\vec{r}, \vec{R}) = E\Psi(\vec{r}, \vec{R}) \quad (2.19)$$

Here the Hamiltonian, as with the two-particle system, has a potential energy  $\hat{V}$  and a kinetic energy  $\hat{T}$  operator. As with the two-particle system, we can divide  $\hat{T}$  as a sum of two contributions, an electron contribution  $\hat{T}_e$  and a nuclear contribution  $\hat{T}_N$ . The only difference is that these contributions are sums over all the particles instead of just one each[9]

$$\hat{T}_e = \sum_i^n \frac{\hbar}{2m_i} \nabla_i^2 \quad (2.20)$$

$$\hat{T}_N = \sum_I^N \frac{\hbar}{2m_I} \nabla_I^2 \quad (2.21)$$

where  $\nabla_k^2$  is the Laplacian operator operating on particle  $k$

$$\nabla_k^2 = \left( \frac{\partial^2}{\partial x_k^2} + \frac{\partial^2}{\partial y_k^2} + \frac{\partial^2}{\partial z_k^2} \right). \quad (2.22)$$

The potential operator, which we define as a sum of Coulomb potentials, is now much more complicated. It consists of three contributions: the nucleus-electron attraction  $\hat{V}_{Ne}$ , the nucleus-nucleus  $\hat{V}_{NN}$  repulsion and the electron-electron repulsion  $\hat{V}_{ee}$  [9].

$$\hat{V}_{Ne} = \sum_I^N \sum_i^n -\frac{Z_I e^2}{|\vec{R}_I - \vec{r}_i|} \quad (2.23)$$

$$\hat{V}_{NN} = \frac{1}{2} \sum_{I \neq J}^N \frac{Z_I Z_J e^2}{|\vec{R}_I - \vec{R}_J|} \quad (2.24)$$

$$\hat{V}_{ee} = \frac{1}{2} \sum_{i \neq j}^n \frac{e^2}{|\vec{r}_i - \vec{r}_j|} \quad (2.25)$$

where  $I, J$  iterate through the nuclei and  $i, j$  iterate through the electrons. The Hamiltonian is therefore dependent on the positions of all the electrons and all the nuclei [10]

$$\hat{H}(\vec{r}, \vec{R}) = \hat{T}_e + \hat{T}_N + \hat{V}_{Ne} + \hat{V}_{NN} + \hat{V}_{ee} \quad (2.26)$$

Both repulsion potentials  $\hat{V}_{NN}, \hat{V}_{ee}$  have  $\frac{N(N-1)}{2}$  and  $\frac{n(n-1)}{2}$  terms respectively, while the other terms have much simpler sums over one index in the case of the kinetic energies and  $N \cdot n$  terms in the attraction potential  $\hat{V}_{Ne}$ .

In the Born–Oppenheimer (BO) we assume that the nuclei of the molecule are much heavier than the electrons (a single proton is approximately 1836 times heavier than an electron [12]) the electrons can instantaneously respond to any change in the configuration of the nuclei [6]. That means that we can solve an electronic problem for any given nuclear geometry as if the nuclei were static [8, 9, 10].

Following this assumption we separate the wave function into an electronic  $\Psi_e$  and a nuclear wave function  $\Psi_N$

$$\Psi(\vec{r}, \vec{R}) = \Psi_N(R)\Psi_e(\vec{r}; \vec{R}). \quad (2.27)$$

Notice that the nuclear wave function is only dependent on the nuclear coordinates, while the electronic has both the electron and nuclear coordinates as input. From our assumption above we say that we solve an electronic SE for each geometry of the molecule, thus the nuclear coordinates are parametric variables of the electronic wave function (symbolized by the semicolon divider ;) which remain constant for each solution of the SE.

The electronic SE is as follows

$$\hat{H}_e(\vec{r}; \vec{R})\Psi_e(\vec{r}; \vec{R}) = E_e(\vec{R})\Psi_e(\vec{r}; \vec{R}) \quad (2.28)$$

Where the electronic energy  $E_e$  becomes a function of  $\vec{R}$  which is solved as a constant for each nuclear geometry. In the electronic Hamiltonian we assume that the kinetic energy of the nuclei is zero, but we still need to compute the nuclear repulsion  $V_{NN}$ . As we are solving for any given geometry  $V_{NN}$  becomes a constant [9]. The electron Hamiltonian  $\hat{H}_e$  is as follows

$$\hat{H}_e(\vec{r}; \vec{R}) = \hat{T}_e + \hat{V}_{Ne} + \hat{V}_{ee} + \hat{V}_{NN} \quad (2.29)$$

Solving the electronic SE for all possible nuclear geometries will give a Potential Energy Surface (PES) defined by the electronic energy for all the different geometries. With this we can go on to solve the total SE [10]

$$\left[ T_N + E_e(\vec{R}) \right] \Psi_N(\vec{R}) = E_{tot} \Psi_N(\vec{R}) \quad (2.30)$$

In the following sections we will be talking mostly about solving the electronic SE, where we will drop the subscript and simply denote the electronic wave function as  $\Psi$  and its Hamiltonian as  $\hat{H}$ .

### 2.3.2 Variational principle

Consider a complete set of orthonormal eigenfunctions  $\Psi_i$  of the Hamiltonian  $\hat{H}$ . From Equation 2.7 we build a representation of an arbitrary wave function  $\Phi$  with a linear combination of the eigenfunctions with projection coefficients  $c_i$ .

$$\Phi = \sum_i c_i \Psi_i \quad (2.31)$$

For ease of notation we assume that  $\Phi$  is normalized. This the following

$$\langle \Phi | \Phi \rangle = \sum_i^n c_i^2 = 1 \quad (2.32)$$

Additionally, the energy associated with the Hamiltonian can be calculated as in Equation 2.17 to give us

$$\langle \Phi | \hat{H} | \Phi \rangle = \sum_i^n c_i^2 E_i \quad (2.33)$$

This tells us the energy of the wave function  $\Phi$  can be determined by knowing the energies  $E_i$  of each eigenfunction  $\psi_i$  and the coefficients  $c_i$  associated with the linear combination that describes  $\Phi$  [9].

We know that for this to be a quantum mechanical system there must be a lowest energy among all energies  $E_i$ . We choose to call this lowest energy  $E_0$ . Subtracting  $E_0$  from Equation 2.33 to find the difference between the calculated energy of the arbitrary wave function  $\Phi$  with respect to the ground state eigenvalues:

$$\sum_i^n c_i^2 (E_i - E_0) = \langle \Phi | \hat{H} | \Phi \rangle - E_0 \quad (2.34)$$

We know that each term  $c_i$  must be greater or equal to zero (non-trivial) and that the term  $(E_i - E_0)$  must be greater or equal to zero as well [9], as each individual  $E_i$  may add more energy to the ground state. This leads to the following set of inequalities.

$$\begin{aligned} \langle \Phi | \hat{H} | \Phi \rangle - E_0 &\geq 0 \\ \langle \Phi | \hat{H} | \Phi \rangle &\geq E_0 \end{aligned} \quad (2.35)$$

It can be inferred from 2.17 that the inequality in the last term in 2.35 shows that the energy calculated as an eigenvalue of  $\Phi$  is always greater or equal to zero. This lets us construct our trial wave functions for the ground state of a system with any basis set. We can assess the quality of the guess by their associated energies, attempting to reach as low a value as possible [9].

### 2.3.3 Self-consistent field

In the previous sections we showed two main points about solving the SE for many-body systems. The first one, with the BO approximation, is that we, instead of solving for the energy of the whole system at the same time, can solve an electronic SE for each geometry of the molecule. Secondly we can construct the wave function with a basis set representation of our choice, for which its accuracy is evaluated by how low the calculated energy is.

Next, we intend to find a way to systematically create wave functions and minimize them as in the variational principle. This is done with an iterative procedure called the SCF.

#### Slater determinant

The electronic wave function seen in section 2.3.1 needs to include all the coordinates that identify an electron. These properties are the spatial coordinates  $x, y, z$ , and the spin coordinate  $s$ . Another characteristic is that it needs to be anti-symmetric, that is it must change sign whenever the coordinates of two electrons, spatial and spin, are interchanged.

The characteristics stated above can be summarized by writing the wave function as a Slater determinant as [9, 13]

$$\Psi_{SD} = \frac{1}{\sqrt{n!}} \begin{vmatrix} \phi_1(1) & \phi_2(1) & \dots & \phi_n(1) \\ \phi_1(2) & \phi_2(2) & \dots & \phi_n(2) \\ \vdots & \vdots & \ddots & \vdots \\ \phi_1(n) & \phi_2(n) & \dots & \phi_n(n) \end{vmatrix}, \quad (2.36)$$

where each  $\phi_i$  is a one-electron spinorbital, a wave function constructed as a product of a spatial function and a spin function[13],  $n$  is the total amount of electrons, the coefficient outside the determinant is a normalization constant and each of the spin orbitals are orthonormal to each other.

In a Slater determinant each column represent a spinorbital and each row one electron. The spatial orbitals can, and are mostly, built using a basis set as described in Equation 2.7. The spin functions are orthonormal eigenfunctions of the operator  $\hat{S}_z$  and have only two eigenvalues  $\pm \frac{\hbar}{2}$  [9].

In certain situations it might be needed to express a wavefunction as a sum of Slater determinants, but here we will work only as if our wave function can be constructed by a single determinant wave function.

### Energy of a Slater determinant

The energy of a single Slater determinant is expressed as

$$E = \sum_i^n \langle \phi_i | \hat{h} | \phi_i \rangle + \frac{1}{2} \sum_{ij}^n \left( \langle \phi_j | \hat{J}_i | \phi_j \rangle - \langle \phi_j | \hat{K}_i | \phi_j \rangle \right) + \hat{V}_N, \quad (2.37)$$

where

$$\hat{h} | \phi_i \rangle = \left( -\frac{1}{2} \nabla_i^2 - \sum_I^N \frac{Z_I}{|\vec{R}_I - \vec{r}_i|} \right) | \phi_i \rangle, \quad (2.38)$$

$$\hat{J}_i | \phi_j(2) \rangle = \left\langle \phi_i(1) \left| \frac{1}{|\vec{r}_1 - \vec{r}_2|} \right| \phi_i(1) \right\rangle | \phi_j(2) \rangle, \quad (2.39)$$

$$\hat{K}_i | \phi_j(2) \rangle = \left\langle \phi_i(1) \left| \frac{1}{|\vec{r}_1 - \vec{r}_2|} \right| \phi_j(1) \right\rangle | \phi_i(2) \rangle, \quad (2.40)$$

$\hat{V}_N$  is the nuclear repulsion, the operator  $\hat{h}_i$  is a one-electron Hamiltonian containing the electronic kinetic energy and the nucleus-electron Coulomb attraction and  $\hat{J}_i$  and  $\hat{K}_i$  are the Coulomb integral operator and the exchange integral operator respectively [13, 9] which apply the two-electron integrals of the same name on a orbital  $\phi_j$ .

### Variational principle on a Slater determinant

The energy of a Slater determinant, defined in 2.37, can be minimized with respect to the orbitals variations under the constraint that the occupied orbitals stay orthonormal [10].



We construct a Lagrange equation as in [13]:

$$L = E - \sum_{ij} \lambda_{ij} (\langle \phi_i | \phi_j \rangle - \delta_{ij}) \quad (2.41)$$

$$\delta L = \delta E - \sum_{ij} \lambda_{ij} (\langle \delta \phi_i | \phi_j \rangle + \langle \phi_i | \delta \phi_j \rangle) \quad (2.42)$$

where

$$\begin{aligned} \delta E &= \sum_i^n \left( \langle \delta \phi_i | \hat{h} | \phi_i \rangle + \langle \phi_i | \hat{h} | \delta \phi_i \rangle \right) \\ &+ \frac{1}{2} \sum_{ij}^n \left( \langle \delta \phi_i | \hat{J}_j - \hat{K}_j | \phi_i \rangle + \langle \phi_i | \hat{J}_j - \hat{K}_j | \delta \phi_i \rangle \right) \\ &+ \frac{1}{2} \sum_{ij}^n \left( \langle \delta \phi_j | \hat{J}_i - \hat{K}_i | \phi_j \rangle + \langle \phi_j | \hat{J}_i - \hat{K}_i | \delta \phi_j \rangle \right) \end{aligned} \quad (2.43)$$

and  $\lambda_{ij}$  is the Lagrange multiplier. The goal is to find a set of orbitals that give us a minimum of the Lagrange equation  $\delta L = 0$ .

### Hartree–Fock equations

We can remove the multiplication by a half outside the sums as the third and fourth terms count the same operations, and so do the fourth and sixth terms. We can also substitute the Fock operator  $\hat{F}$  into equation 2.43 as [10]

$$\delta E = \sum_j^n \left( \langle \delta \phi_j | \hat{F} | \phi_j \rangle + \langle \phi_j | \hat{F} | \delta \phi_j \rangle \right) \quad (2.44)$$

$$\hat{F} = \hat{h} + \sum_j^n \left( \hat{J}_j - \hat{K}_j \right) \quad (2.45)$$

We substitute 2.44 into 2.43 and use properties of complex conjugates to manipulate the equation as shown in [10] to give us the HF equations

$$\hat{F} \phi_i = \sum_j^n \lambda_{ij} \phi_j \quad (2.46)$$

where we can construct a  $n \times n$  matrix out of these sums called the Fock matrix. We then diagonalize the Fock matrix and get the following set of eigenvalue equations

$$\hat{F} \phi'_i = \epsilon_i \phi'_i \quad (2.47)$$

where the  $\epsilon_i$  is the energy of each orbital. When diagonalizing the matrix the orbitals get changed slightly, creating new orbitals. We denote these new orbitals with a ' superscript.

In order for an orbital to be known, one must know the rest of the orbitals. We solve this by iteratively forming the Fock matrix, diagonalizing it and using these new orbitals to construct a new Fock matrix and repeat the process until the change in the orbitals reach below a predetermined threshold [14, 9]. This iterative method is called SCF.

The sum of the orbital energies do not give us the total energy of the system. For each electron, we are accounting for the repulsion and exchange interactions with all the other electrons, we end up counting twice. Which means we have to subtract half of these interactions from the total orbital energy. This gives the total energy  $E$  as [10]

$$E = \sum_i^n \epsilon_i - \frac{1}{2} \sum_{ij}^n (\hat{J}_{ij} - \hat{K}_{ij}) \quad (2.48)$$

An important point to note is that at the start of this section we assumed our wavefunction to consist of a single determinant. This is part of the HF approximation, where we only take into account the lowest energy level of the system, and we assume that a single Slater determinant is enough to describe it.

### 2.3.4 Density Functional Theory

Another SCF method is DFT. In this method we iterate over a density that is dependent the spatial dimensions only.

#### The density

In DFT we calculate the energy directly as a functional of the electron density distribution [5, 9] described by

$$\rho(\vec{r}) = n \int |\Psi_e(\vec{r}, \vec{r}_2, \dots, \vec{r}_n)| d\vec{r}_2 \dots d\vec{r}_n \quad (2.49)$$

which is an integral over all the possible configurations of the electrons. The coefficient  $n$  is the total amount of electrons on the system. This method, DFT, allows to discard computing the wave function in the iterative process and simply use the density instead.

The electron density has properties that are characteristic to each system, the molecule, it is constructed from. The first is that its integral over all space is equal to the amount of electrons  $n$  on the system [9]

$$\int_{\mathbb{R}^3} \rho d\vec{r} = n \quad (2.50)$$

The second is that the density has maxima on the positions of the nuclei, and these maxima have the following value dependent on the nuclear charge of said nuclei [9].

$$\left. \frac{\partial}{\partial \vec{r}} \rho(\vec{r}) \right|_{\vec{r}=\vec{R}_I} = -2Z_I \rho(\vec{r}) \quad (2.51)$$

#### Hohenberg–Kohn theorems

In DFT the electrons interact both with each other and with an external potential  $V_{ext}$ , such as the nucleus-electron attraction potential. In order to compute the total energy, we need to know how to determine both of those interactions. We know from the definitions above that the electrons can be described by the density. The Hohenberg-Kohn existence theorem states that the ground-state density of the system determines the  $V_{ext}$  [9]. The Hamiltonian of the system can thus be defined and from it one can define the wave function of the system.

Now that both the Hamiltonian and the wave function are determined by the ground state density we can go forth to solve for the energy of the system. Applying the variational

principle tells us that, for any such construction of wave functions and Hamiltonians, the energy computed will always be bigger or equal to the true ground state energy. This brings us to the Hohenberg–Kohn variational theorem, which states that we can keep choosing different densities to construct Hamiltonians and wave functions, and the ones that give us lower energy will be closer to the correct density [9].

The important points from the Hohenberg–Kohn theorems are that the energy of the system is entirely determinable from the ground-state density, and that we can get densities closer to the true density by minimizing the energy.

### Kohn–Sham theory

The energy is determined by a functional  $E[\rho]$  made of functionals representing the kinetic energy of the electrons  $T[\rho]$ , the attraction potential energy  $V_{Ne}[\rho]$ , and the two-electron repulsion energy  $V_e[\rho]$  [5, 15]

$$E[\rho] = V_{Ne}[\rho] + T[\rho] + V_e[\rho] \quad (2.52)$$

In Kohn–Sham theory, in order to compute the Kinetic energy functional, we assume that we can describe the energy of the system as the exact kinetic energy  $T_S$  of a single Slater determinant describing a charge distribution  $\rho$  of a fictitious system of non-interacting electrons, composed of orbitals  $\phi_i$  [10].

$$\rho = \sum_i^n |\phi_i|^2 \quad (2.53)$$

$$T_S = \sum_i^n \left\langle \phi_i \left| -\frac{1}{2} \nabla^2 \right| \phi_i \right\rangle \quad (2.54)$$

The attraction potential functional  $V_{Ne}[\rho]$  is easily determined as its classical definition [10]

$$V_{Ne}[\rho] = - \sum_I^N \int \frac{Z_I \rho(\vec{r})}{|\vec{R}_I - \vec{r}|} d\vec{r}. \quad (2.55)$$

We can also divide the two-electron repulsion into Coulomb  $J[\rho]$  and exchange  $K[\rho]$  contributions. Since we are describing  $\rho$  as in Equation 2.53 we can evaluate the Coulomb energy in the classical way as [10].

$$J[\rho] = \frac{1}{2} \int \int \frac{\rho(\vec{r}) \rho(\vec{r}')}{|\vec{r} - \vec{r}'|} d\vec{r} d\vec{r}', \quad (2.56)$$

Some of the kinetic energy is lost when we use the form in 2.54 since we are calculating from fictitious system of non-interacting electrons, and the exchange functional  $K[\rho]$  is not known. We gather these terms in a exchange correlation functional  $E_{xc}[\rho]$  as [10]

$$E_{xc}[\rho] = (T[\rho] - T_S) + (V_e - J[\rho]) \quad (2.57)$$

We can now redefine a new energy functional  $E_{DFT}[\rho]$  from 2.52 By substituting the definitions mentioned above [10]:

$$E_{DFT}[\rho] = T_S[\rho] + V_{Ne}[\rho] + J[\rho] + E_{xc}[\rho] \quad (2.58)$$

different ways of defining  $E_{xc}$  can be outlined in [9, 10].

By the variational principle discussed previously, we are trying to minimize the energy to get the best representation of the system with the given basis. Here we try to find minima by differentiating 2.58 with respect to  $\rho$  giving us

$$\frac{\partial}{\partial \rho} E[\rho] = \frac{\partial}{\partial \rho} (V_{Ne}[\rho] + T_S[\rho] + J[\rho]) + V_{xc} \quad (2.59)$$

Where  $V_{xc}$  is the functional derivative  $\frac{\partial}{\partial \rho} E_{xc}[\rho]$  [9]. We can see that  $V_{xc}$  seems to be a correction to the gradient to our first definition of the energy 2.52. The system described by Equation 2.52 is the fictitious system of non-interacting electrons. In this system we can define one-electron operators  $\hat{h}_i^{KS}$  as

$$\hat{h}_i^{KS} \phi_i = \epsilon_i \phi_i \quad (2.60)$$

$$\hat{h}_i^{KS} = -\frac{1}{2} \nabla_i^2 + v_{Ne} + v_e(\rho) + V_{xc} \quad (2.61)$$

where  $v_{Ne}$  and  $v_e(\rho)$  are one-electron operators for the nuclear-electron attraction and the two-electron potentials. We can start the SCF by creating a first guess  $\rho$  with a non-interacting Slater determinant. We can then solve set of one orbital SE created from 2.60 and get new orbitals, which can be used to start over and iterate in much the same manner as in HF theory.

# Chapter 3

## Multiwavelet Basis

As stated in the previous chapter 2, the main goal of computational chemistry is to approximate systems in order to calculate their energy through the SE. These systems are completely described by wave functions [7].

In order to construct a solution (wave function) to the SE of a given system one uses sets of functions with differing properties. These sets of functions construct a basis for the space on which the wave functions are projected into. These sets are thus called basis sets [9] and they are essential to solving many-body systems. In this text we will be focusing in the MW basis from MRA methods.

### 3.1 Different types of basis sets

We have mentioned constructing solutions of systems using basis sets represented as Linear Combination of Atomic Orbitals (LCAO), sums of basis functions multiplied with projection coefficients. In this section we discuss some basis sets used to solve quantum chemical systems.

#### 3.1.1 Atom centered basis sets

Some of the first basis sets to be developed were based on the assumption of centering the functions on the atom nucleus. These basis sets are called Slater-type orbitals (STO) and Gaussian-type orbitals (GTO). The basis functions (orbitals) follow from the separation of variables used in solving for one-electron atoms

$$\Psi(\vec{r}) = R(r)Y_{lm}(\theta, \phi), \quad (3.1)$$

where  $R$  is the radial part of the wave function and  $Y$  is the angular part of the wave function.

#### Slater-type orbitals

These basis functions are constructed from the observation that the wave function should decay exponentially to zero when the distance from the nucleus extends to infinity. They are typically of the form [10, 16]

$$\chi^{STO}(\vec{r}) = P(r)e^{-\zeta r}Y_{lm}(\theta, \phi), \quad (3.2)$$

where  $P$  is a polynomial representing the radial decay and  $\zeta$  represents the how diffuse the function is. These functions are characterized for them having a cusp at the nucleus, which follows from the treatment of the nucleus as a point charge. This cusp makes computing integrals and derivatives a complex problem.

### Gaussian-type orbitals

GTO are based on the same reasoning behind STO, but instead of letting the exponential decay be to the rate of  $r$  we let it be to the rate of  $r^2$ , that is, we work with Gaussian functions [16]. They have the following forms, both polar coordinates

$$\chi^{GTO}(\vec{r}) = P(r)e^{-\alpha r^2}Y_{lm}(\theta, \phi), \quad (3.3)$$

and Cartesian coordinates

$$\chi^{GTO}(\vec{r}) = (x - A_x)^k(y - A_y)^l(z - A_z)^m e^{-\alpha|\vec{r}-\vec{A}|^2}, \quad (3.4)$$

where the vector  $\vec{A}$  and its components represent the center of the atom. In this basis we remove the problem the STOs had of trying to evaluate the cusp of the function. The lack of a cusp also allows to treat the nucleus as more than a point charge. Another advantage is the fact that the functions are no longer constrained to a spherical coordinate system and can be evaluated on Cartesian coordinates. They are also separable in the Cartesian coordinate system as a product of one variable Gaussians.

On the other hand, the GTO decay too fast in comparison to the STO and do not describe the nucleus cusp correctly either, meaning that we have to make more considerations to the exponents and possibly have more functions per atom in order to find better solutions.

### Contracted Gaussian-type orbitals

In order to diminish the problem of the cusp in STO one tries to represent the STO as linear combinations of GTOs. This way the decay is properly modeled and the cusp is no longer a difficult problem to solve. This has the obvious weakness of needing to compute more basis functions for a single orbital, which increases the cost of running the calculations [9]. In order to remove this we define the GTOs as being represented by another linear combination of GTOs, but the coefficients for this one are known and static. This way we can have a better representation of STOs with GTOs [10].

### 3.1.2 Periodic basis sets

Periodic basis sets are a type of basis sets that are not centered on an atom. These basis sets are best at describing, as the name implies, systems with periodic boundary conditions. Two examples are metals and ion crystals.

#### Plane wave basis functions

In metals, one can think of the valence electrons as free electrons with periodic boundary conditions. The wave functions of these type of systems are described by either complex exponentials or cosine and sine functions [10].



On infinite systems the molecular orbitals, due to the space between different energy levels vanishing, can be described by a basis of plane waves. The definition in three dimensions is then a complex exponential.

To finish this section on basis sets we can comment on the applicability of these basis sets. Atom based basis sets are best at describing the electrons nearest the nucleus. STOs are more accurate in the decay, but the cusp at the nucleus is harder to differentiate, therefore, GTO basis sets are used to simplify the near nucleus differentiation. GTOs do not decay in the correct manner so one might want to use contracted GTOs.

Plane wave functions excel at describing slowly varying delocalized electron densities. An example is the valence and conduction bands in metal. They are not that good at describing internal electrons, where the oscillation frequency near the nuclei need to increase a lot in order to properly approximate the orbital [10].

## 3.2 Multiresolution analysis

### 3.2.1 Definition

Consider that we have a function  $\varphi \in L^2(\mathbb{R})$  where its translations and dilations are described as [17]

$$\varphi_k^j(x) = 2^{\frac{j}{2}}\varphi(2^j x - k), \quad j, k \in \mathbb{Z}, \quad (3.5)$$

and the function  $\varphi(x)$  satisfies the two-scale difference relations [18, 17, 5]

$$\begin{aligned} \varphi(x) &= \varphi(2x) + \varphi(2x - 1), \\ \varphi_k^j(x) &= \varphi_{2k}^{j+1}(2^{j+1}x - 2k) + \varphi_{2k+1}^{j+1}(2^{j+1}x - 2k - 1), \end{aligned} \quad (3.6)$$

where  $j$  is the scale of the function and  $k$  is the translation of the function [5]. A normalization constant is included in the definition of  $\varphi$ . A space  $V^n$  is spanned by translations of  $\varphi_{nk}$ . This space forms a hierarchical chain of linear subspaces [18]

$$V^0 \subset V^1 \subset \dots \subset V^j \subset \dots \subset L^2(\mathbb{R}), \quad (3.7)$$

where  $V^0$  is spanned only by  $\varphi_{0,0}(x) = \varphi(x)$  [5].

If relation 3.7 and the following refinement equation holds for  $\varphi_{j,k}(x)$  one can call the subspaces  $V^n$  or the functions  $\varphi_{j,k}(x)$  build a MRA of  $L_2(\mathbb{R})$ .

$$\varphi_k^j(x) = \sum_{k \in \mathbb{Z}} h_k^{j+1} \varphi_k^{j+1}(x), \quad (3.8)$$

where  $h$  is a coefficient characteristic to the transformation between scales.

### 3.2.2 The Haar wavelet

From now we will work with the Haar basis for simplicity [18]. Let us define the Haar function [17] as

$$\varphi_0^0 = \varphi(x) = \begin{cases} 1 & \text{for } x \in [0, 1) \\ 0 & \text{elsewhere} \end{cases}. \quad (3.9)$$

Let us now define a second set of subspaces  $W^n$ . These are the orthogonal complements of  $V^n$  [19], also called difference subspaces, defined as [18, 5, 19]

$$W^n \oplus V^n = V^{n+1}. \quad (3.10)$$

The subspaces  $W^n$  are then spanned by a set of functions defined by the translations and dilations of  $\psi(x)$

$$\psi_k^j(x) = 2^{\frac{j}{2}}\psi(2^j x - k), \quad j, k \in \mathbb{Z}, \quad (3.11)$$

where  $\psi(x)$  is called the Haar wavelet [17] and is defined as

$$\psi_0^0 = \psi(x) = \begin{cases} 1 & \text{for } x \in [0, \frac{1}{2}) \\ -1 & \text{for } x \in [\frac{1}{2}, 1), \\ 0 & \text{elsewhere} \end{cases} \quad (3.12)$$

and  $\varphi$  is related to  $\psi$  by the following two-scale difference relation [18, 17, 5]:

$$\begin{aligned} \psi(x) &= \varphi(2x) - \varphi(2x - 1), \\ \psi_k^j(x) &= \psi_{2k}^{j+1}(2^{j+1}x - 2k) + \psi_{2k+1}^{j+1}(2^{j+1}x - 2k - 1). \end{aligned} \quad (3.13)$$

The functions  $\varphi_k^j$  and  $\psi_k^j$  are orthonormal and dense in  $L^2(\mathbb{R})$  [18, 5, 20].

The definition on Equation 3.10 can be applied recursively in order to get any space  $V^n$  as long as one knows the first subspace  $V^0$  and one has a method for constructing the subspace  $W^m$  from  $V^0$  and  $W^{m-1}$

$$V^0 \oplus W^0 \oplus W^1 \oplus \dots \oplus W^{n-1} = V^n. \quad (3.14)$$

Projecting a function  $f(x)$  onto this basis would be then a weighted linear combination of the Haar functions, but taking into account the definition on Equation 3.14 one arrives at [5]

$$f(x) \approx \sum_k^{2^j-1} s_k^j \varphi_k^j = s_0^0 \varphi_0^0 + \sum_j^{N-1} \sum_k^{2^j-1} d_k^j \psi_k^j, \quad (3.15)$$

where  $d$  are the difference coefficients and  $s$  are the scaled averages of dyadic intervals of the function  $f(x)$ .

The scaling coefficients  $s_k^j$  are computed by the projection  $\langle \varphi_k^j(x) | f(x) \rangle$ . Likewise, the difference coefficients  $d_k^j(x)$  are computed by the projection  $\langle \psi_k^j(x) | f(x) \rangle$ . Because of the way the Haar function is defined, we can define the scaling coefficients as scaled averages of  $f(x)$  at intervals  $2^{-j}$  [5, 18]

$$s_k^j = \int_{\mathbb{R}} \varphi_k^j(x) f(x) dx = \int_{2^{-j}k}^{2^{-j}(k+1)} f(x) dx. \quad (3.16)$$

The subsequent scaling coefficients can be obtained as

$$\begin{aligned} s_k^j &= \int_{\mathbb{R}} \varphi_k^{j-1}(x) dx \\ &= 2^{\frac{j}{2}} \int_{\mathbb{R}} \varphi(2^j x - k) f(x) dx \\ &= 2^{\frac{j}{2}} \int_{2^{-j}(k-1)}^{2^{-j}k} f(x) dx. \end{aligned} \quad (3.17)$$

We can then obtain the difference coefficients by using Equations 3.16, 3.11 and 3.13:

$$\begin{aligned}
d_k^{j-1} &= \int_{\mathbb{R}} \psi_k^{j-1}(x) f(x) dx \\
&= 2^{\frac{j-1}{2}} \int_{\mathbb{R}} \psi(2^{j-1}x - k) f(x) dx \\
&= 2^{\frac{j-1}{2}} \left( \int_{\mathbb{R}} \varphi(2^j x - 2k) f(x) dx - \int_{\mathbb{R}} \varphi(2^j x - 2k - 1) f(x) dx \right) \\
&= 2^{\frac{j-1}{2}} \left( \int_{2^{-j}2k}^{2^{-j}(2k+1)} f(x) dx - \int_{2^{-j}(2k+1)}^{2^{-j}(2k+2)} f(x) dx \right) \\
&= \frac{1}{\sqrt{2}} (s_{2k}^j - s_{2k+1}^j).
\end{aligned} \tag{3.18}$$

The result of Equations 3.18 and 3.17 show us that we can represent the projection of coefficients onto a coarser scale as an orthogonal matrix [5, 18]:

$$\begin{pmatrix} d_k^j \\ s_k^j \end{pmatrix} = \begin{pmatrix} \frac{1}{\sqrt{2}} & -\frac{1}{\sqrt{2}} \\ \frac{1}{\sqrt{2}} & \frac{1}{\sqrt{2}} \end{pmatrix} \begin{pmatrix} s_{2k}^{j+1} \\ s_{2k+1}^{j+1} \end{pmatrix}. \tag{3.19}$$

Projecting the coefficients into a more refined scale is just a transpose of the above matrix:

$$\begin{pmatrix} s_{2k}^{j+1} \\ s_{2k+1}^{j+1} \end{pmatrix} = \begin{pmatrix} \frac{1}{\sqrt{2}} & \frac{1}{\sqrt{2}} \\ -\frac{1}{\sqrt{2}} & \frac{1}{\sqrt{2}} \end{pmatrix} \begin{pmatrix} d_k^j \\ s_k^j \end{pmatrix}. \tag{3.20}$$

### 3.2.3 Projecting a Gaussian function example

As an example, let us approximate the function  $f(x) = \frac{10}{\sqrt{\pi}} e^{-100(x-0.5)^2}$  in  $L^2(\mathbb{R})$  with Haar basis up to scale 5 using 3.15. This gives us the plots in the following Figure 3.1.

## 3.3 Multiwavelet MRA

### 3.3.1 Constructing the basis functions in one dimension

Following the same basics as in the Haar basis from the previous section we can define a hierarchical set of multiresolution spaces  $V_l^j$  where [21]

$$\begin{aligned}
V_l^j \stackrel{\text{def}}{=} \{ & f : \text{all polynomials of degree } \leq l \\
& \text{on } (2^{-j}k, 2^{-j}(k+1)) \text{ for } 0 \leq k < 2^n, \\
& f \text{ vanishes elsewhere} \}
\end{aligned} \tag{3.21}$$

and

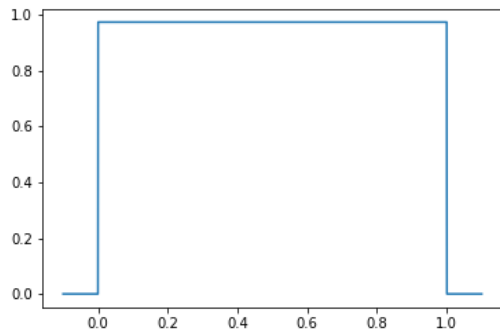
$$V_l^0 \subset V_l^1 \subset \dots \subset V_l^j \subset \dots \subset L^2(\mathbb{R}). \tag{3.22}$$

We again define subspaces  $W$ , as the orthogonal complements of  $V_j^l$  [19] defined as

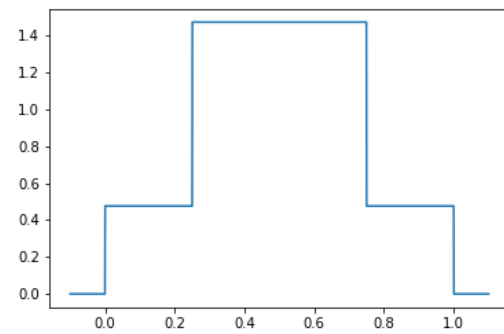
$$V_l^j \oplus W_l^j = V_l^{j+1}, \tag{3.23}$$

with orthogonal basis functions  $\psi_{lk}^j$  which are translations and dilations of functions  $\psi_i$

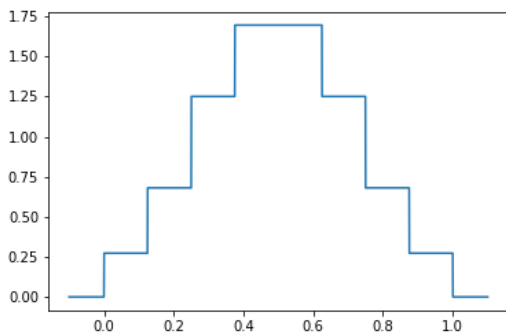
$$\psi_{ik}^j(x) = 2^{\frac{j}{2}} \psi_i(2^j x - k), \quad i = 1, \dots, l; \quad k \in \mathbb{Z}. \tag{3.24}$$



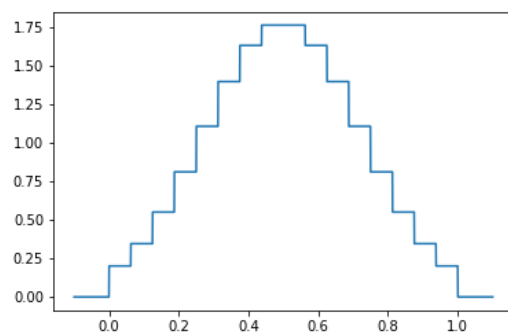
(a) Haar basis projection to the 1st scale



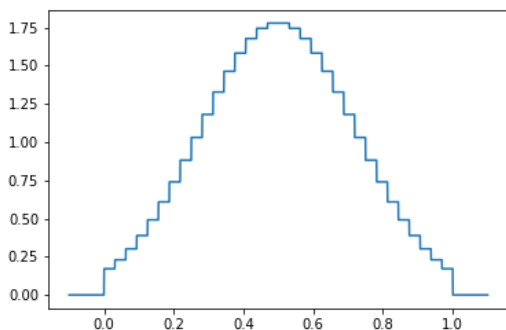
(b) Haar basis projection to the 2nd scale



(c) Haar basis projection to the 3rd scale



(d) Haar basis projection to the 4th scale



(e) Haar basis projection to the 5th scale

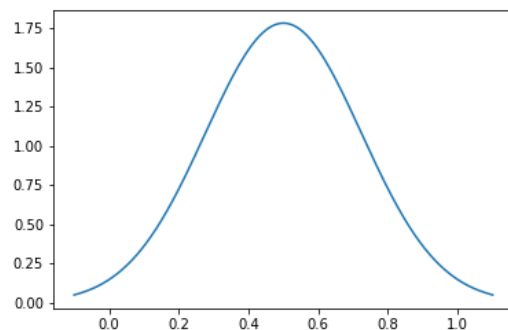
(f) Analytical plot of  $f(x)$ 

Figure 3.1: Projecting Gaussian function  $f(x) = \frac{10}{\sqrt{\pi}}e^{-100(x-0.5)^2}$  with Haar basis up to scale 5 on interval  $(0, 1)$

The functions  $\psi_1, \dots, \psi_l$  are piece-wise polynomial, orthogonal to lower order polynomials and vanish outside  $[0, 1]$  and their subscripts denote the polynomial order [19]

$$\int_0^1 \psi_i(x)x^m dx = 0, \quad m = 0, 1, \dots, l-1. \quad (3.25)$$

The basis functions  $\phi_i(x)$  of the subspace  $V_l^0$  can be defined using the following two-scale difference equations [22], which are analogous to the two-scale difference equations

in 3.13

$$\psi_i(x) = \sqrt{2} \sum_{j=0}^{l-1} \left( \bar{H}_{ij}^{(0)} \psi_j(2x) + \bar{H}_{ij}^{(1)} \psi_j(2x-1) \right), \quad i = 0, \dots, l-1, \quad (3.26)$$

$$\phi_i(x) = \sqrt{2} \sum_{j=0}^{l-1} \left( \bar{G}_{ij}^{(0)} \psi_j(2x) + \bar{G}_{ij}^{(1)} \psi_j(2x-1) \right), \quad i = 0, \dots, l-1, \quad (3.27)$$

where  $\bar{H}$  and  $\bar{G}$  are quadrature mirror filter matrices [22] which have the following properties:

$$\bar{H}^{(0)} \bar{H}^{(0)T} + \bar{H}^{(1)} \bar{H}^{(1)T} = \bar{I}, \quad (3.28)$$

$$\bar{G}^{(0)} \bar{G}^{(0)T} + \bar{G}^{(1)} \bar{G}^{(1)T} = \bar{I}, \quad (3.29)$$

$$\bar{H}^{(0)} \bar{G}^{(0)T} + \bar{H}^{(1)} \bar{G}^{(1)T} = \bar{0}, \quad (3.30)$$

which can be summarized in the orthogonal block matrix  $\bar{U}$  [22]

$$\bar{U} = \begin{pmatrix} \bar{H}^{(0)} & \bar{H}^{(1)} \\ \bar{G}^{(0)} & \bar{G}^{(1)} \end{pmatrix}. \quad (3.31)$$

This lets us put the two two-scale difference equations in the following way [5]

$$\begin{pmatrix} \vec{\psi}(x) \\ \vec{\phi}(x) \end{pmatrix} = \sqrt{2} \begin{pmatrix} \bar{H}^{(0)} & \bar{H}^{(1)} \\ \bar{G}^{(0)} & \bar{G}^{(1)} \end{pmatrix} \begin{pmatrix} \vec{\psi}(2x) \\ \vec{\psi}(2x-1) \end{pmatrix}, \quad (3.32)$$

and subsequently

$$\begin{pmatrix} \vec{\psi}(2x) \\ \vec{\psi}(2x-1) \end{pmatrix} = \frac{1}{\sqrt{2}} \begin{pmatrix} \bar{H}^{(0)} & \bar{G}^{(0)} \\ \bar{H}^{(1)} & \bar{G}^{(1)} \end{pmatrix} \begin{pmatrix} \vec{\psi}(x) \\ \vec{\phi}(x) \end{pmatrix}, \quad (3.33)$$

where the function vectors  $\vec{\phi}$  and  $\vec{\psi}$  represent the set of all  $l-1$  functions  $\phi_i$  and  $\psi_i$  of order  $i = 1, 2, \dots, l$  respectively.

### 3.3.2 Choices of scaling functions

Now that we have stated how to build the scaling and wavelet basis functions we need to make a choice of functions  $f$  to build said basis. Here we will briefly show two examples of polynomial functions used to create the basis. These two are the Legendre polynomials and the Lagrange interpolating polynomials [18, 22].

**Legendre basis** The Legendre scaling function is defined as follows

$$\phi_j(x) \begin{cases} \sqrt{2j+1} P_j(2x-1), & x \in [0, 1) \\ 0, & x \notin (0, 1) \end{cases}, \quad (3.34)$$

where  $P_j$  are the Legendre polynomials of order  $j$  defined in  $[-1, 1]$  [18]. Following are some examples of the polynomials together with figures of the first few terms of the functions. These functions have the advantage of being simple to compute, since each incremental polynomial order only adds a single term to the function.

### Lagrange interpolating basis

$$\varphi_i = \frac{1}{\sqrt{w_i}} l_i(x), \quad i = 0, \dots, M-1, \quad (3.35)$$

$$l_i(x) = \prod_{k=0, k \neq i}^{M-1} \frac{x - x_k}{x_i - x_k}, \quad (3.36)$$

$$w_i = \frac{1}{M \hat{P}'_M(2x_i - 1) P_{M-1}(2x_i - 1)}, \quad (3.37)$$

where  $M$  is the scale of the subspace, the  $P$  functions are the Legendre polynomials and  $x_0, \dots, x_{M-1}$  are the roots of  $P_M(2x-1)$  [18]. These scaling functions have the characteristic of  $l_i(x_j) = \delta_{ij}$  simplifying integrals and thus projections of the basis.

Going from one dimension to  $d$  dimensions is to use a tensor product method as shown in [21].

## 3.4 Operators

### 3.4.1 Non-standard form representation of operators

Let us define two projection operators  $\hat{P}^n$  and  $\hat{Q}^n$  and their relation as:

$$\hat{P}^n : L^2([0, 1]) \rightarrow V^n, \quad (3.38)$$

$$\hat{Q}^n : L^2([0, 1]) \rightarrow W^n, \quad (3.39)$$

$$\hat{P}^{n+1} = \hat{P}^n + \hat{Q}^n, \quad (3.40)$$

$$\hat{P}^n = \hat{P}^0 + \hat{Q}^0 + \hat{Q}^1 + \dots + \hat{Q}^{n-1}, \quad (3.41)$$

where we, for now, have dropped the polynomial order subscript  $l$  for ease of notation.

A function  $f$  would then be projected into a scale  $n$  by applying the operators as [21]

$$f^{(n)} = \hat{P}^n f. \quad (3.42)$$

Its projection onto a more refined scale would then be [21]

$$\begin{aligned} f^{(n+1)} &= f^{(n)} + df^{(n)}, \\ df^{(n)} &= \hat{Q}^n f. \end{aligned} \quad (3.43)$$

Following Equation 3.41 we can expand the equation above to

$$f^{(N)} = f^{(0)} + df^{(0)} + df^{(1)} + \dots + df^{(N-1)}, \quad (3.44)$$

which, for a given refinement level  $N$ , is a good approximation of  $f$

$$f \approx f^{(N)}. \quad (3.45)$$

The representation of a linear operator  $\hat{T}$  onto a scale  $n$  is

$$\hat{T}^n = \hat{P}^n \hat{T} \hat{P}^n, \quad (3.46)$$

and onto a more refined scale

$$\begin{aligned}\hat{T}^{n+1} &= \hat{P}^{n+1}\hat{T}\hat{P}^{n+1} \\ &= (\hat{P}^n + \hat{Q}^n)\hat{T}(\hat{P}^n + \hat{Q}^n) \\ &= \hat{P}^n\hat{T}\hat{P}^n + \hat{P}^n\hat{T}\hat{Q}^n + \hat{Q}^n\hat{T}\hat{P}^n + \hat{Q}^n\hat{T}\hat{Q}^n.\end{aligned}\tag{3.47}$$

We define a set of 3 operators which will help us describe the more refined operator  $\hat{T}$

$$\hat{A}^n \stackrel{\text{def}}{=} \hat{Q}^n\hat{T}\hat{Q}^n : W^n \rightarrow W^n,\tag{3.48}$$

$$\hat{B}^n \stackrel{\text{def}}{=} \hat{Q}^n\hat{T}\hat{P}^n : V^n \rightarrow W^n,\tag{3.49}$$

$$\hat{C}^n \stackrel{\text{def}}{=} \hat{P}^n\hat{T}\hat{Q}^n : W^n \rightarrow V^n,\tag{3.50}$$

so we can rewrite the last term in Equation 3.47 as

$$\hat{T}^{n+1} = \hat{A}^n + \hat{B}^n + \hat{C}^n + \hat{T}^n.\tag{3.51}$$

Repeating this iteratively we get

$$T^N = T^0 + \sum_{n=0}^N (\hat{A}^n + \hat{B}^n + \hat{C}^n),\tag{3.52}$$

which we can say, given a refinement level  $N$  is a good approximation of  $T$

$$T \approx T^N.\tag{3.53}$$

Let us now define a function  $g = \hat{T}f$  which is the resulting function from applying the unprojected operator  $\hat{T}$  onto the unprojected  $f$ . We want to represent this operation in the MW basis as

$$g^{(n)} = \hat{P}^n g = \hat{P}^n (\hat{T}f),\tag{3.54}$$

but we do not know what  $g$  looks like. We have the projected function  $f^{(n)}$  and the representation of the operator  $\hat{T}^n$ . We do the following set of manipulations to define a new projected function  $\tilde{g}^{(n)}$  [21]:

$$\begin{aligned}g^{(n)} &= \hat{P}^n g = \hat{P}^n (\hat{T}f) \\ &= \hat{P}^n \hat{T} (\hat{P}^n + 1 - \hat{P}^n) f \\ &= \hat{P}^n \hat{T} \hat{P}^n \hat{P}^n f + \hat{P}^n \hat{T} (1 - \hat{P}^n) f \\ &= \hat{T}^n f^{(n)} + \hat{P}^n \hat{T} (1 - \hat{P}^n) f, \\ \tilde{g}^{(n)} &\stackrel{\text{def}}{=} \hat{T}^n f^{(n)},\end{aligned}\tag{3.55}$$

where we know  $\hat{T}^n$  and  $f^{(n)}$  as defined above and we focus only in finding  $\tilde{g}^{(n)}$ . We substitute Equations 3.43 and 3.51 into the last term of Equation 3.55 to get

$$\tilde{g}^{(n)} = (\hat{A}^{n-1} + \hat{B}^{n-1} + \hat{C}^{n-1} + \hat{T}^{n-1}) (f^{(n-1)} + df^{(n-1)}),\tag{3.56}$$

$$\tilde{g}^{(n)} = \bar{g}^{(n-1)} + d\bar{g}^{(n-1)},\tag{3.57}$$

$$\bar{g}^{(n-1)} = (\hat{C}^{n-1} + \hat{T}^{n-1}) (f^{(n-1)} + df^{(n-1)}),\tag{3.58}$$

$$d\bar{g}^{(n-1)} = (\hat{A}^{n-1} + \hat{B}^{n-1}) (f^{(n-1)} + df^{(n-1)}),\tag{3.59}$$

and

$$\begin{aligned}
\hat{C}^{n-1} f^{(n-1)} &\approx 0 ; \hat{T}^{n-1} df^{(n-1)} \approx 0 \\
\bar{g}^{(n-1)} &\stackrel{\text{def}}{=} \hat{g}^{(n-1)} + \tilde{g}^{(n-1)} \\
\hat{g}^{(n-1)} &= \hat{C}^{n-1} df^{(n-1)} \\
\tilde{g}^{(n-1)} &= \hat{T}^{n-1} f^{(n-1)}
\end{aligned} \tag{3.60}$$

We find  $\bar{g}^{(0)}$  as

$$\bar{g}^{(0)} = \tilde{g}^{(0)} + \hat{g}^{(0)} = \hat{T}^0 f^{(0)} + \hat{C}^0 df^{(0)}, \tag{3.61}$$

and iteratively find  $\tilde{g}^{(n)}$  as [21]

$$\begin{aligned}
\tilde{g}^{(0)} &= \hat{T}^0 f^{(0)}, \\
\tilde{g}^{(1)} &= \bar{g}^{(0)} + d\bar{g}^{(0)} \\
&= \tilde{g}^{(0)} + \hat{g}^{(0)} + d\bar{g}^{(0)} \\
&= \hat{T}^0 f^{(0)} + \hat{C}^0 df^{(0)} + \left( \hat{A}^0 + \hat{B}^0 \right) \left( f^{(0)} + df^{(0)} \right), \\
\tilde{g}^{(2)} &= \bar{g}^{(1)} + d\bar{g}^{(1)} \\
&= \tilde{g}^{(1)} + \hat{g}^{(1)} + d\bar{g}^{(1)} \\
&= \bar{g}^{(0)} + d\bar{g}^{(0)} + \hat{g}^{(1)} + d\bar{g}^{(1)} \\
&= \tilde{g}^{(0)} + \hat{g}^{(0)} + d\bar{g}^{(0)} + \hat{g}^{(1)} + d\bar{g}^{(1)}, \\
&\vdots \\
\tilde{g}^{(N)} &= \hat{T}^0 f^{(0)} + \sum_{n=0}^N \hat{C}^n df^{(n)} + \left( \hat{A}^n + \hat{B}^n \right) \left( f^{(n)} + df^{(n)} \right),
\end{aligned} \tag{3.62}$$

and we assume that for a given refinement level  $N$  we have a good approximation of  $g$

$$\tilde{g}^{(N)} \approx g^N = (\hat{T}f)^N. \tag{3.63}$$

In multiple dimensions  $d$  we can expand the Non-Standard form into a tensor product of the four operators as shown in [21].

### 3.4.2 Examples of operators

#### Derivative operator

We let  $\hat{T}$  represent a derivative operator  $\frac{\partial}{\partial x}$  and  $\hat{T}_l^n$  represent its projection onto scale  $n$  with order  $l$  as defined as in Equation 3.46. For a function  $f$  for which we want to apply the operator on we define the expansions for  $\hat{P}_l^n$  and  $\hat{T}_l^n$  [22]

$$\begin{aligned}
\left( \hat{P}_l^n f \right) (x) &= \sum_{m=0}^{2^n-1} \sum_{j=0}^{l-1} s_{jm}^n \phi_{jm}^n(x), \\
\left( \hat{T}_l^n f \right) (x) &= \sum_{k=0}^{2^n-1} \sum_{i=0}^{l-1} \tilde{s}_{ik}^n \phi_{ik}^n(x),
\end{aligned} \tag{3.64}$$



where  $\phi$  and  $s$  are scaling coefficients and functions as defined above and  $\tilde{s}$  is

$$\tilde{s}_{ik}^n = \sum_{m=0}^{2^n-1} \sum_{j=0}^{l-1} [r_{km}^n]_{ij} s_{jm}^n, \quad (3.65)$$

where  $[r_{km}^n]$  is a  $l \times l$  transition matrix which we are trying to solve for

$$[r_{km}^n]_{ij} = \int_{2^{-n}k}^{2^{-n}(l+1)} \phi_{ik}^n(x) \frac{\partial}{\partial x} \phi_{jm}^n(x) dx = 2^{nd} [r_{k-m}]_{ij}, \quad (3.66)$$

$$[r_k]_{ij} = \int_0^1 \phi_i(x) \frac{\partial}{\partial x} \phi_j(x+k) dx. \quad (3.67)$$

Since the derivative operator is in-homogeneous we can represent it on scale  $n$  by rescaling by powers of two

$$r_{km}^n = 2^n r_{k-m}, \quad (3.68)$$

and given that the operator acts only on the neighboring intervals we can remove a sum from Equation 3.65 as follows

$$\tilde{s}_{ik}^n = 2^n \sum_{j=0}^{l-1} \left( [r_1]_{ij} s_{j,k-1}^n + [r_0]_{ij} s_{jk}^n + [r_{-1}]_{ij} s_{j,k+1}^n \right). \quad (3.69)$$

We can now introduce a vector multiplication notation for the sum in Equation 3.69

$$\begin{aligned} S^n &= (s_{00}^n, \dots, s_{l-1,0}^n, s_{01}^n, \dots, s_{l-1,1}^n, \dots, s_{0,2^n-1}^n, \dots, s_{l-1,2^n-1}^n)^T, \\ \tilde{S}^n &= (\tilde{s}_{00}^n, \dots, \tilde{s}_{l-1,0}^n, \tilde{s}_{01}^n, \dots, \tilde{s}_{l-1,1}^n, \dots, \tilde{s}_{0,2^n-1}^n, \dots, \tilde{s}_{l-1,2^n-1}^n)^T, \\ \bar{R}^n &= 2^n \{r_{k-m}\}_{k,m=0,\dots,2^n-1}, \end{aligned} \quad (3.70)$$

where Equation 3.69 can be rewritten into a matrix equation as

$$\tilde{S}^n = \bar{R}^n S^n, \quad (3.71)$$

$$\bar{R}^n = 2^n \begin{pmatrix} r_0 & r_{-1} & & & \\ r_1 & \ddots & \ddots & & \\ & \ddots & \ddots & r_{-1} & \\ & & r_1 & r_0 & \end{pmatrix}, \quad (3.72)$$

where each block  $r_i$  is a  $l \times l$  and  $r_1$  and  $r_{-1}$  describe the interactions between neighboring intervals [22]. Computations of this transition matrix  $\bar{R}$  are shown in [22] and there it is assumed that the rest of the operators  $\hat{A}^n$ ,  $\hat{B}^n$ ,  $\hat{C}^n$  are computed by rescaling the representation explained above.

### Poisson operator

In order to solve a system where an electrostatic field  $V$  is affected by a charge distribution  $\rho$  changes throughout space one attempts to solve a Poisson equation

$$\nabla^2 V = -4\pi\rho. \quad (3.73)$$

In MW one makes use of the Poisson operator  $\hat{\mathcal{P}}$  to find the electrostatic potential induced by the charge distribution

$$\hat{\mathcal{P}}[\rho(\vec{r})] = \int \frac{1}{4\pi \|r - r'\|} \rho(r') dr', \quad (3.74)$$

which is a simplified version of the Poisson kernel shown in [21]. The Poisson operator can be projected as is outlined in section 3.4.1 above.

### 3.5 SCF method in multiwavelet basis

When performing the SCF mentioned in chapter 2 one computes the sets of one-orbital eigenfunctions from Equation 2.47. Let us expand that equation into its single kinetic and potential energy contributions

$$\left( \hat{T} + \hat{V}_n + \hat{J} - \hat{K} + \hat{V}_{xc} \right) \phi_i = \epsilon_i \phi_i, \quad (3.75)$$

where  $\hat{V}_{xc}$  is the exchange-correlation potential, which is part of the DFT SCF and can be removed for HF. We will not dwell on it much more and assume it is known.

The kinetic energy operator  $\hat{T}$  from Equation 3.75 consists of a double derivative. We saw from the previous section on operators that representing a derivative operator on MW basis is not a simple matter. In order to solve this we need to represent the derivative operator in a slightly different manner.

First let us rearrange Equation 3.75 and multiply each side with operator  $\hat{G}_\mu$  which is much easier to project to the MW basis

$$\hat{G}_\mu = (\nabla^2 + \mu^2)^{-1} = \frac{e^{-\mu|\vec{r}|}}{4\pi|\vec{r}|}, \quad (3.76)$$

$$\mu \stackrel{\text{def}}{=} \sqrt{-2\epsilon_i}, \quad (3.77)$$

$$\begin{aligned} \hat{G}_\mu \left( \hat{T} - \epsilon_i \right) \phi_i &= -\hat{G}_\mu \left( \hat{V}_n + \hat{J} - \hat{K} + \hat{V}_{xc} \right) \phi_i, \\ (\nabla^2 + \mu^2)^{-1} \left( \frac{1}{2} \nabla^2 - \epsilon_i \right) \phi_i &= -(\nabla^2 + \mu^2)^{-1} \left( \hat{V}_n + \hat{J} - \hat{K} + \hat{V}_{xc} \right) \phi_i, \\ \frac{1}{2} \phi_i &= -\hat{G}_\mu \left( \hat{V}_n + \hat{J} - \hat{K} + \hat{V}_{xc} \right) \phi_i, \\ \phi_i &= -2\hat{G}_\mu \left( \hat{V}_n + \hat{J} - \hat{K} + \hat{V}_{xc} \right) \phi_i. \end{aligned} \quad (3.78)$$

Using the last equation above one can perform a SCF procedure by iteratively applying  $-2\hat{G}_\mu \left( \hat{V}_n + \hat{J} - \hat{K} + \hat{V}_{xc} \right)$  on an unconverged orbital to attain a new orbital. This process is then repeated until the change between the orbitals is below a predetermined threshold.

# Chapter 4

## Solvent Effect

In chapter 2 we saw how to approximate and solve systems of molecules in vacuum. This was done using both HF and DFT in iterative SCF procedures. Results obtained from these methods would then be used to determine certain properties, or observables, from these systems. Results obtained from systems in vacuum can be called gas phase values.

The goal of these computations are to both to approximate systems and to manage to make predictions in regards to these approximation. It makes sense then that one of the type of systems one would be most interested in approximating as a chemist are solvation systems. This is because most chemical processes of interest in chemistry, such as reaction mechanisms or acid-base reactions, happen in solvent.

Our aim is to be able to simulate a solvent system in an appropriate way, such that the models let us predict rates, mechanisms and other specific processes which occur in solutions [4].

A straightforward approach, consistent with the QM methods defined up to now, is to make a system a substrate atom surrounded by solvent molecules, all defined by quantum mechanical methods. One can imagine the substrate to be a single atom ion and the solvent to be water. The first problem that arises is the quantity of water molecules needed to simulate the solution system. A straight forward answer would be to have enough water molecules to surround the ion in one layer of them, and just do our calculations from that point.

Let us put the molecules in a cube-like fashion around the cation, with each water molecule in a face of the cube, totaling 6 water molecules. Our calculations could be performed from this point, but one should see that the system is ordered, and that it is not necessarily in a minimum with respect to the geometry. The next course of action should be to perform a geometry optimization on these 7 molecules, or 19 nuclei. The first problem with this method appears in these geometry optimization. Since we have so many nuclei, the PES will be affected by all of them simultaneously. This causes the PES to have many small, local minima, making it harder to find the global minimum of the surface [9]. This is still doable with full QM methods, given that these type of calculations are done on greater systems than just 19 nuclei, such as hydrocarbons, or small proteins.

Another question we can ask ourselves is how representative is this model to the real system we are trying to simulate. After all, the water molecules on a solvent interact with themselves and the substrate. As our model is now the water molecules are only interacting with the ones beside them, while elsewhere there are no other water molecules. Our model is representing a group of a substrate molecule surrounded by water molecules on a vacuum. This is not what we are trying to model. We can add more layers of water

molecules, so as to simulate the interactions of water with itself, but we will always have a set of water molecules facing vacuum. We can add water molecules until the amount of molecules facing vacuum is negligible with respect to the ones in a solvent environment. This will be an extremely big system suffering of a PES with many local minima and nuclei, making both geometry optimizations and energy calculations expensive [10].

The system explained above is both expensive and not representative of the system we are trying to model. Solvent models, presented in this chapter, present a solution to the dilemma above. These solvents models, which will be the focus of this chapter, reference the case of a very dilute solution, where we can assume the substrate is surrounded by the solvent only.

## 4.1 Outlining the problem

Solvation models describe one or more molecules (substrate) surrounded by a set of other molecules (solvent). Most reactions of interest occur in a solvent where the geometry, energy and kinetics of the reactants and products are affected by their environment[23].

We can describe the total Hamiltonian  $\hat{H}_{sol}$  of a solvent-solute system as [4]

$$\hat{H}_{sol} = \hat{H}_0 + \hat{V}_{sol}, \quad (4.1)$$

where  $H_0$  is the gas phase Hamiltonian (in vacuo) and  $\hat{V}_{sol}$  is the potential arising from the interactions between solvent and solute. These interactions can be considered as perturbations to the in vacuo system. The SE of the system is as follows [4]

$$\hat{H}_{sol}\Psi^{(f)} = E^{(f)}\Psi^{(f)}, \quad (4.2)$$

where  $f$  denotes the degree of rigidity of the interactions (0 being with completely static solvent molecules and rigidity decreasing with increasing index). In most practical uses, we are interested in the polarization interaction between the solvent and solute, meaning that one can replace the wave function  $\Psi$  with the total charge distribution of the solute  $\rho_{tot}$  [4]

$$\begin{aligned} \rho_{tot}(\vec{r}; \vec{Q}) &= \rho_{nuc}(\vec{r}; \vec{Q}) + \rho_{el}(\vec{r}; \vec{Q}), \\ \rho_{nuc}(\vec{r}; \vec{Q}) &= \sum_{\alpha} Z_{\alpha} \delta(\vec{r} - \vec{Q}_{\alpha}), \\ \rho_{el}(\vec{q}_1; \vec{Q}) &= - \int \left| \Psi^{(f)}(\mathbf{q}, \vec{Q}) \right|^2 d\vec{q}_2 \dots d\mathbf{q}_{N_{el}}, \end{aligned} \quad (4.3)$$

where  $\alpha$  is an index that iterates over all the nuclei of the molecule,  $Z_{\alpha}$  is the nuclear charge of each nucleus,  $\vec{q}_1, \dots, \vec{q}_{N_{el}}$  represents the coordinates of the electrons,  $\vec{Q}_{\alpha}$  represents the coordinates of the nuclei and  $\vec{r}$  is a vector variable describing a point in three dimensions.

There are four main interactions affected by solvent which one might be interested in solving. These are electrostatic interactions, cavitation, changes in dispersion and changes in bulk solvent structure [9]. In this thesis we work mostly with the electrostatics interactions of the solute-solvent interface and the reaction field they create.

### 4.1.1 Reaction field

Let us consider a system where a solute  $A$  with a dipole moment  $\vec{\mu}_A$  is introduced to a solvent  $S$  where each solvent molecule  $S_i$  has its own dipole moment  $\vec{\mu}_{S_i}$ . On equilibrium

the different  $S_i$  would be placed randomly, giving an average electric field of zero. When  $A$  is introduced, its  $\vec{\mu}_A$  will induce an electric field that will affect all the  $\vec{\mu}_{S_i}$  of the  $S_i$ . The  $S_i$  will reorient themselves so that their  $\vec{\mu}_{S_i}$  lie along the electric field induced by  $\vec{\mu}_A$ . This is so that they are in a more energetically favorable position in the electric potential of the field induced by  $\vec{\mu}_A$ , but in doing this, they will act against their own electric field and lose conformational freedom, which will cost energy. This will, in turn, change the electric field of  $S$  so that it no longer behaves uniformly. The electric field of  $S$  will then affect  $A$  so that  $\vec{\mu}_A$  lies along the new electric field of  $S$  for the same reason stated above, using free energy in doing so [9].

The process outlined above will repeat itself until the energy gain from reorienting  $A$  and  $S$  is outweighed by the required energy of such a reorientation. The energy at such a point is equal to half the total interaction energy between  $S$  and  $A$  [9]. The new field obtained at the equilibrium position of this interaction is called the reaction field  $U_r$  for the interaction of  $A$  and  $S$ . This interaction can be represented as a statistical average over all degrees of freedom of the interaction. This is done by replacing the solvent molecules with a continuous electric field that is affected by the introduction of the substrate. This is done so that one does not need to represent the charge distribution of the solvent explicitly [9], which can be expensive with bigger systems. Solvent models that represent the charge distribution explicitly are called explicit solvation models. The models that do not represent it explicitly are implicit solvation models.

## 4.2 Explicit solvation models

The explicit method is necessary when the solvent molecules' geometry and states are important to the measurement of the interactions of the substrate [9]. One way to simplify the problem is to partition the system into two parts, the solvent, modeled using molecular mechanics (MM) and the solute, modeled using QM, this method is called QM/MM [23].

The main point of this model is that the energy contribution from the solvent can be described as a sum of bonding and non-bonding contributions [9] where the solvent bonds are described as springs [23] and the atoms as weights. The bonding contributions can be divided into bending, stretching and torsion of the bonds. Both the bending and the stretching of the bonds can be described with the Harmonic Oscillator (HO) and the torsion with a periodic function [23]. The non-bonding interactions can be described with Coulomb's law, or other equivalent expressions of potentials, with the atoms as point charges. More information on this can be read on [9, 10].

## 4.3 Implicit solvation models

Most implicit models describe the solvent as a linear isotropic continuum characterized by the static dielectric constant  $\epsilon_{out}$  characteristic of the bulk of the solvent [4, 1]. In this continuum only the electrostatic interactions contribution are significant [4]. The energy needed to create a cavity in the continuum in which the substrate is contained and the dispersion and repulsion forces between the solvent and the substrate often cancel out, or at least the contribution becomes negligible [9]. This means that the interaction potential  $\hat{V}_{sol}$  in Equation 4.1 becomes an electrostatic potential  $\hat{V}_\sigma$  [4]

$$\hat{V}_{int} = \hat{V}_\sigma(\mathbf{q}, \mathbf{Q}, \rho_{tot}, \epsilon_{out}) = \sum_{\alpha} Z_{\alpha} U_r(\mathbf{Q}_{\alpha}) - \sum_i U_r(\mathbf{q}_i), \quad (4.4)$$

where  $U_r$  is the reaction field potential. The contribution of the interaction between the solvent and the substrate to the total energy  $E^{(f)}$  is given by

$$W_{tot} = \int_{\mathbb{R}^3} \Psi^{(f)*} \hat{V}_\sigma \Psi^{(f)} dq \dots dq_{N_{el}} = \langle \rho_{tot}(\vec{r}) | U_r(\vec{r}) \rangle. \quad (4.5)$$

This means that determining the reaction potential as well as knowing the coordinates of the different particles will solve the Equation 4.2. Since we are looking at the effect the charge distribution of a solute has on the interaction potential, we set up a Poisson equation. We also know that the change in the potential must also be related to the dielectric constant that characterizes the continuum  $\epsilon$ . We try to find the solution to the following electrostatic potential equation, also called the GPE

$$\nabla(\epsilon(\vec{r})\nabla U(\vec{r})) = -4\pi\rho_{tot}, \quad (4.6)$$

where  $U(\vec{r})$  is the electrostatic potential of the interaction between the solute and the solvent.

There are two main ways of solving the GPE that are implemented in PCMs. These are either direct solutions of Equation 4.6, or introducing boundary conditions where the Volumes inside and outside the cavity are separated by the a two dimensional cavity surface. In the latter method the problem is solved at the surface and is represented as an apparent surface charge  $\sigma$  distributed along the surface.

### 4.3.1 Cavity

All continuum models make use of a cavity in which the solute  $A$  resides [4, 9, 2]. The shape of the cavity must be defined so it includes the whole molecule  $A$  and its charge distribution. Although, since the charge distribution of any molecule persists to infinity there will always be an overlap with the charge distributions of the medium in real systems. The charge that is not contained within the cavity is often called escaped charge [2].

The size of the cavity is critical to the calculated results of the model, if the cavity is too big the solvation effects are dampened, if it is too small various errors may arise in the computation of the interactions to be studied [4]. The cavity shape should closely resemble the shape of the molecule itself [2]. There are two main ways of defining the shape and size of the cavity: (1) regular shapes and (2) molecular shapes.

Regular shapes such as spheres, cylinders and ellipsoids have the advantage of faster and simpler computations than molecular shapes. The fact that the cavity should resemble the molecule and its charge distributions still stands, and it is not realistic to assume that all molecules have regular shapes (apart from maybe single atoms and linear molecules) [2].

Molecular shapes give a better representation of the solute in the solvent due to the fact that they more closely follow the shape of the solute molecule. There are three main molecular shapes I wish to mention: interlocking spheres, surfaces traced by solvent probes and isodensity surfaces.

#### Molecular surface shapes

**The interlocking spheres model** The interlocking spheres model consists of creating spheres centered at the nuclei of the molecule. Other centers can be in functional groups, so that they envelope a whole group, or in specially designated spaces around the molecule

so that they give an accurate representation of the parts of the substrate molecule the solvent has access to [4]. The latter is explained more in the next section.

The consensus for the radius of each cavity  $R_i$  is that it has to be close to the van der Waals (vdW) radius  $R_{vdw}$  of the atom the sphere is centered in. One of the most used set of radii for this are the radii provided by Bondi [24, 2] and are generally scaled by a coefficient  $f$  that is close to 1. The following relation holds [4]

$$R_i = fR_{vdw}, \quad (4.7)$$

where  $f$  has been found to be, by statistical analysis,  $f = 1.2 \pm 0.1$  in order to yield the best results. Its value is 1.2 for water while it can vary with other solvents [4]. Although this only stands for neutral solutes. Some results imply that the best radius for cations is the covalent radius and the best one for anions is the ionic radius [4].

**Solvent probe tracing surfaces** This family of surfaces are based on the interlocking spheres model in that a solvent probe (normally a spherical probe) is rolled around the interlocking sphere surface to trace a new surface. The inwards facing face of the probe traces a surface which the solvent cannot access. This surface is called the Solvent Excluded Surface (SES) [2, 23]. One can think of this as smoothing so as to not get polarization in areas around the molecule which should not be accessible to the solvent. Both SAS and SES are shown in the following Figure 4.1

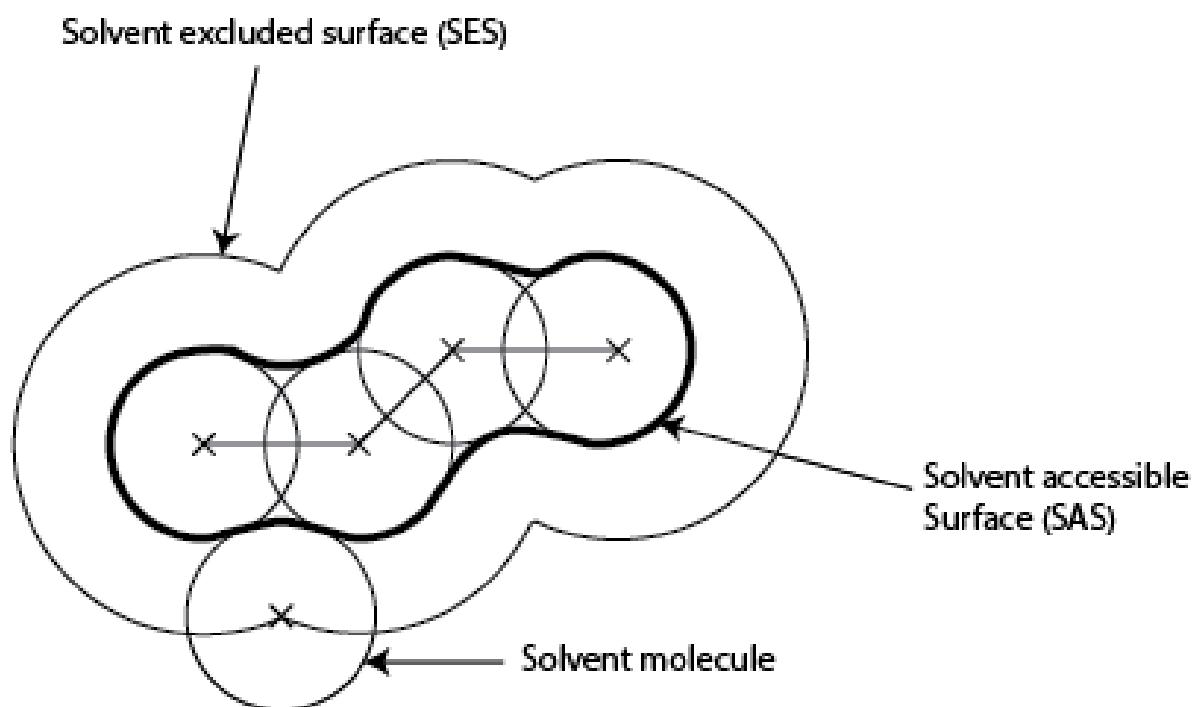


Figure 4.1: SAS and SES surfaces

**Isodensity surfaces** A third type of surface is one defined by a certain value of the charge density. This is usually defined by setting a threshold value of the charge density for which the surface will be drawn (usually 0.0004 – 0.001 a.u.)[2].

### 4.3.2 Boundary conditions

As stated before, in continuum models the solvent is represented by an isotropic continuum defined by the dielectric constant  $\epsilon_{out}$  characteristic to the bulk solvent [4]. The interface between the solute and the continuum is the cavity. One way to think of the value of the continuum is by defining a function epsilon with the cavity as a boundary condition [2, 4]

$$\epsilon(\vec{r}) = \begin{cases} \epsilon_{out} & \text{for } \vec{r} \in C \\ 1 & \text{for } \vec{r} \notin C \end{cases}, \quad (4.8)$$

where  $C$  is the cavity. We then solve the polarization problem at the surface of the cavity. We define an Apparent surface charge  $\sigma$  which defines the polarization of the electric field as charges at the surface of the cavity. Apparent surface charge methods are used to solve for the polarization. We define this problem by partitioning the volume of the system into two parts, one inside the cavity and one outside the cavity [4]. Another assumption that is made is to say that we have an ideal charge distribution that does not reach outside the cavity [9, 4]. This means that [4]

$$\rho_{tot}(\vec{r}) = 0 \quad \vec{r} \notin C. \quad (4.9)$$

This lets us define the Poisson equation inside and outside the cavity as follows [5, 4]:

$$\begin{aligned} \nabla^2 U(\vec{r}) &= -4\pi\rho_{tot}(\vec{r}) \quad \vec{r} \in C, \\ \epsilon_{out}\nabla^2 U(\vec{r}) &= 0 \quad \vec{r} \notin C, \end{aligned} \quad (4.10)$$

where, for a point  $\vec{s}$  and a normal outwards vector  $\vec{n}$  on the surface of the cavity, the following conditions are true [5, 4]

$$\begin{aligned} U_{in}(\vec{s}) &= U_{out}(\vec{s}), \\ \frac{\partial U_{in}}{\partial \vec{n}} &= \epsilon_{out} \frac{\partial U_{out}}{\partial \vec{n}}, \end{aligned} \quad (4.11)$$

where  $U(\vec{r})$  is the sum of the potential of the substrate in vacuo  $U_{vac}$  and the reaction field potential  $U_r$ [5, 1]

$$U(\vec{r}) = U_{vac}(\vec{r}) + U_r(\vec{r}). \quad (4.12)$$

### 4.3.3 Approaches to a solution

#### Apparent surface charge

In this family of solutions we look at the classical electrostatics description of the problem. we do this by defining an apparent charge distribution  $\sigma$  confined to the surface of the cavity  $\Gamma$  [4, 2]. The apparent surface charge distribution at the boundary between two regions  $i, j$  is defined as

$$\sigma_{ij} = -(\vec{P}_j - \vec{P}_i) \cdot \vec{n}_{ij}, \quad (4.13)$$



where  $\vec{n}_{ij}$  is the unit vector pointing from  $i$  to  $j$  and  $\vec{P}$  is the polarization vector of a region of constant isotropic permittivity (such as the continuum in PCM) defined as

$$\vec{P}_i(\vec{r}) = -\frac{\epsilon_i - 1}{4\pi} \nabla U(\vec{r}), \quad (4.14)$$

where  $\epsilon_i$  is the permittivity constant of region  $i$  [2]. In a solvation model we only have two regions, one inside and one outside. We know that  $\epsilon_{in} = 1$  so  $\vec{P}_0 = 0$  leaving only the outside region to construct  $\sigma$ . This gives us [2]

$$\sigma(\vec{s}) = \frac{\epsilon_{out} - 1}{4\pi\epsilon_{out}} \frac{\partial}{\partial \vec{n}} (U_{vac} + U_\sigma)_{in}; \quad s \in \Gamma, \quad (4.15)$$

and we find the reaction potential of the apparent surface charge  $U_\sigma$  with the following integral

$$U_\sigma(\vec{r}) = \int_\Gamma \frac{\sigma(\vec{s})}{|\vec{r} - \vec{s}|} d\vec{s}; \quad s \in \Gamma, \quad (4.16)$$

If we divide the surface into a set of finite elements, tesserae [2, 5], with set areas  $A$  that are small enough to be able to assume that  $\sigma$  does not change inside each of these tesserae, will let us define the integral as a sum over all the tesserae

$$U_\sigma(\vec{r}) \simeq \sum_k \frac{\sigma(\vec{s}_k) A_k}{|\vec{r} - \vec{s}_k|} d\vec{s} = \sum_k \frac{q_k}{|\vec{r} - \vec{s}_k|}, \quad (4.17)$$

where  $q_k = \sigma(\vec{s}_k) A_k$  is the point charge of each tesserae [2]. Many slightly different types of Apparent Surface Charge (ASC) have been implemented as of now. Some of these are Conductor-like Screening model (COSMO), Integral equation formalism (IEF) and Surface and Volume Polarization for Electrostatic (SVPE).

**COSMO** In this version of ASC we proceed as normal except that we define  $\epsilon_{out} = \infty$ . This way we determine the ASC ( $\sigma^*$ ) by the local value of the electrostatic potential instead of computing the normal component of its gradient [2]. We then scale  $\sigma^*$  as

$$\sigma(\vec{s}) = \frac{\epsilon_{out} - 1}{\epsilon_{out} + k} \sigma^*(\vec{s}), \quad (4.18)$$

where  $k$  is small [2].

**IEF** In this method we define the electrostatic potentials in terms of Green integral functions. The Green function  $G(\vec{x}, \vec{y})$  is the potential produced at a point  $\vec{x}$  by a unit charge at  $\vec{y}$  [2]. We define the electrostatic potentials as follows

$$\begin{aligned} U(x) &= \int_{R^3} G^s(x, y) \rho_M(y) dy, \\ U_{vac}(x) &= \int_{R^3} G(x, y) \rho_M(y) dy, \\ U_r(x) &= \int_{R^3} G^r(x, y) \rho_M(y) dy, \end{aligned} \quad (4.19)$$

where  $G(\vec{x}, \vec{y}) = 1/|\vec{x} - \vec{y}|$  is the Green kernel for the operator  $-\nabla^2$ ,  $G^s(\vec{x}, \vec{y})$  is the Green function of  $-\nabla(\epsilon(\vec{r})\nabla)$  and  $G^r(x, y) = G^s(\vec{x}, \vec{y}) - G(\vec{x}, \vec{y})$ . Then the reaction potential  $U_r$  can be represented as [2]

$$U_r(x) = \int_{\Gamma} \frac{\sigma(\vec{y})}{|\vec{x} - \vec{y}|} d\vec{y} \forall \vec{x} \in R^3, \quad (4.20)$$

where the surface charge  $\sigma$  is given by solving the following equation

$$\left[ 2\pi \left( \frac{\epsilon + 1}{\epsilon - 1} \right) - D_i \right] S_i \sigma = - (2\pi - D_i) V_{vac}, \quad (4.21)$$

where  $S_i$  and  $D_i$  are two of the four components of the Calderon projector [2].

**SVPE** The main focus of this method is that the solute charge distribution has a trailing "tail" that reaches outside the surface [2]. We define the reaction potential as consisting of a ASC term  $U_\sigma$  and a exterior term  $U_\beta$

$$\begin{aligned} U_r(\vec{x}) &= U_\sigma(\vec{x}) + U_\beta(\vec{x}), \\ U_\beta(\vec{x}) &= -\frac{\epsilon_{out} - 1}{\epsilon_{out}} \int_{ext} \frac{\rho_{tot}(\vec{y})}{|\vec{x} - \vec{y}|} d\vec{y}, \end{aligned} \quad (4.22)$$

where  $x, y$  are defined as above.

### Multipole expansion

In this solution we write the total electrostatic potential  $U(\vec{r})$  in terms of Legendre polynomials. This way the potential is reduced to a set of two spherical harmonics functions, one outside and one inside the cavity.

$$\begin{aligned} U_{in}(\vec{r}) &= \sum_{l=0}^{\infty} \frac{1}{r^{l+1}} \sum_{m=-l}^l B_{lm} Y_l^m(\theta, \phi) \\ &+ \sum_{l=0}^{\infty} \frac{(l+1)(\epsilon_{out} - 1)}{l + (l+1)\epsilon_{out}} \frac{r^{l+1}}{a^{2l+1}} \sum_{m=-l}^l B_{lm} Y_l^m(\theta, \phi), \\ U_{out}(\vec{r}) &= \sum_{l=0}^{\infty} \frac{2l+1}{l + (l+1)\epsilon_{out}} \frac{1}{r^{l+1}} \sum_{m=-l}^l B_{lm} Y_l^m(\theta, \phi), \end{aligned} \quad (4.23)$$

where  $Y_l^m$  is the spherical harmonics with angular momentum  $l$  and projection along the z-axis  $m$ ,  $a$  is the radius of the cavity and  $B_{lm}$  is a set of constants which need to be found [4]. It goes without saying that since we are using spherical harmonics, the cavities used in this method must be spherical. Some methods exist to work with ellipsoidal cavities and even interlocking spheres, which are outlined in [4] and [2].

### 4.3.4 Solving the generalized Poisson equation in multiwavelet basis

Following Fosso–Tande [1] the cavity is defined as a molecular shape interlocking spheres cavity. We start by defining a normal signed distance function  $s_i$  of a point  $\vec{r}$  away from the surface of the sphere  $C_i$  with radius  $R_i = 1.2 \cdot R_i^{vdw}$  and centered on atom  $i$  with coordinate  $\vec{r}_i$  [1]

$$s_i(\vec{r}) = |r - r_i| - R_i. \quad (4.24)$$

The cavity for the  $i$ -th atom is defined as

$$C_i(\vec{r}) = 1 - \Theta(s_i(\vec{r})) = \Theta(-s_i(\vec{r})), \quad (4.25)$$

where  $\Theta$  is a heavyside-like function that enables to smoothly transition from the inside of the cavity (value 1), to the surface of the cavity (value  $\frac{1}{2}$ ) and to the outside of the cavity (value 0) [5, 1]. We use the error function  $\text{erf}(x)$  to define  $\Theta$  and a parameter  $\sigma$  characterizing the width of the transition between the inside and outside of the cavity

$$\Theta(s_i) = \frac{1}{2} \left( 1 + \text{erf} \left( \frac{s_i}{\sigma} \right) \right). \quad (4.26)$$

The function for the complete set of interlocking spheres  $C$  for a molecule with  $N$  atoms is given by

$$C(\vec{r}) = 1 - \prod_{i=1}^N (1 - C_i(\vec{r})). \quad (4.27)$$

This function can then be used further in creating a dielectric function  $\epsilon$  that switches smoothly from  $\epsilon_{in}$  (permittivity of free space with value 1 [1]) to  $\epsilon_{out}$  either with a linear representation

$$\epsilon(\vec{r}) = \epsilon_{out} + (\epsilon_{in} - \epsilon_{out})C(\vec{r}), \quad (4.28)$$

or with an exponential representation

$$\epsilon(\vec{r}) = \epsilon_{in} \exp \left( \left( \log \frac{\epsilon_{out}}{\epsilon_{in}} \right) (1 - C(\vec{r})) \right), \quad (4.29)$$

which is better suited for the computation of its log-derivative. This is important because differentiating the dielectric function directly will give us a slope that is not entirely centered at the cavity surface, which gives rise to instabilities in the results [1]. The log-derivative for the exponential representation is defined as [1]

$$\nabla \log \epsilon(\vec{r}) = \frac{\nabla \epsilon(\vec{r})}{\epsilon(\vec{r})} = \left( \log \frac{\epsilon_{in}}{\epsilon_{out}} \right) \nabla C(\vec{r}). \quad (4.30)$$

The log derivative of the linear dielectric function is expressed as

$$\nabla \log (\epsilon(\vec{r})) = \frac{\nabla \epsilon(\vec{r})}{\epsilon(\vec{r})} = \frac{(\epsilon_{in} - \epsilon_{out})}{\epsilon(\vec{r})} \nabla C(\vec{r}). \quad (4.31)$$

With either of those dielectric functions, the GPE can be constructed [5, 1]

$$\nabla \cdot (\epsilon(\vec{r}) \nabla U(\vec{r})) = -4\pi \rho_{tot}(\vec{r}), \quad (4.32)$$

$$\nabla^2 U(\vec{r}) = -4\pi \frac{\rho_{tot}}{\epsilon(\vec{r})} - \frac{\nabla \epsilon(\vec{r}) \cdot \nabla U(\vec{r})}{\epsilon(\vec{r})}. \quad (4.33)$$

We define the effective charge distribution  $\rho_{eff}$  and the surface charge distribution  $\gamma_s$  [1]

$$\rho_{eff}(\vec{r}) = \frac{1}{\epsilon(\vec{r})} \rho_{tot}(\vec{r}), \quad (4.34)$$

$$\gamma_s(\vec{r}) = \frac{1}{4\pi} \frac{\nabla \epsilon(\vec{r})}{\epsilon(\vec{r})} \cdot \nabla U(\vec{r}), \quad (4.35)$$

and substitute them into Equation 4.32

$$\nabla^2 U(\vec{r}) = -4\pi(\rho_{eff}(\vec{r}) + \gamma_s(\vec{r})). \quad (4.36)$$

Which, if we were to define  $\rho$  as entirely contained in the cavity, would mean that the polarization is completely defined by  $\gamma_s$  and Equation 4.36 would take the form of Equation 4.15. This means that  $\gamma_s$  is equivalent to  $\sigma$ . We get the total iteration potential  $U(\vec{r})$  between the substrate and the solvent by applying the Poisson operator  $\hat{\mathcal{P}}$  as defined in Equation 3.74 to equation 4.36

$$U(\vec{r}) = \hat{\mathcal{P}}(\rho_{eff}(\vec{r}) + \gamma_s(\vec{r})). \quad (4.37)$$

We can then find the reaction potential following Equation 4.12 and rearranging it so we get the following

$$U_r(\vec{r}) = U(\vec{r}) - U_{vac}(\vec{r}). \quad (4.38)$$

The reaction field energy is given as [1]

$$E_{tot} = -E_{vac} + \frac{1}{2}E_r, \quad (4.39)$$

$$E_r = \langle U_r | \rho_{tot} \rangle. \quad (4.40)$$

and  $E_{vac}$  is the gas phase energy of the substrate. This means that we can easily add the energy contributions from the reaction field to the SCF energy as a simple addition.

Since the solution of the total potential has itself in both sides of the equation we will need to iterate with an initial guess. This is called SCRF and will be implemented more thoroughly in Chapter 5.

## 4.4 Variational formulation of the Generalized Poisson equation

Following Lipparini [3, 25] I'll arrive at a functional where minimizing with respect to  $U$  of the solvent energy contribution to the total energy  $G_s$  will give a way to determine  $U_r$  variationally.

Starting from the GPE defined from [1] we project it into a suitable space with test functions  $\psi$

$$\begin{aligned} \nabla(\epsilon \nabla U) &= -4\pi\rho, \\ -\langle \psi | \nabla | \epsilon \nabla U \rangle &= 4\pi \langle \psi | \rho \rangle. \end{aligned} \quad (4.41)$$

Applying the following vector identity

$$\nabla(\psi \epsilon \nabla U) = \nabla \psi \epsilon \nabla U + \psi \nabla \epsilon \nabla U + \psi \epsilon \nabla^2 U, \quad (4.42)$$

we get the integral

$$-\int_{\mathbb{R}^3} \psi \nabla \epsilon \nabla U dr - \int_{\mathbb{R}^3} \psi \epsilon \nabla^2 U dr = \int_{\mathbb{R}^3} \nabla \psi \epsilon \nabla U dr - \int_{\mathbb{R}^3} \nabla(\psi \epsilon \nabla U) dr. \quad (4.43)$$

The test functions vanish at infinity. Applying Gauss' theorem [25] we can turn the rightmost integral into an integral on the surface, thus vanishing. This gives us

$$-\langle \psi | \nabla | \epsilon \nabla U \rangle = \langle \nabla \psi | \epsilon | \nabla U \rangle, \quad (4.44)$$

which we substitute into Equation 4.41

$$\langle \nabla \psi | \epsilon | \nabla U \rangle = 4\pi \langle \psi | \rho \rangle, \quad (4.45)$$

which lets us write the functional for the energy as [3]

$$G(U) = \frac{1}{8\pi} \langle \nabla U | \epsilon | \nabla U \rangle - \langle U | \rho \rangle. \quad (4.46)$$

We now find the gradient of the functional in order to minimize with respect to  $U$

$$\begin{aligned} \frac{\delta}{\delta U} G(U) &= \frac{\partial}{\partial U} G - \nabla \cdot \frac{\partial}{\partial \nabla U} G \\ &= -\nabla \cdot \frac{1}{8\pi} \frac{\partial}{\partial U} \langle \nabla U | \epsilon | \nabla U \rangle - \frac{\partial}{\partial U} \langle U | \rho \rangle \\ \frac{\delta}{\delta U} G(U) &= \frac{1}{4\pi} \epsilon \nabla U - \rho \end{aligned} \quad (4.47)$$

where, if we set  $\frac{\delta}{\delta U} G(U) = 0$  we get the GPE from [1] and thus we can use any type of minimization method to reach the right potential.



# Chapter 5

## Implementation of the generalized Poisson equation

### 5.1 Generalized Poisson equation on multiwavelet basis

In the following chapter we will outline our implementation of the GPE for solvent systems. We took Fosso–Tande’s and Harrison’s paper in [1] as a starting point. There they defined how to solve a GPE that included a dielectric function which was analytical through the cavity boundary. This model was explained with more detail in chapter 4 and it will not be explained again.

#### 5.1.1 Cavity Function

The first step was to create a cavity function as in [1]. This was done by creating a cavity object that stored the coordinates of nuclei  $\vec{r}_I$  and their characteristic radii  $R_I$ . When a point  $\vec{r}$  is evaluated in the Cavity function it will return 0 if it is outside and 1 if it is inside and will have a sigmoidal shape at the boundary of the Interlocking spheres cavity defined by the nuclei coordinates and their radii. Additionally we wanted to be able to change the width of the boundary with a parameter  $\sigma$ . The structure of the cavity object is as in Algorithm 1

This Object was implemented as a derived class of `RepresentableFunction`, a C++ class in `MRCHEM` .

#### 5.1.2 Dielectric Function

In Equations 4.29 and 4.28 we defined both a linear  $\epsilon_{lin}(\vec{r})$  and exponential  $\epsilon_{exp}(\vec{r})$  dielectric function. These were implemented as presented in those two equations, with no changes to them, except for minor syntax related adjustments. Their log derivatives had to be implemented separately, this was done in order to have better convergence [1]. The log derivative of the exponential dielectric function is represented as the derivative of the Cavity multiplied by a constant. The cavity of water as implemented above can be seen in Figure 5.1 as a slice through the  $xz$  plane.

**Algorithm 1** Cavity object**Initialize**  $C(\vec{r})$ **Input** : Molecular Coordinates, Radii, Width $\sigma \leftarrow$  WidthSet  $C_{tot}(\vec{r}) = 1$ **for** All Nuclei  $I$  **do** $\vec{r}_I \leftarrow$  Molecular Coordinate $_I$  $R_I \leftarrow$  Radius $_I$ **end for****When Evaluating**  $C(\vec{r})$ **Input:**  $\vec{r}$ **for** All Nuclei  $I$  **do** $s_I(\vec{r}) = |\vec{r} - \vec{r}_I| - R_I$  $\Theta_I(\vec{r}) = \frac{1}{2} \left( 1 + \operatorname{erf} \left( \frac{s_I(\vec{r})}{\sigma} \right) \right)$  $C_I(\vec{r}) = 1 - \Theta_I(\vec{r})$  $C_{tot}(\vec{r}) \leftarrow C_{tot}(\vec{r}) \cdot (1 - C_I(\vec{r}))$ **end for****return**  $1 - C_{tot}(\vec{r})$ 

## Atom based Cavity for water

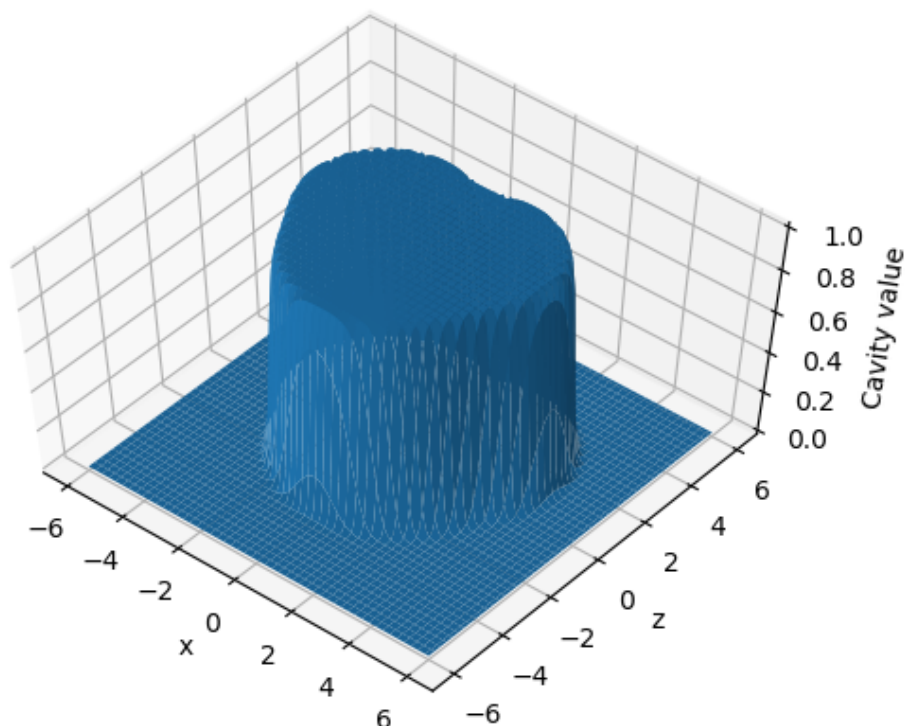


Figure 5.1: Interlocking spheres cavity function slice for water as implemented in algorithm 1



### 5.1.3 Effective volume charge distribution

When Running a SCF calculation one calculates with electron densities in order to solve an electron SE as is consistent with the BO approximation [9, 26], whereas the GPE needs the total molecular density  $\rho_{tot}$ . This is computed as a sum of the electron density  $\rho_{el}$  and the nuclear density  $\rho_{nuc}$  based on the geometry and charge of the nuclei

$$\rho_{tot} = \rho_{el} + \rho_{nuc} \quad (5.1)$$

. Algorithm 2 shows how we calculated the nuclear density  $\rho_{nuc}$  for the total density by use of point charges represented as Gaussian functions centered at each nucleus.

---

#### Algorithm 2 Nuclear charge density

---

**Input :** Nuclear coordinates,  $Z_I$

$\alpha = 1000$

$\beta = \left(\frac{\alpha}{\pi}\right)^{\frac{3}{2}} \cdot Z_I$

$\vec{r}_I(\vec{r}) =$  Nuclear coordinate $_I$

Set  $\rho_{nuc} = 0$

**for** All nuclei  $I$  **do**

$\rho_I(\vec{r}) = \beta e^{-\alpha \cdot \|\vec{r} - \vec{r}_I\|^2}$

$\rho_{nuc}(\vec{r}) = \rho_{nuc}(\vec{r}) + \rho_{nuc}^{(I)}(\vec{r})$

**end for**

**return**  $\rho_{nuc}(\vec{r})$

---

Where  $\alpha$  represents the width of the Gaussian function,  $\beta$  is the normalization constant multiplied with the charge,  $\vec{r}_I$  is the position of the nucleus and  $\rho_{nuc}^{(I)}$  is the Gaussian representing the a point charge at the nucleus.

We then go on to create the effective volume charge distribution by the following equation.

$$\rho_{eff} = \frac{1 - \epsilon}{\epsilon} \rho_{tot} \quad (5.2)$$

This differs from Fosso–Tande’s effective charge distribution in that we incorporate the subtraction of  $U_{vac}$  to it from the start [1]. This way we will be solving directly for the reaction field potential  $U_r$ . The alternative is to instead compute the total potential  $U$  and then subtract the gas phase potential to get the Reaction potential as in [1]. Calculating the Reaction potential with the latter method brings loss of accuracy by adding numerical noise.

### 5.1.4 Surface charge distribution

Given the total interaction potential of  $U$  of a solvation system with dielectric function  $\epsilon$  defined with cavity  $C$ , we compute the surface charge distribution  $\gamma_s$  as shown in algorithm 3.

In algorithm 3 we use the definition of the log derivative for both  $\epsilon_{lin}(\vec{r})$  and  $\epsilon_{exp}(\vec{r})$  from equations 4.30 and 4.31. This is the same as just writing

$$\gamma_s = \frac{1}{4\pi} \frac{\nabla \epsilon \nabla U}{\epsilon},$$

which is the same equation as in 4.34.

---

**Algorithm 3** Surface charge distribution

---

$\gamma_s[U, \epsilon[C]]$ :  
**Input** :  $U$  potential,  $\epsilon[C]$  dielectric function  
**if**  $\epsilon$  is exponential **then**  
 $k = \frac{1}{4\pi} \log \frac{\epsilon_{in}}{\epsilon_{out}}$   
**return**  $k \nabla C \cdot \nabla U$   
**else if**  $\epsilon$  is linear **then**  
 $k = \frac{1}{4\pi} (\epsilon_{in} - \epsilon_{out})$   
**return**  $\frac{k}{\epsilon} \nabla C \cdot \nabla U$   
**end if**

---

### 5.1.5 The iterative SCRF method

In this method we Compute the Reaction field of the solvation system by iteration. Here we follow the equation for the Reaction field potential in section 4.3.4. In that section we see that, in order to compute the reaction potential, we need to compute the surface charge distribution of the reaction potential. This paradox is resolved by an iterative process. In this section I will explain how this process works.

The first potential that is calculated will be a gas phase potential  $U_{vac}$  this potential is found by applying the Poisson operator  $\hat{\mathcal{P}}$  defined in Equation 3.74 on only the total charge density  $\rho_{tot}$ . This is then used to make the zeroth Surface charge distribution  $\gamma_s^{(0)}$ . This zeroth gamma is then added to the effective volume charge distribution  $\rho_{eff}$  and the Poisson operator is applied to the sum in order to get the reaction potential. This reaction potential is then used next iteration if the SCRF to compute the first surface charge distribution, which is then used to compute the next and so on. This is done until the norm of the difference between the previous reaction potential and the new one is less than a user defined precision. This is shown in Algorithm 4. The SCRF can then be

---

**Algorithm 4** SCRF iterative method

---

**Zeroth iteration:**  
 $U_{vac} \leftarrow \hat{\mathcal{P}}(\rho_{tot})$   
 $\gamma_s^{(0)} \leftarrow \gamma_s[U_{vac}, \epsilon]$   
 $U_r^{(1)} \leftarrow \hat{\mathcal{P}}(\rho_{eff} + \gamma_s^{(0)})$   
**n-th iteration:**  
**Input** : precision  
error = 10  
**while** error  $\geq$  precision **do**  
 $\gamma_s^{(n)} \leftarrow \gamma_s[(U_{vac} + U_r^{(n)}), \epsilon]$   
 $U_r^{(n+1)} \leftarrow \hat{\mathcal{P}}(\rho_{eff} + \gamma_s^{(n)})$   
error =  $\|U_r^{(n+1)} - U_r^{(n)}\|$   
 $U_r^{(n)} \leftarrow U_r^{(n+1)}$   
**end while**  
**return**  $U_r^{(n)}$

---

implemented by itself inside a SCF cycle. The converged Reaction potential for water in a water solvent can be seen in Figure 5.2.

## 5.2 Variational implementation

The variational implementation is very similar to the iterative one described. All the steps outlined above are the same during the first SCF cycle. Except that in the end, we compute the next  $\gamma_s^{(n)}$  with the converged  $U_r$  before moving on to the next SCF cycle. This  $\gamma_s^{(n)}$  is then used in the next cycle to compute only one iteration of the SCRF without checking the error against the precision. After the one iteration we use the new  $U_R$  to compute the  $\gamma_s^{(n+1)}$  for the next iteration. If one is using a convergence accelerator one can make use of the old surface charge distribution  $\gamma_s^{(n)}$  and the new one just computed  $\gamma_s^{(n+1)}$  to accelerate the convergence of the Reaction field potential. This is outlined in algorithm 5. Where  $\gamma_s^{(n+1)'} is an optimized  $\gamma_s^{(n+1)}$  which is used in the next iteration. The$

---

### Algorithm 5 SCRF variational method

---

#### Zeroth step:

Do The iterative SCRF  $\rightarrow U_r^{(converged)}$

$$\gamma_s^{(n+1)} \leftarrow \gamma_s[(U_{vac} + U_r^{(converged)}), \epsilon]$$

#### n-th step:

**On every SCF cycle do**

$$\gamma_s^{(n)} \leftarrow \gamma_s^{(n+1)}$$

$$U_r^{(n+1)} \leftarrow \hat{\mathcal{P}}(\rho_{eff} + \gamma_s^{(n)})$$

$$U_r^{(n)} \leftarrow U_r^{(n+1)}$$

$$\gamma_s^{(n+1)} \leftarrow \gamma_s[(U_{vac} + U_r^{(n)}), \epsilon]$$

$$\text{Accelerator}[\gamma_s^{(n)}, \gamma_s^{(n+1)}] \rightarrow \gamma_s^{(n+1)'}$$

$$\gamma_s^{(n+1)} \leftarrow \gamma_s^{(n+1)'}$$


---

first Iterative SCRF was done so that we would start the Optimizing of the potential with an already good guess.

## 5.3 Software used

The problem was first implemented in VAMPYR [27] which is a python interface to the MRCPP [28] code. Then it was implemented in C++ using MRChem [29]. All of the above software are MW software developed at Hylleraas centre of Quantum molecular sciences. Both implementations are identical, except for slight changes for performance improvement, such as using a KAIN accelerator,

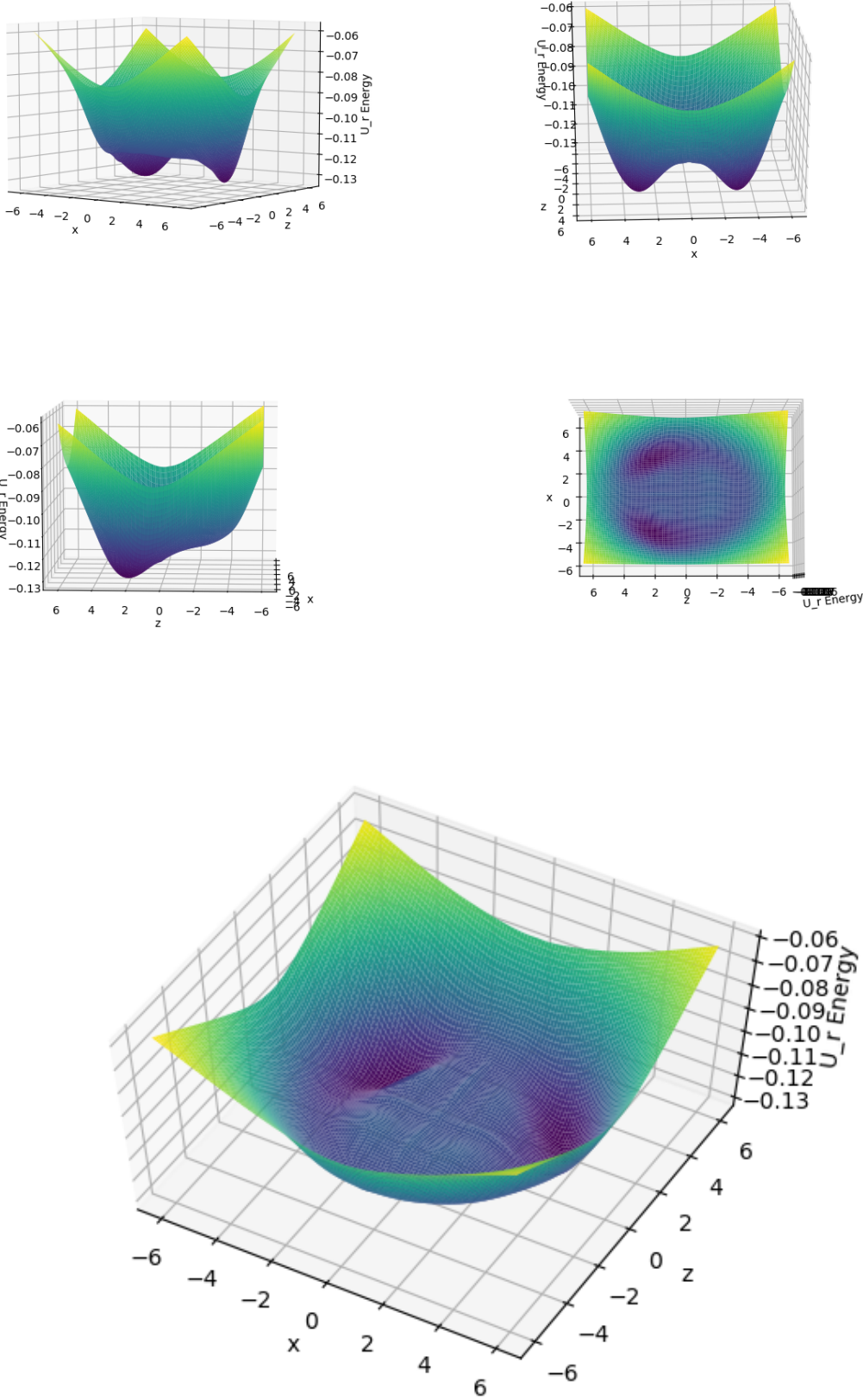


Figure 5.2: Reaction potential of water across the XZ plane

# Chapter 6

## Results

### 6.1 Overview of tests

We divided the tests of this implementation into four main types, (1) theoretical correctness, (2) parametrization, (3) comparison and (4) tests of the variational implementation.

1. **Theoretical correctness:** In the tests of theoretical correctness we test if our implementation gives the results to problems as expected. The tests for this were comparisons to the energy of  $\text{Li}^+$  in an environment with dielectric constant  $\epsilon_{out}$  with the value we would get from the Born model. In the Born model the energy of a one-atom ion in a solvent is the same as the energy of a point charge in the same solvent. This energy is described as [4]

$$E_R^{Born} = -\frac{\epsilon - 1}{2\epsilon} \frac{q^2}{R} \quad (6.1)$$

In the Born model the cavity is defined as a sharp two-dimensional surface. Because of this it is not expected that our results, with a smooth cavity, should converge to the same values as the Born model. A second comparison was done with Gauss' theorem[5] where we tested for the following relation that should hold for a point charge

$$\int \gamma_s dr = \frac{1 - \epsilon_{out}}{\epsilon_{out}} q \quad (6.2)$$

the integral evaluates the reaction charge of the system.

2. **Parametrization:** The parametrization tests were done by changing one parameter at a time while comparing this same change to Gaussian calculations with different basis sets. First we only checked the dependency on the radius and how changing it would affect the reaction field energy with respect to Gaussian calculations of the same radii. We then compared Gaussian calculations of radius  $R$  against MRCHEM calculations of radius  $R+0.2$  in an attempt to see an improvement in the results. A second parametrization test was done with only  $\text{Li}^+$  where we changed the relative precision of the MRCHEM calculations to see how they affect the energy with respect to the Gaussian energies. This was also done on different radii.
3. **Comparison:** We then took 4 molecules that were tested by Chipman in [30] and compared the results from the computations against Gaussian results. The molecules used were  $\text{H}_2\text{O}$ ,  $\text{NO}^+$ ,  $\text{CN}^-$  and  $\text{CH}_3\text{CONH}_2$ . These tests are classified

into spherical cavity tests and molecular-shaped cavity tests. Spherical cavity tests are performed by varying the radius of the cavities for each molecule. The spherical cavity test was done for all molecules except for  $\text{CH}_3\text{CONH}_2$  as it was too big, which made calculations in both Gaussian and MRCHEM extremely slow.

The molecular-shaped cavity tests consist of making interlocking spheres centered on each atom with radius equal to the atom's van der Waals radius. The set of radii by Bondi [24] are scaled by 1.2 as outlined by [4]. These radii were later shifted by 0.2 Bohr so that we were comparing MRCHEM calculations of bigger radii to Gaussian calculations.

4. **Variational tests:** As stated before in Chapters 4 and 5 a variational formulation of the reaction field Problem was implemented in this thesis, The tables in Appendix A show a row which is labeled "Variational", though the variational implementation behaved in a irregular way. We will show the reaction energy plots for the variational implementation for both  $\text{H}_2\text{O}$  and  $\text{Li}^+$  as those are the ones that had the most data points. We leave the reader to evaluate the variational energies for the other molecules.

All MRCHEM tests were done with relative precision of  $1e - 6$ , HF method and `SAD_DZ` as a starting guess [29]. All Gaussian calculations were ran with HF method, Dunning's correlation consistent basis sets[31] of increasing completeness, `scrf(pcm, read)` option with `nocav`, `nodis` and `norep` keywords. Both Gaussian and MRCHEM computations were run with optimized geometries from Gaussian using `b3lyp/cc-pVQZ`.

## 6.2 Data

### 6.2.1 Theoretical correctness tests

We calculated the integral on the left hand side of Equation 6.2 for a point charge with charge  $q = 3$  and compared it to the exact value calculated as shown in the right hand side of the same equation. This is shown in Tables 6.1 and 6.2.

We then evaluated the reaction field energy of the same point charge and compared it to an exact value calculated as in Equation 6.1. Tables 6.3 and 6.4 show this.

For both the tests above we calculated the values with two radii,  $R = 3.0, 4.0$  Bohr, two sets of dielectric constants,  $\epsilon_{out} = 2, 80$ , two transition widths,  $\sigma = 0.1, 0.2$ , and two values for the relative precision,  $1e - 4, 1e - 6$ .

Radius	Prec.	$\sigma = 0.2$	Rel. Diff.	$\sigma = 0.1$	Rel. Diff.
3.0	1E-04	-1.499964	-2.41E-05	-1.504559	3.04E-03
	1E-06	-1.499999	-7.43E-07	-1.500001	4.17E-07
4.0	1E-04	-1.499602	-2.66E-04	-1.503913	2.61E-03
	1E-06	-1.500002	1.21E-06	-1.499659	-2.27E-04
Exact		-1.500000		-1.500000	

Table 6.1: Reaction charge for a point charge of  $q = 3$  and  $\epsilon_{out} = 2$  calculated with differing precision, transition width ( $\sigma$ ) and cavity radius (Bohr) compared to the exact values

Radius	Prec.	$\sigma = 0.2$	Rel. Diff.	$\sigma = 0.1$	Rel. Diff.
3.0	1.00E-04	-2.96495	8.26E-04	-2.96167	-2.81E-04
	1.00E-06	-2.96250	2.92E-07	-2.96235	-5.16E-05
4.0	1.00E-04	-2.96400	5.06E-04	-2.95605	-2.18E-03
	1.00E-06	-2.96243	-2.20E-05	-2.96215	-1.17E-04
Exact		-2.96250		-2.96250	

Table 6.2: Reaction charge for a point charge of  $q = 3$  and  $\epsilon_{out} = 80$  calculated with differing precision, transition width ( $\sigma$ ) and cavity radius (Bohr) compared to the exact values

Radius	Born energy	Prec.	$\sigma = 0.2$	Rel. Diff.	$\sigma = 0.1$	Rel. Diff.
3.0	-0.7500	1E-04	-0.7586	1.14E-02	-0.7560	7.96E-03
		1E-06	-0.7586	1.15E-02	-0.7539	5.15E-03
4.0	-0.5625	1E-04	-0.5670	7.95E-03	-0.5660	6.27E-03
		1E-06	-0.5671	8.17E-03	-0.5645	3.53E-03

Table 6.3: Reaction field energy for a point charge of  $q = 3$  and  $\epsilon_{out} = 2$  calculated with differing precision, transition width ( $\sigma$ ) and cavity radius (Bohr) compared to the values from the Born model

Radius	Born energy	Prec.	$\sigma = 0.2$	Rel. Diff.	$\sigma = 0.1$	Rel. Diff.
3	-1.48125	1.00E-04	-1.55781	5.17E-02	-1.51700	2.41E-02
		1.00E-06	-1.55658	5.09E-02	-1.51731	2.43E-02
4	-1.1109375	1.00E-04	-1.15306	3.79E-02	-1.12961	1.68E-02
		1.00E-06	-1.15241	3.73E-02	-1.13093	1.80E-02

Table 6.4: Reaction field energy for a point charge of  $q = 3$  and  $\epsilon_{out} = 80$  calculated with differing precision, transition width ( $\sigma$ ) and cavity radius (Bohr) compared to the values from the Born model

## 6.2.2 Parametrization Tests

We first varied the radius of the cavity for H<sub>2</sub>O and lithium. The following Table 6.5 presents the data for the energy calculations of H<sub>2</sub>O with the three first cavity radii used in the calculations. These are the total energy of the system including the solvent effect contributions.

Basis	vacuum E	3.6	3.7	3.8
cc-pVDZ	-76.02663793	-76.03908811	-76.03763579	-76.03641832
cc-pVTZ	-76.05697112	-76.07006812	-76.06851635	-76.06721439
cc-pVQZ	-76.06463074	-76.07784858	-76.07628127	-76.07496499
cc-pV5Z	-76.06688831	-76.08017253	-76.07860146	-76.07728122
aug-cc-pVDZ	-76.04126545	-76.05445572	-76.05289986	-76.05159320
aug-cc-pVTZ	-76.06042913	-76.07366704	-76.07209913	-76.07078170
aug-cc-pVQZ	-76.06580140	-76.07902254	-76.07745594	-76.07613970
aug-cc-pV5Z	-76.06711902	-76.08034209	-76.07877365	-76.07745617
daug-cc-pVDZ	-76.04174340	-76.05497166	-76.05340824	-76.05209489
daug-cc-pVTZ	-76.06052322	-76.07376602	-76.07219809	-76.07088031
daug-cc-pVQZ	-76.06582414	-76.07904691	-76.07748036	-76.07616414
daug-cc-pV5Z	-76.06712250	-76.08034610	-76.07877753	-76.07745995
mrchem	-76.06728320	-76.08531969	-76.08277751	-76.08071980

Table 6.5: Total Energy Calculations example for H<sub>2</sub>O in Water. Energy in Hartree and radii of the cavity in Bohr

To calculate the reaction field energy we took a gas phase calculation of a basis set and subtracted it from the total energy calculated with the same basis set. In MRCHEM this was done using the same relative precision for both the gas phase and the solvent calculations. The following equation was used to calculate the reaction field Energy  $E_r$

$$E_r = E_{tot} - E_{vac} \quad (6.3)$$

Examples of  $E_r$  for the first three cavity radii for H<sub>2</sub>O obtained from the operation in Equation 6.3 can be seen in Table 6.6

The Tables 6.5 and 6.6 do not show the total amount of results that were used to plot the Energies. The results for the remaining radii can be seen in Appendix A.

We now plot the data from the total energy and reaction energy tables for both H<sub>2</sub>O and Li<sup>+</sup>. In this chapter we will be plotting only against double augmented basis sets. The rest of the plots for the other basis sets can be seen in Appendix B.

The plots for the reaction energy of H<sub>2</sub>O for both the Gaussian and MRCHEM calculations can be seen in Figure 6.1. The same type of plots for Li<sup>+</sup> can be seen in Figure 6.2. In both of these figures we are comparing the energy from MRCHEM to sets of four curves formed each of double, triple, quadruple and quintuple zeta Dunning's correlation consistent basis sets[31] as implemented in Gaussian [32].

The MRCHEM energy values  $E_{MRCHEM}$  for each radius were compared to the corresponding values of each of the different basis set calculations in Gaussian  $E_{Gaussian}^{basis}$  by finding the relative difference  $d_r$  between them as

$$d_r = \frac{E_{Gaussian}^{basis} - E_{MRCHEM}}{E_{MRCHEM}} \quad (6.4)$$



basis	3.6	3.7	3.8
cc-pVDZ	-0.01245017	-0.01099786	-0.00978039
cc-pVTZ	-0.01309700	-0.01154523	-0.01024327
cc-pVQZ	-0.01321784	-0.01165053	-0.01033425
cc-pV5Z	-0.01328422	-0.01171314	-0.01039291
aug-cc-pVDZ	-0.01319027	-0.01163442	-0.01032775
aug-cc-pVTZ	-0.01323791	-0.01167000	-0.01035257
aug-cc-pVQZ	-0.01322114	-0.01165454	-0.01033831
aug-cc-pV5Z	-0.01322306	-0.01165463	-0.01033715
daug-cc-pVDZ	-0.01322826	-0.01166484	-0.01035150
daug-cc-pVTZ	-0.01324280	-0.01167487	-0.01035709
daug-cc-pVQZ	-0.01322276	-0.01165622	-0.01033999
daug-cc-pV5Z	-0.01322360	-0.01165503	-0.01033745
mrchem	-0.01803648	-0.01549431	-0.01343659

Table 6.6: [ $E_r$  for H<sub>2</sub>O in Water sample]Reaction Field Energy Calculations example for H<sub>2</sub>O in water, Energy in Hartree and radii of the cavity in Bohr

The operation in Equation 6.4 was applied to both H<sub>2</sub>O and Li<sup>+</sup>. The results for H<sub>2</sub>O and Li<sup>+</sup> are presented in Figures 6.3 and 6.4 respectively.

We then shifted the cavity radius of the MRCHEM calculations for both H<sub>2</sub>O and Li<sup>+</sup> so they were 0.2 Bohr bigger and compared them to Gaussian calculations with an unshifted radius. The relative Difference plots for H<sub>2</sub>O and Li<sup>+</sup> can be seen in Figures 6.5 and 6.6 respectively.

Lastly we computed the reaction field energies of Li<sup>+</sup> with four different relative precision;  $1e-3$ ,  $1e-4$ ,  $1e-5$ , and  $1e-6$ . We compared these to the reaction field energies calculated with the most complete basis set: **daug-cc-pV5Z** as described in 6.4 Figure 6.7 shows the plots of the operation in Equation 6.4 as applied to the different precision values of the MRCHEM calculations for Li<sup>+</sup>. First all of the relative differences plotted together, then the second one contains only the results for relative precision  $1e(-4)$ ,  $1e(-5)$ , and  $1e(-6)$  since the results with relative precision  $1e(-3)$  are over five times larger than the other ones.

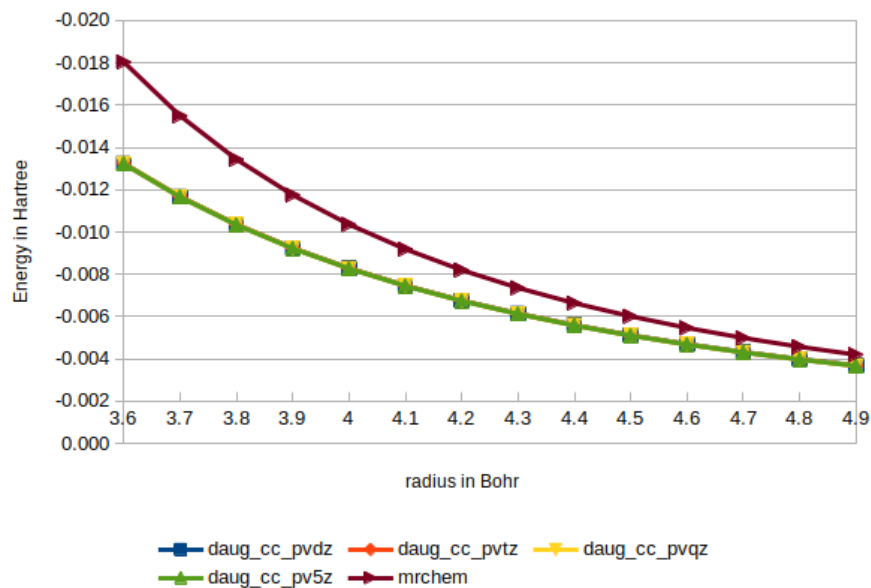


Figure 6.1: Reaction field energy of  $\text{H}_2\text{O}$  in a water solution, calculated with relative precision  $e - 05$  in MRCHEM and with double augmented basis sets in Gaussian

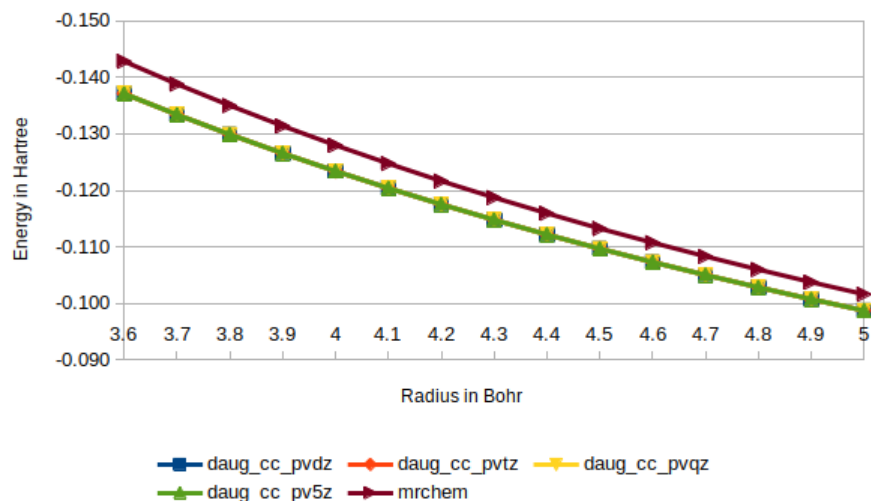


Figure 6.2: Reaction field energy of  $\text{Li}^+$  in a water solution, calculated with relative precision  $e - 05$  in MRCHEM and with double augmented basis sets in Gaussian

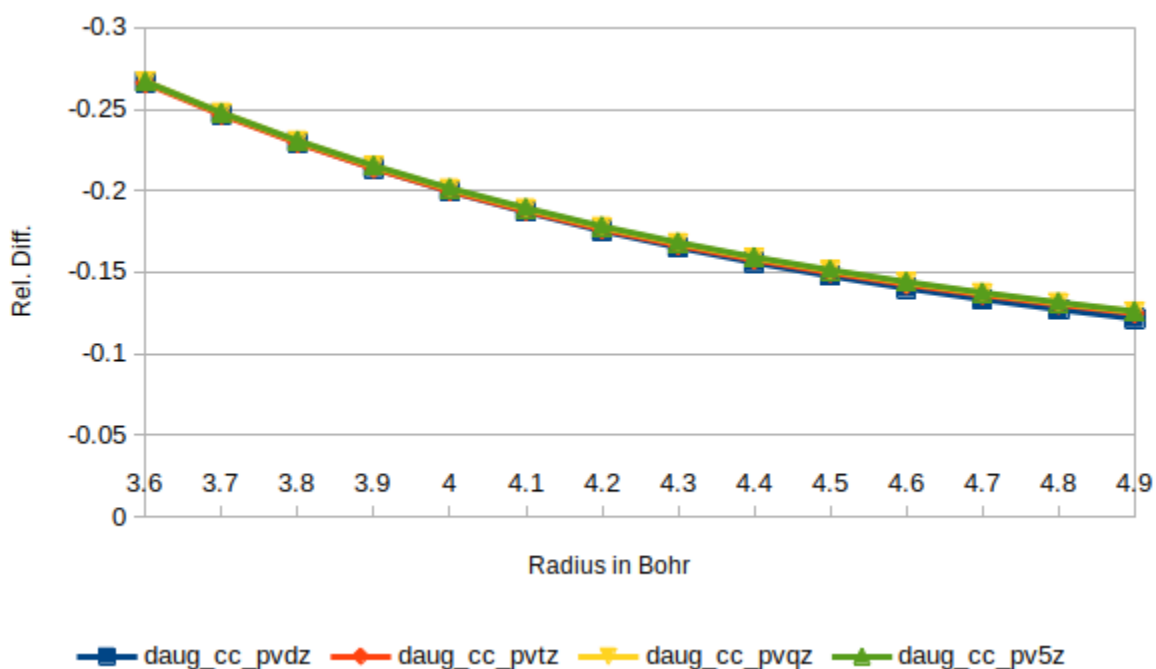


Figure 6.3: Relative difference between the reaction field energy of  $\text{H}_2\text{O}$  in a water solution calculated with with relative precision  $e-05$  in MRCHEM against double augmented basis sets in Gaussian

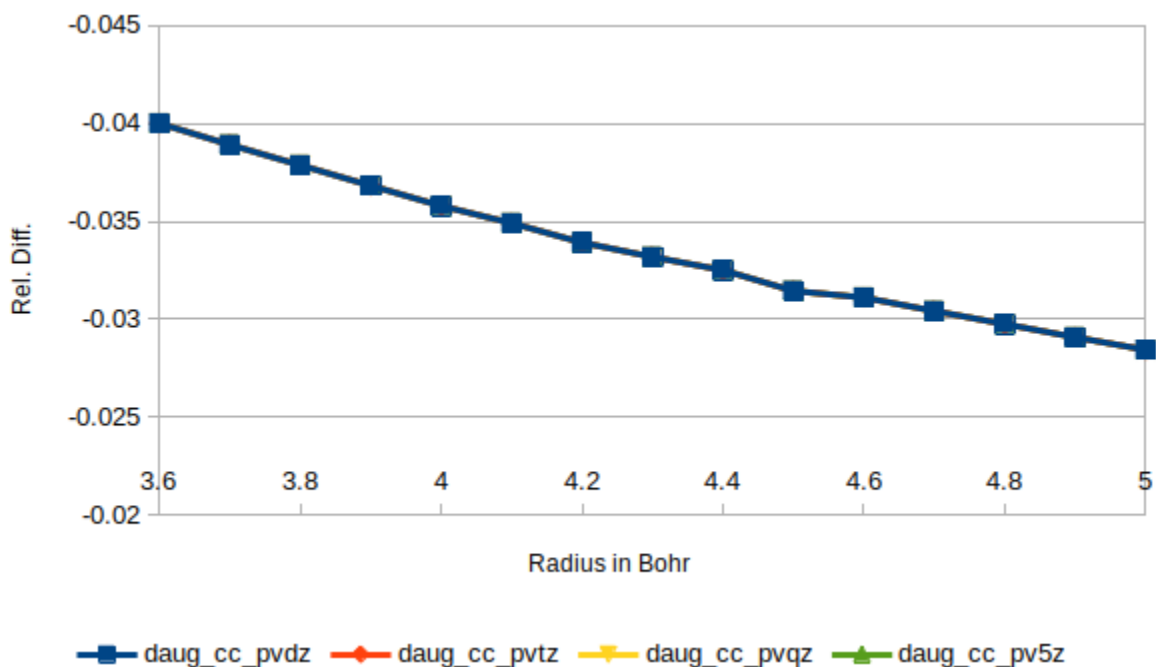


Figure 6.4: Relative difference between the reaction field energy of  $\text{Li}^+$  in a water solution calculated with relative precision  $e-05$  in MRCHEM and with double augmented basis sets in Gaussian

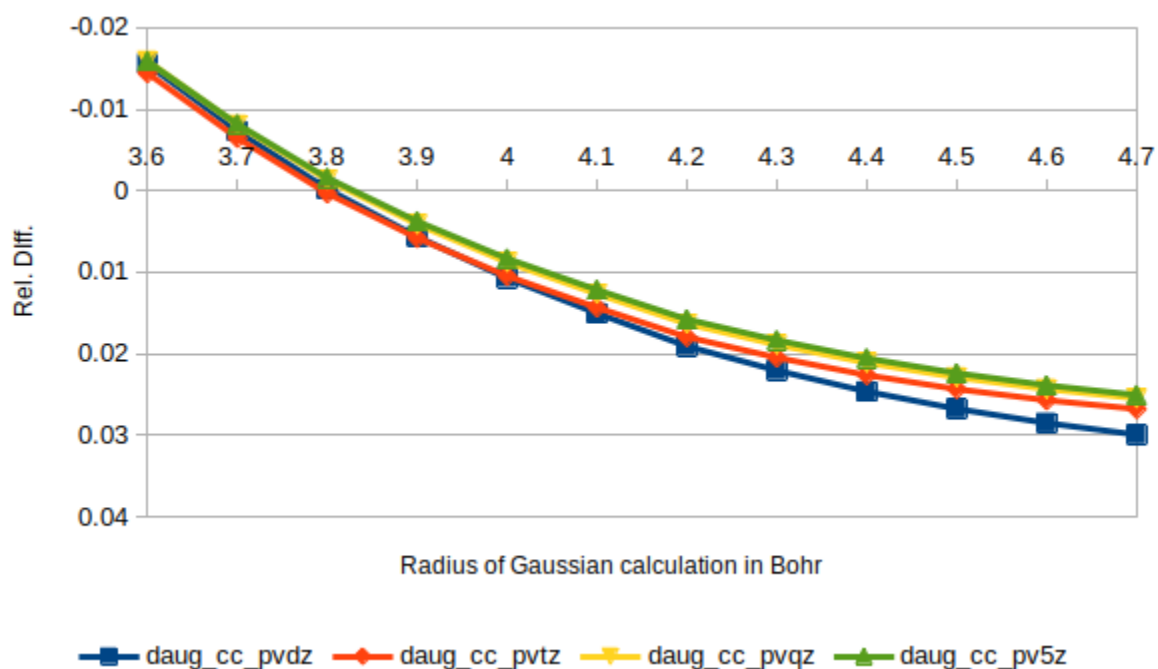


Figure 6.5: Relative difference between the reaction field energy of  $\text{H}_2\text{O}$  in a water solution calculated with with relative precision  $e - 05$  in MRCHEM and radius  $+0.2$  Bohr and with double augmented basis sets in Gaussian

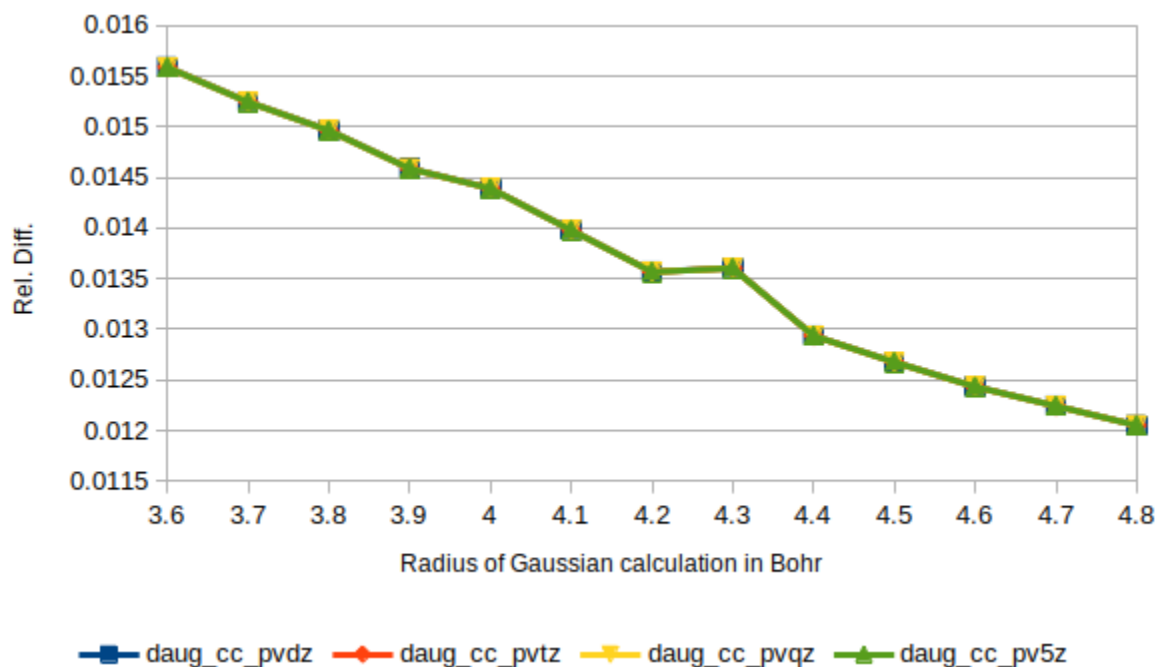
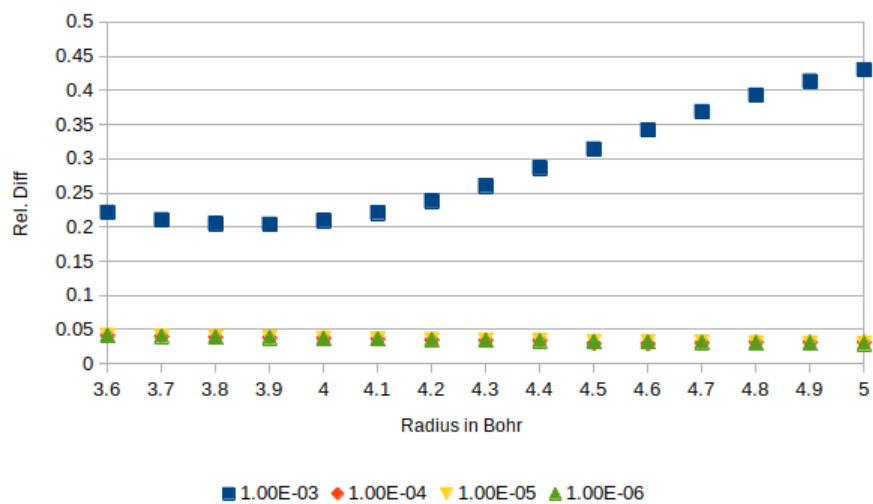


Figure 6.6: Relative difference between the reaction field energy of  $\text{Li}^+$  in a water solution calculated with relative precision  $e - 05$  in MRCHEM and radius  $+0.2$  Bohr and with double augmented basis sets in Gaussian



(a) All precision values plotted

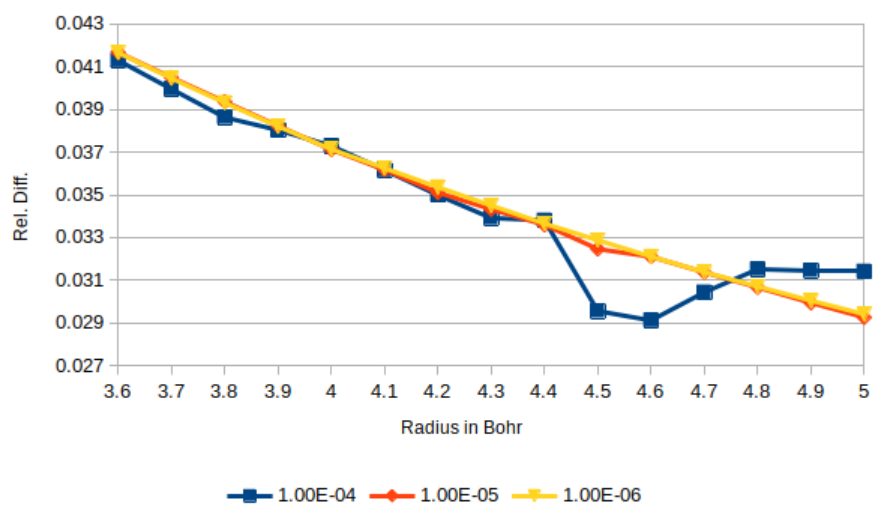
(b) All precision values plotted, except for precision value  $1e - 03$ 

Figure 6.7: Relative difference between the reaction field energy of  $\text{Li}^+$  in a water solution calculated with different relative precisions in MRCHEM and same calculations in Gaussian with daug-cc-pV5Z

### 6.2.3 Comparison Tests

The substrates studied in these tests are the same 4 substrates studied by Chipman in [30], namely,  $\text{H}_2\text{O}$ ,  $\text{NO}^+$ ,  $\text{CN}^-$  and  $\text{CH}_3\text{CONH}_2$ . Two sets of comparison tests were performed. Firstly, spherical cavity calculations where for each calculation the radius of the cavity was varied. Secondly, molecular-shaped cavities calculations were performed on all the substrates. Of the second type of test only two sets of radii were calculated, for each substrate, cavities based on the Bondi radii multiplied by 1.2, and the same cavities but their radii were increased by 0.2 Bohr. This is done to compensate for the thickness of the cavity surface.

The results for the spherical cavity tests for  $\text{H}_2\text{O}$  can be seen in Figures 6.1 and 6.3, and the results for the molecular-shaped tests for  $\text{H}_2\text{O}$  can be seen on Table 6.7. For  $\text{NO}^+$  the plots for the single sphere cavity tests can be seen in Figures 6.8 and 6.10 and the molecular shape cavity test result can be seen in Table 6.8. For  $\text{CN}^+$  one can see the plots for the single sphere cavity on Figures 6.9 and 6.11 while the molecular-shaped results are on Table 6.9. The molecular-shaped test for the incremented radii did not converge for  $\text{CN}^-$ , but comparisons between the standard scaled Bondi radii and the single sphere cavity can still be done.

Some of the data points for  $\text{CN}^-$  and  $\text{NO}^+$  are missing. The reason for this is that the calculations for these values either never completed or gave extreme outliers, due to yet not understood numerical instability. These outliers were removed from the plots in order to better visualize the trend correctly converged values. All of the available values, those which completed, can be seen in their corresponding tables in Appendix A.

There are no single sphere cavity tests for  $\text{CH}_3\text{CONH}_2$  due to the size of the molecule making single sphere calculations extremely slow for both Gaussian and MRChem. The only tests that were ran were molecular-shaped tests. Gaussian did not converge after 72 hours of running with `daug-cc-pV5Z`, therefore, the comparison values are missing from the tables. The  $\text{CH}_3\text{CONH}_2$  results are presented in Table 6.10.

The molecular-shaped cavity results shown are just the relative difference between MRChem and Gaussian values as shown in Equation 6.4. For the rest of the tables see Appendix A.

basis	Van der Waals	Van der Waals + 0.2 Bohr
cc-pVDZ	-0.15090654	0.04037456
cc-pVTZ	-0.12829535	0.06807953
cc-pVQZ	-0.12895265	0.06727416
cc-pV5Z	-0.12925406	0.06690484
aug-cc-pVDZ	-0.12913032	0.06705646
aug-cc-pVTZ	-0.13428776	0.06073717
aug-cc-pVQZ	-0.13683848	0.05761183
aug-cc-pV5Z	-0.13631495	0.05825329
daug-cc-pVDZ	-0.12816349	0.06824109
daug-cc-pVTZ	-0.13378744	0.06135020
daug-cc-pVQZ	-0.13648975	0.05803913
daug-cc-pV5Z	-0.13623509	0.05835115

Table 6.7: Relative difference between Gaussian and MRChem results from molecular-shaped cavity tests for  $\text{H}_2\text{O}$

Basis	Van der Waals radii	Van der Waals radii +0.2 Bohr
cc-pVDZ	-0.03598423	0.02044325
cc-pVTZ	-0.03692221	0.01945037
cc-pVQZ	-0.03747002	0.01887050
cc-pV5Z	-0.03810456	0.01819881
aug-cc-pVDZ	-0.03906862	0.01717832
aug-cc-pVTZ	-0.03801963	0.01828871
aug-cc-pVQZ	-0.03792710	0.01838665
aug-cc-pV5Z	-0.03814585	0.01815510
daug-cc-pVDZ	-0.03897379	0.01727870
daug-cc-pVTZ	-0.03811073	0.01819228
daug-cc-pVQZ	-0.03799786	0.01831176
daug-cc-pV5Z	-0.03813936	0.01816197

Table 6.8: Relative difference between Gaussian and MRCHEM results from molecular-shaped cavity test for  $\text{NO}^+$

Basis	Van der Waals radii
cc-pVDZ	0.01805797
cc-pVTZ	0.00402722
cc-pVQZ	-0.00689520
cc-pV5Z	-0.01760704
aug-cc-pVDZ	-0.02534307
aug-cc-pVTZ	-0.02484616
aug-cc-pVQZ	-0.02473155
aug-cc-pV5Z	-0.02453156
daug-cc-pVDZ	-0.02428967
daug-cc-pVTZ	-0.02475331
daug-cc-pVQZ	-0.02472359
daug-cc-pV5Z	-0.02449823

Table 6.9: Relative difference between Gaussian and MRCHEM results from molecular-shaped cavity test for  $\text{CN}^-$

basis	vdw	Vdw+0.2
cc-pVDZ	-0.18617733	-0.02575734
cc-pVTZ	-0.13954658	0.03006522
cc-pVQZ	-0.12431320	0.04830139
cc-pV5Z	-0.12131273	0.05189330
aug-cc-pVDZ	-0.11396644	0.06068769
aug-cc-pVTZ	-0.12038877	0.05299940
aug-cc-pVQZ	-0.12258540	0.05036977
aug-cc-pV5Z	-0.12243503	0.05054978
daug-cc-pVDZ	-0.11719827	0.05681881
daug-cc-pVTZ	-0.12128833	0.05192252
daug-cc-pVQZ	-0.12247807	0.05049826

Table 6.10: Relative difference between Gaussian and MRCHEM results from molecular-shaped cavity test for  $\text{CH}_3\text{CONH}_2$

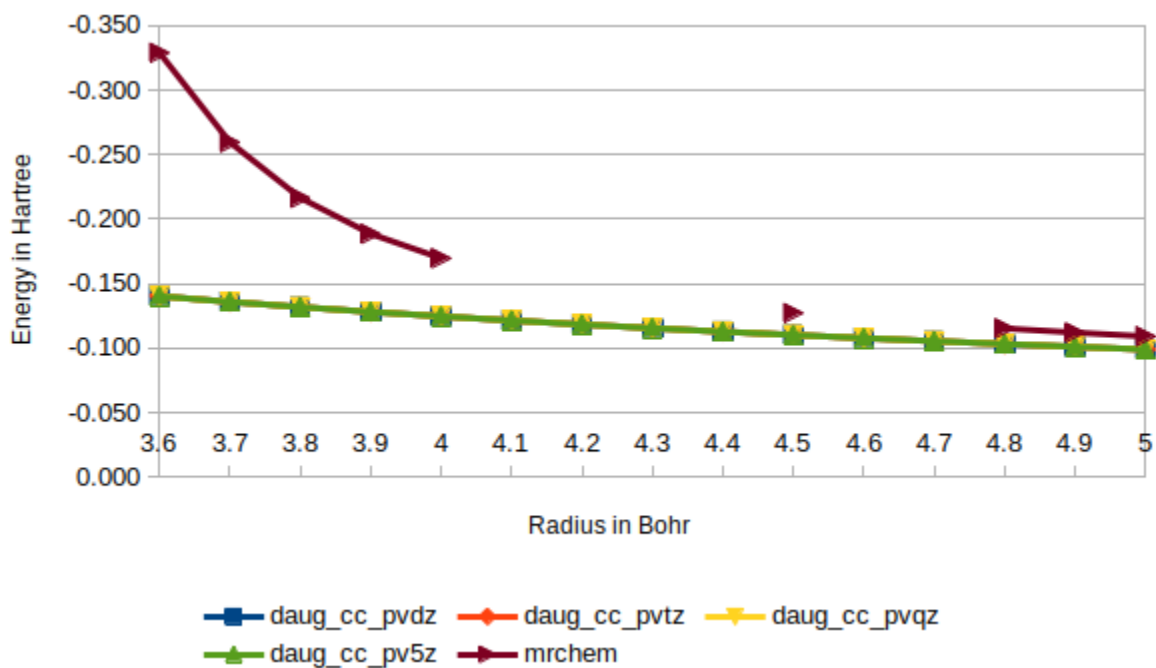


Figure 6.8: Reaction field energy of  $\text{NO}^+$  in a water solution, calculated with MRCHEM and with different double augmented basis sets in Gaussian

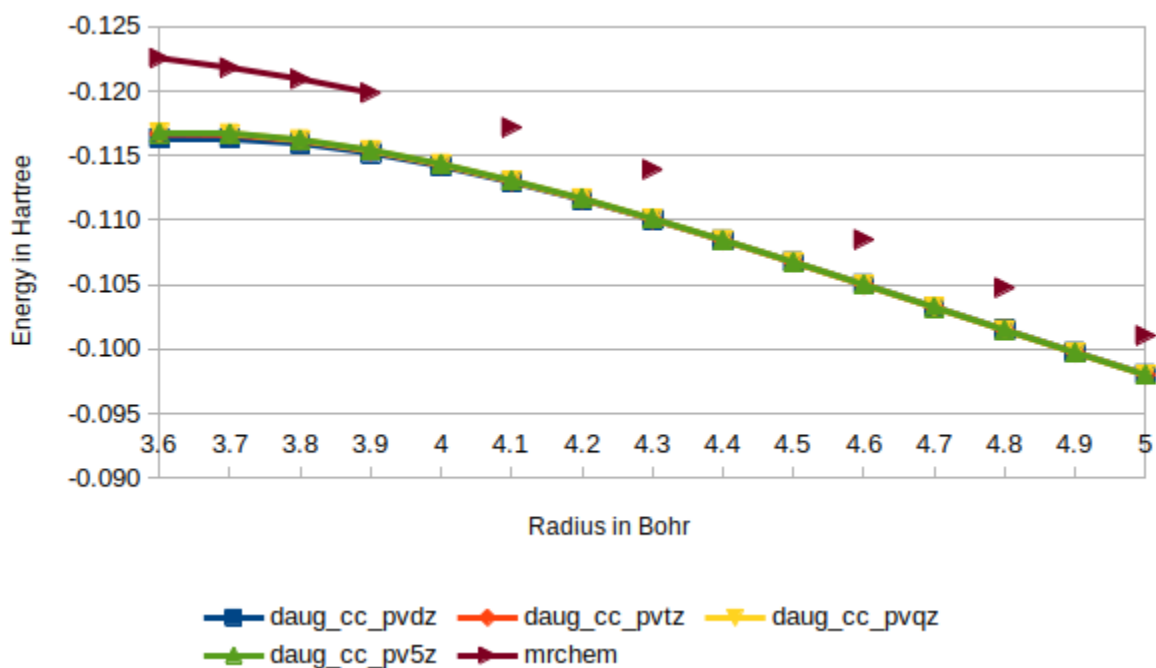


Figure 6.9: Reaction field energy of  $\text{CN}^-$  in a water solution, calculated with MRCHEM and with different basis sets in Gaussian



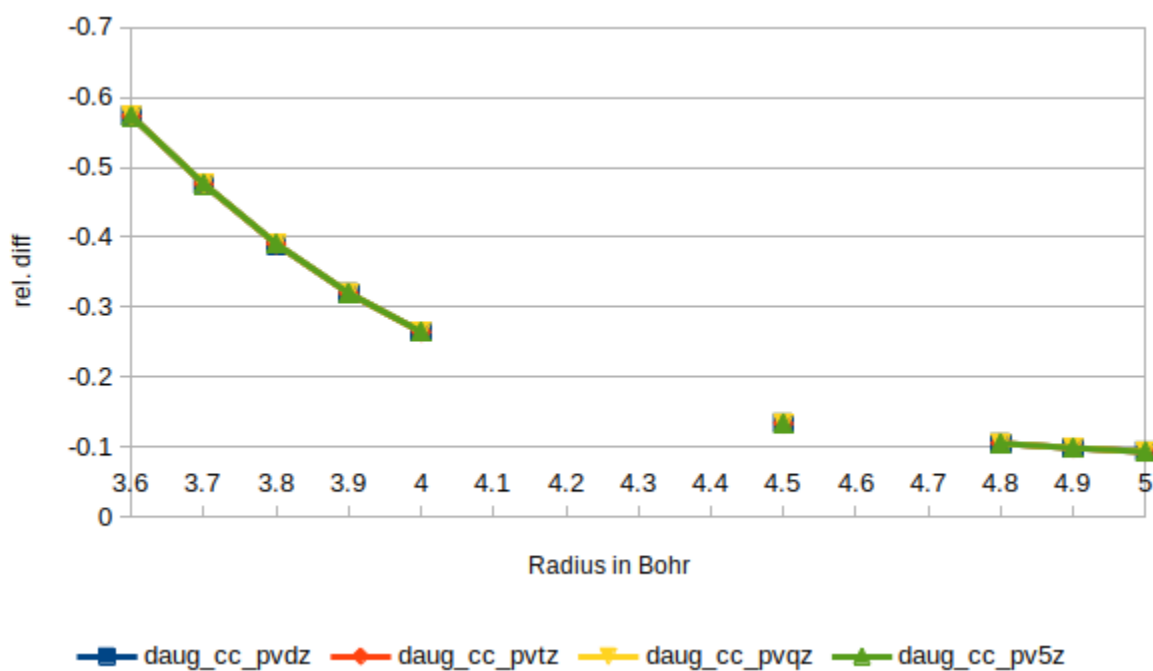


Figure 6.10: Relative difference between the reaction field energy of  $\text{NO}^+$  in a water solution calculated with MRCHEM and with different double augmented basis sets in Gaussian

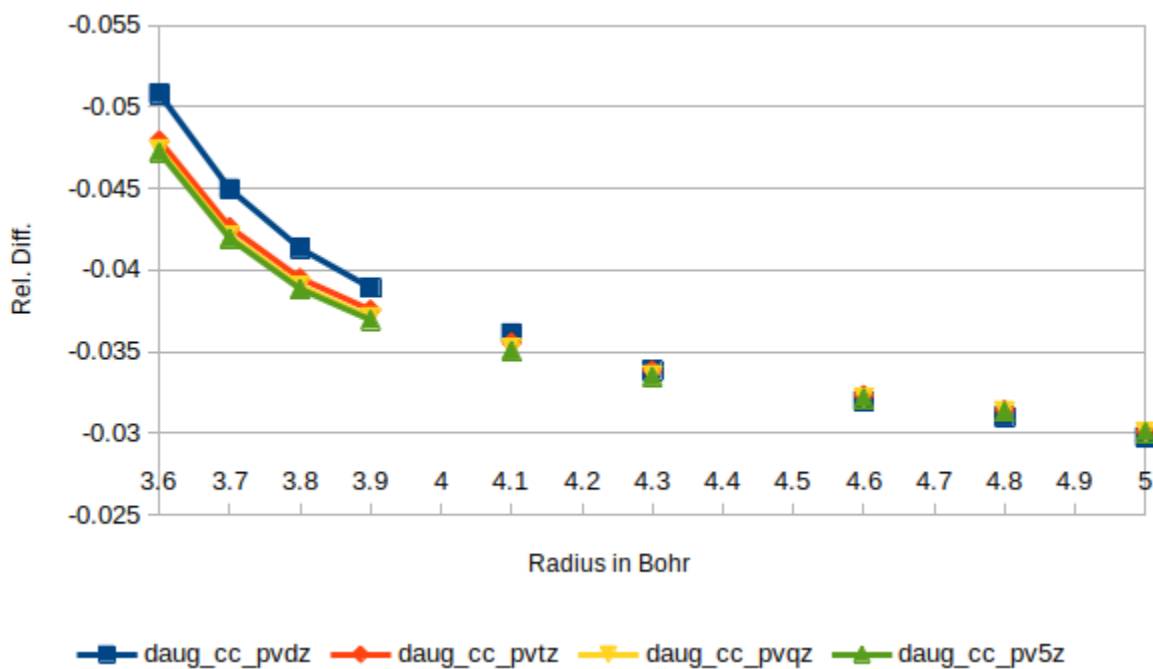


Figure 6.11: Relative difference between the reaction field energy of  $\text{CN}^-$  in a water solution calculated with MRCHEM and with different double augmented basis sets in Gaussian

### 6.2.4 Variational implementation tests

Figures 6.12 and 6.13 show the reaction field energy calculated with the variational implementation for  $\text{H}_2\text{O}$  and  $\text{Li}^+$ , respectively. Figures 6.14 and 6.15 show the relative difference as calculated with Equation 6.4 for  $\text{H}_2\text{O}$  and  $\text{Li}^+$ , respectively.

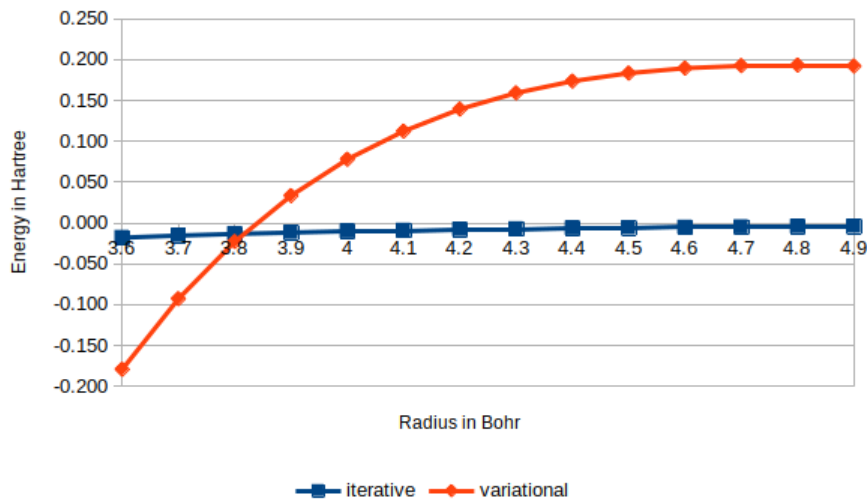


Figure 6.12: Reaction field energy for  $\text{H}_2\text{O}$  in water using the variational and iterative implementation

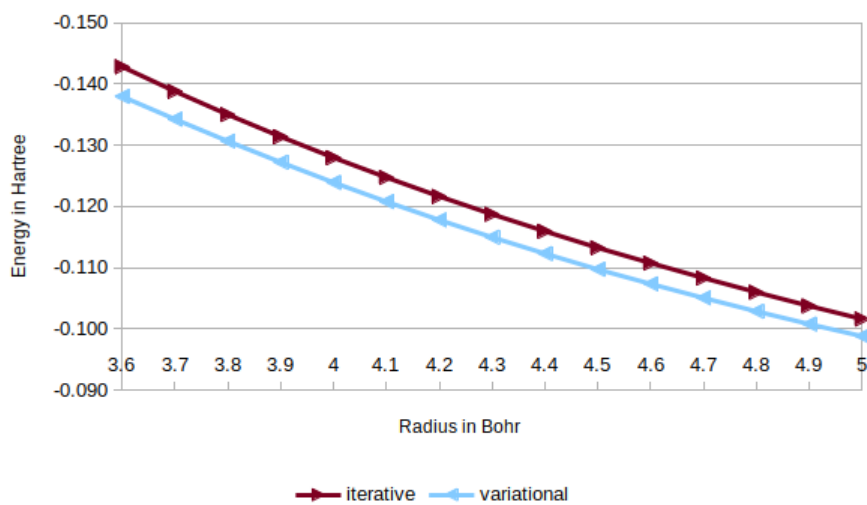


Figure 6.13: Reaction field energy for  $\text{Li}^+$  in water using the variational and iterative implementation

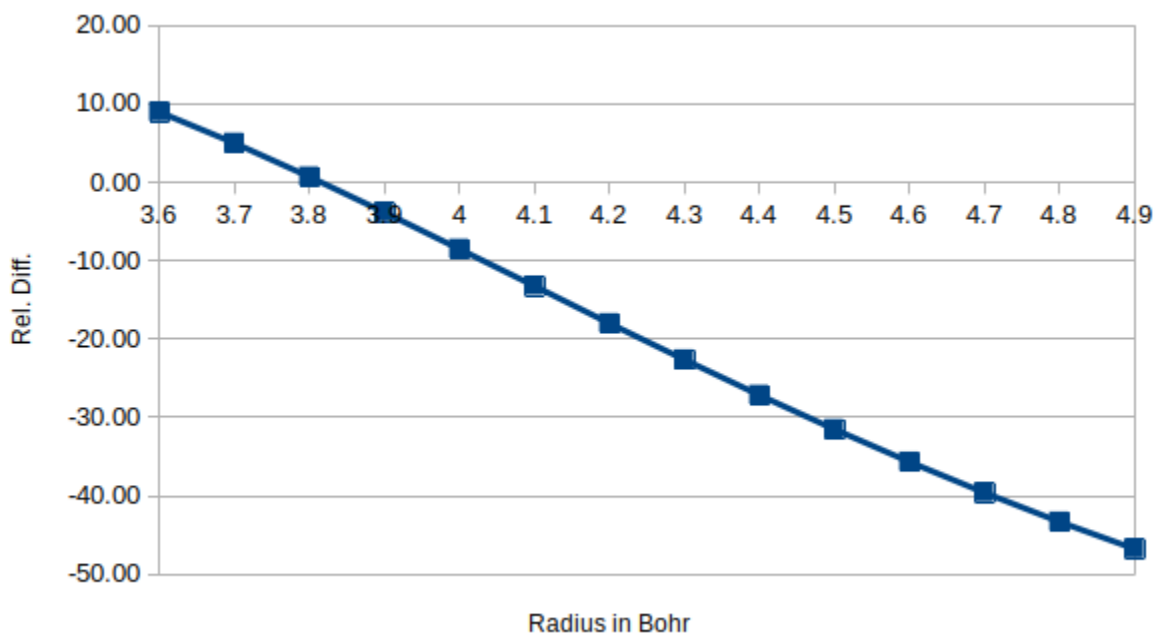


Figure 6.14: Relative difference between the reaction field energy of  $\text{H}_2\text{O}$  calculated with the variational implementation against the iterative implementation

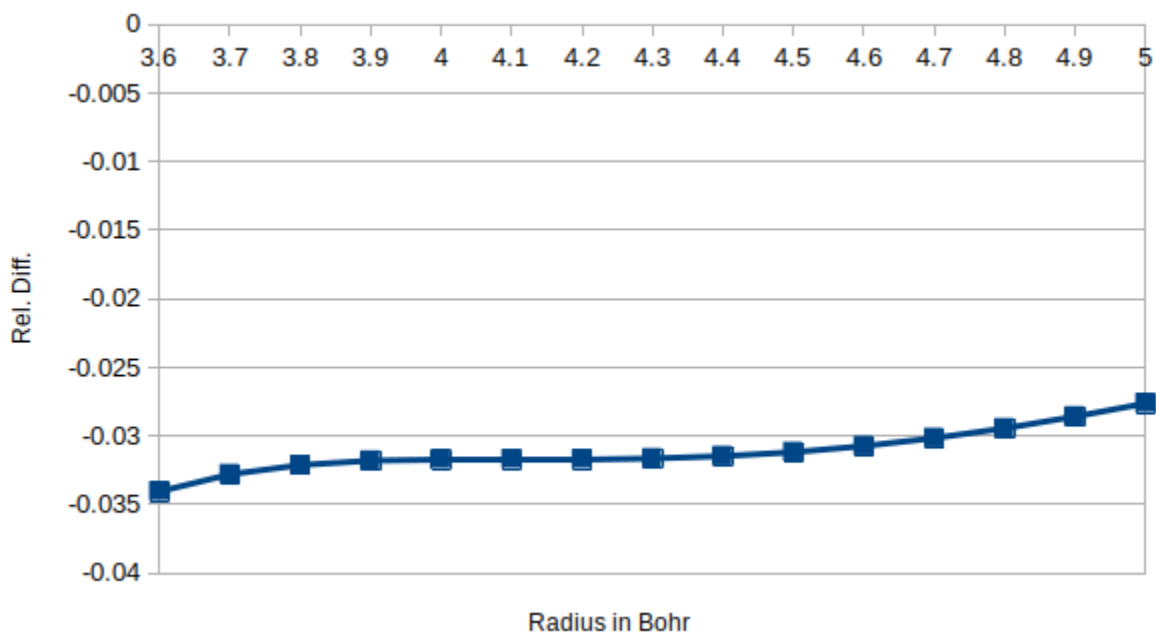


Figure 6.15: Relative difference between the reaction field energy of  $\text{Li}^+$  calculated with the variational implementation against the iterative implementation

## 6.3 Discussion

### 6.3.1 Theoretical correctness

The results for the integral of the surface charge distribution  $\gamma_s$  for both dielectric constants of 2 and 80 are on Tables 6.1 and 6.2 respectively. These results must coincide with exact value calculated with Equation 6.2 if the implementation is theoretically correct. We can see that, since the relative difference is so small, that the implementation is correct for both big and small dielectric constants. The values for  $\epsilon_{out} = 80$  have a bit larger relative difference in comparison, which stems from the fact that the implementation has hardships in solving solvation systems with big dielectric constants. Increasing the precision of the calculations decreases the relative difference, as expected.

Increasing the radius does not improve the differences of the integrals, except for  $\epsilon_{out} = 2$  with  $\sigma = 0.1$  and  $prec. = 1e-4$ , and for  $\epsilon_{out} = 80$  with  $\sigma = 0.2$  and  $prec. = 1e-4$  where it improves by 0.1% for  $\epsilon_{out} = 2$  and 0.03% for  $\epsilon_{out} = 80$ . The cause for this decrease in the quality of the MRChem results might be because of the surface charge effect being diminished by the bigger cavity. The reason it gets better at only two sets of parameters might be caused by numerical noise, given the size of the variation. The same behavior is seen for tighter surfaces. The difference worsens when increasing tightness, and where it gets better is most likely because of numerical noise, given the size of the variation. These two observations show the difficulty this implementation still has at working with sharp transitions and larger surface areas.

The energies, on the other hand, do not have the constraint of needing to be exactly the same as the Born model values. This is simply because the Born model is a model in which the cavity surface is a sharp transition. We can see that this is the case since the relative difference increases or decreases by very small values when increasing the relative precision of the calculations, telling us that the variation of our values between themselves is much smaller than the difference with the Born model. It was expected as well, that when the width of our cavity surface becomes small compared to the radius our results would resemble the Born results more. Two ways of decreasing the width of the surface relative to the size of the cavity exist, either by increasing the radius and/or by decreasing the width of the transition. Both of these relations hold true, in our results, for both dielectric constants.

The relative differences for the  $\epsilon_{out} = 80$  are not as good as for  $\epsilon_{out} = 2$ . The most likely cause is the transition becomes steeper relative to the width and radius parameters due to the high difference between  $\epsilon_{out}$  and  $\epsilon_{in}$ . This leads to MRChem having difficulties projecting the cavity, which in turn, increase the numerical noise in the calculation.

### 6.3.2 Parametrization

The values for H<sub>2</sub>O reaction energy with a cavity radius of 5 Bohr diverged, therefore we removed them in order to better visualize the trends. We can see in Figures 6.3 and 6.4 that the relative difference decays, diminishes to a stable value, the bigger the cavity is. The method Gaussian uses to calculate the reaction field describes the transition from inside the cavity to the outside as happening at a boundary, this being the surface of the cavity. The problem is solved at the surface of the cavity, which is assumed to be two dimensional, so the transition is noncontinuous, as explained in Chapter 4. Our cavity is defined as an analytical transition with a parameter  $\sigma$  which controls the width of the

cavity surface, so that we get a smooth transition between the inside and the outside of the cavity.

Two main factors are responsible for the decay in relative difference that we observe. Firstly, the bigger the radius, the smaller the difference is relative to the size of the cavity. This means that at larger distances our cavity resembles more and more that of a discontinuous transition such as the ones used by Gaussian. The second factor is the amount of the charge density that is contained within the cavity. The effect of this can be seen on the tests that followed.

As we can see on the Figures 6.5 and 6.6 there is a significant improvement on the relative difference when we compare with bigger radii of MRCHEM calculations to smaller radii of Gaussian calculations. This is caused by the smooth cavity. Since the transition is wider in our implementation there is more density that is situated outside the cavity than in cavities of same radius from Gaussian calculations. This was accounted for when we increased the radii, and we still see the same decay in difference that we saw in the standard comparison.

The graphs from Figure 6.7 tell us two things about our results: Firstly at precision lower than  $1e - 03$  we get results that are at least 20% different than the best Gaussian results we could run for small radii and diverge from the Gaussian results for bigger radii. Secondly we see that we don't need a relatively high precision to get stable results which are consistent with greater previsions and that also approach the Gaussian results at bigger radii.

On the other hand, it is hard to decide if this is applicable to bigger systems, as the Lithium cation is fairly simple, whereas other systems might not be so simple.

### 6.3.3 Comparison

Same as with the tests for  $\text{Li}^+$  and  $\text{H}_2\text{O}$ , the Figures 6.10 and 6.11 show that both relative differences for  $\text{CN}^-$  and  $\text{NO}^+$  decay at higher radii.

The relative differences for the results for  $\text{NO}^+$  seem to decay faster than the other molecules, but it is hard to see due to the lack of data points. Assuming that it decays faster, one can explain this as being due to the fact that the electron density is closer to the atoms, making it easier for the cavity to contain most of it. The opposite can be seen for  $\text{CN}^-$ . The explanation for this might go through the same line of thought as that for  $\text{NO}^+$ , but now since the molecule is negatively charged, the density is more diffuse, making it harder to contain it in its entirety.

The divergence around the interval (4.0, 4.7) can be attributed to the way the functions are projected. The cavity function is very sharp at the transition. In order to project it correctly one needs to go to very low scales. Additionally, the intervals are powers of two, meaning that there is always the discontinuity from the wavelets at the 4.0 point, which is hard to correct. This discontinuity brings forth numerical noise that gets amplified when the derivative of the function is calculated to solve the GPE. These errors occur in this implementation as it is still in development. These problems are expected to be diminished or removed in future revisions. One way we could attempt to fix is by defining a better derivative for the cavity. Fosso-Tande defined the derivative of the cavity as combinations of analytical derivatives [1]. This definition supposedly would help remove numerical noise at the transition, since one can create these analytical derivatives before projecting them into the MW basis.

The tables for the molecular-shaped cavity tests show us that for most the molecules,

the relative difference doesn't vary too much when going to molecular-shaped cavity or that it gets much better, as is the case for  $\text{NO}^+$  in Table 6.8. It can be seen that, while its spherical cavity plot, Figure 6.10, does not go lower than a relative difference of 10%, its molecular-shaped cavity tests have a relative difference of less than 4%. The same can be said for the results for  $\text{CN}^-$ , in Table 6.9, which got to less than 3% from the Gaussian results, while it never approached 10% with spherical cavity, Figure 6.11.

The  $\text{H}_2\text{O}$  results, in Table 6.7 do not go too far from the best relative difference shown in Figure 6.3. They do significantly better when increasing the radius of the interlocking spheres, a decrease in the relative difference of around 6 – 9%. This decrease is seen in the other molecules as well, where, for  $\text{NO}^+$ , the decrease is around 1 – 2%.

$\text{CH}_3\text{CONH}_2$ , in Table 6.10 has a difference of at best 11.4% and at worst 18.6%. Increasing the radii of the interlocking spheres has the same effect that was observed for  $\text{H}_2\text{O}$ , but stronger. Here they decrease by 5 – 16%. This tells us that in MRChem, in order to get comparable results to Gaussian, one needs to define a cavity that is a bit bigger than the one used in Gaussian. This makes sense as the cavity surface, because of the width, starts earlier for us than it does for Gaussian. This leads to more of the density escaping. Increasing the radius gives us a cavity that is effectively the same as Gaussian's.

### 6.3.4 Variational implementation

The results for the variational implementation of the GPE for  $\text{H}_2\text{O}$  and  $\text{Li}^+$  is shown in Figures 6.14 and 6.15 respectively.

Ideally, the results from the iterative and variational implementation should be almost equal, with differences between them being for the most part caused by numerical noise. This is because we are using the same GPE, but different implementation, for both of them.

$\text{Li}^+$  behaves almost as expected, with very small differences between implementations, which can be explained as numerical noise.  $\text{H}_2\text{O}$  on the other hand shows signs that, for bigger systems, the errors are not numerical noise only. The  $\text{H}_2\text{O}$  differences imply that there is an error in the implementation, which gets augmented for bigger systems. This is further strengthened by the fact that the variational values for the other molecules had the same trend, as can be seen in the Tables of Appendix A.

Something worth noting is that the values appear to behave systematically, which strengthens the possibility of something being implemented wrongly, and most importantly, that it can be accounted for and corrected in future revisions of this implementation.

## 6.4 Concluding remarks

The theoretical correctness tests showed that the implementation is, at its base, theoretically correct.

We saw that when increasing the radii of the cavity in calculations, the difference between the Gaussian calculations and the MRChem calculations decayed, as is expected. Having a tighter precision than  $1e - 4$  helps to have better results, but is not entirely necessary, as the difference between the models is larger than the improvement upon moving to better precision values.

We see that all the solutes used in [30] have relative differences that decay with bigger radii. We also saw that using bigger MRChem cavities where Gaussian used smaller gave us better relative differences in molecular-shaped Cavities. The MRChem calculations did not converge for some values of  $\text{CN}^-$  and  $\text{NO}^+$  which is most likely caused by instabilities in the derivatives of the cavity, which can be improved by following Fosso–Tande [1].

The variational implementation gives acceptable results for small systems such as  $\text{Li}^+$  but for bigger systems, it shows clear signs of errors in the implementation. The variational implementation is still in its early days when it comes to development, and the results still behave systematically, which tells us that they can be accounted for and improved upon. We have also seen that for most of our comparisons we could not expect our values to actually converge to what we were testing against. This is because there still are not many equivalent implementations to test against.

## 6.5 Areas of improvement/future development

Given that the iterative values gave results as expected we can say that the implementation is correct. An improvement would be to try to change the cavity definition so as to take into account more of the electron density. One way that is possible right now is to decrease the width of the transition, another is to simply use bigger cavities as these are shown to give better results. Both of those are possible with the implementation used now, but decreasing the width of the transition might make the cavity harder to project.

A better solution to this is to implement the derivative of the cavity as a combination of analytical derivatives, as Fosso–Tande did in [1], which might let us get better results with the same parameters used in the tests of this chapter.

The goal in the future is to apply these solutions and test if they better the results of the variational method. After that we will start seeing how molecular properties are affected by this.

Another goal is to attempt better stability at sharper cavity surfaces as there is clearly a trend where the narrower the surface, the harder it is to actually converge it.





# Bibliography

- [1] Jacob Fosso-Tande and Robert J Harrison. Implicit Solvation Models in a Multiresolution Multiwavelet Basis. *Chem Phys Lett*, pages 1–16, February 2013.
- [2] Jacopo Tomasi, Benedetta Mennucci, and Roberto Cammi. Quantum mechanical continuum solvation models. *Chem Rev*, 105(8):2999–3093, August 2005.
- [3] Filippo Lipparini, Giovanni Scalmani, Benedetta Mennucci, Eric Cancès, Marco Caricato, and Michael J Frisch. A variational formulation of the polarizable continuum model. *J Chem Phys*, 133(1):014106, July 2010.
- [4] Jacopo Tomasi and Maurizio Persico. Molecular Interactions in Solution: An Overview of Methods Based on Continuous Distributions of the Solvent. *Chem Rev*, 94(7):2027–2094, November 1994.
- [5] Rune Sørland Monstad. Solvent effects with multiwavelets. Master’s thesis, UiT, The arctic university of norway, 11 2017.
- [6] Peter Atkins and Ronald Friedman. *Molecular Quantum Mechanics*. Oxford University Press, 5 edition, 2011.
- [7] Claude Cohen-Tannoudji, Bernard Diu, and Franck Laloë. *Quantum Mechanincs*, volume one. Wiley-Interscience, 1973.
- [8] Peter Atkins and Julio de Paula. *Physical Chemistry*. Oxford, 10 edition, 2014.
- [9] Cristopher J. Cramer. *Essentials of to Computational Chemistry: Theories and models*. Wiley, 2 edition, 2004.
- [10] Frank Jensen. *Introduction to Computational Chemistry*. Wiley, 3 edition, 2017.
- [11] Jack Simons. *Advanced Theoretical Chemistry*. 2016. [Online; accessed 18.02.2019].
- [12] proton-electron mass ratio, 2019.
- [13] Frank Jensen. *Introduction to Computational Chemistry*. Wiley, 1 edition, 1999.
- [14] Trygve Helgaker, Poul Jorgensen, and Jeppe Olsen. *Molecular Electronic-Structure Theory*. Wiley, 2012.
- [15] P. Hohenberg and W. Kohn. Inhomogeneous electron gas. *Phys. Rev.*, 136:B864–B871, Nov 1964.
- [16] Radovan Bast and Per-Olof Widmark, editors. *European Summerschool in Quantum chemistry 2013*, volume 1. Stabilimento Tipolitografico PRIULLA s.r.l., Via Ugo La Malfa, 64, I-90146 Palermo Italy, 5 2013.

- [17] R. Schneider and F. Krüger. Introduction to multiresolution analysis (mra). TUB - Technical University of Berlin, Jan. 22 2007.
- [18] Gregory Beylkin. Lecture notes on mra/madness.
- [19] Bradley K. Alpert. A class of bases in  $\mathbb{R}^2$  for the sparse representation of integral operators. *SIAM Journal on Mathematical Analysis*, 24(1):246–262, January 1993.
- [20] Stig Rune Jensen. *Real-space all-electron Density Functional Theory with Multi-wavelets*. PhD thesis, UiT, The arctic university of norway, 2 2014.
- [21] Luca Frediani, Eirik Fossgaard, Tor Flå, and Kenneth Ruud. Fully adaptive algorithms for multivariate integral equations using the non-standard form and multi-wavelets with applications to the poisson and bound-state helmholtz kernels in three dimensions. *Molecular Physics*, 111(9-11):1143–1160, 2013.
- [22] Gregory Beylkin, D J Gines, and Lev Vozovoi. Adaptive solution of partial differential equations in multiwavelet bases. 1999.
- [23] Benedetta Mennucci. Modelling environment effects, September 2018.
- [24] A. Bondi. van der waals volumes and radii. *The Journal of Physical Chemistry*, 68(3):441–451, 1964.
- [25] Filippo Lipparini. *Molecular properties in complex environments: towards a polarizable multiscale approach*. PhD thesis, Scuola Normale Superiore Classe di Scienze Corso di Perfezionamento in Chimica, 2013.
- [26] Kenichi Konoshi and Giampiero Paffuyi. *Quantum Mechanics; A New Introduction*. Oxford University press, 2009.
- [27] Vampyr, 2019.
- [28] Mrcpp, 2019.
- [29] Mrchem, 2019.
- [30] Daniel M. Chipman. Comparison of solvent reaction field representations. *Theoretical Chemistry Accounts*, 107(2):80–89, Feb 2002.
- [31] Thom H. Dunning. Gaussian basis sets for use in correlated molecular calculations. i. the atoms boron through neon and hydrogen. *The Journal of Chemical Physics*, 90(2):1007–1023, 1989.
- [32] M. J. Frisch, G. W. Trucks, H. B. Schlegel, G. E. Scuseria, M. A. Robb, J. R. Cheeseman, G. Scalmani, V. Barone, B. Mennucci, G. A. Petersson, H. Nakatsuji, M. Caricato, X. Li, H. P. Hratchian, A. F. Izmaylov, J. Bloino, G. Zheng, J. L. Sonnenberg, M. Hada, M. Ehara, K. Toyota, R. Fukuda, J. Hasegawa, M. Ishida, T. Nakajima, Y. Honda, O. Kitao, H. Nakai, T. Vreven, J. A. Montgomery, Jr., J. E. Peralta, F. Ogliaro, M. Bearpark, J. J. Heyd, E. Brothers, K. N. Kudin, V. N. Staroverov, R. Kobayashi, J. Normand, K. Raghavachari, A. Rendell, J. C. Burant, S. S. Iyengar, J. Tomasi, M. Cossi, N. Rega, J. M. Millam, M. Klene, J. E. Knox, J. B. Cross, V. Bakken, C. Adamo, J. Jaramillo, R. Gomperts, R. E. Stratmann, O. Yazyev, A. J.

Austin, R. Cammi, C. Pomelli, J. W. Ochterski, R. L. Martin, K. Morokuma, V. G. Zakrzewski, G. A. Voth, P. Salvador, J. J. Dannenberg, S. Dapprich, A. D. Daniels, Ö. Farkas, J. B. Foresman, J. V. Ortiz, J. Cioslowski, and D. J. Fox. Gaussian 09 Revision E.01. Gaussian Inc. Wallingford CT 2009.



# Appendix A

## Data tables

Here are all the Data tables for all tests performed



Table A.4: Total energy of  $\text{Li}^+$ . Radius on top row in Bohr and energies in Hartree

Basis	3.6	3.7	3.8	3.9	4	4.1	4.2	4.3	4.4	4.5	4.6	4.7	4.8	4.9	5
cc-pVDZ	-7.23611864	-7.37323448	-7.36601770	-7.36268690	-7.35952284	-7.35651275	-7.35364019	-7.35091297	-7.34830399	-7.34581096	-7.34342634	-7.34114918	-7.33895516	-7.33685645	-7.33484469
cc-pVTZ	-7.23638007	-7.37349549	-7.36627880	-7.36294804	-7.35978832	-7.35677396	-7.35390743	-7.35117423	-7.34856526	-7.34607225	-7.34368763	-7.34140449	-7.33921648	-7.33711778	-7.33510302
cc-pVQZ	-7.23638436	-7.37344973	-7.36628304	-7.36295229	-7.35978807	-7.35677821	-7.35391168	-7.35117848	-7.34856952	-7.34607652	-7.34369190	-7.34140876	-7.33922075	-7.33712205	-7.33510729
cc-pV5Z	-7.23641070	-7.37352601	-7.36630935	-7.36297860	-7.35981439	-7.35680453	-7.35393801	-7.35120481	-7.34859585	-7.34610285	-7.34371823	-7.34143509	-7.33924709	-7.33714838	-7.33513363
aug-cc-pVDZ	-7.23612105	-7.37323683	-7.36602006	-7.36268927	-7.35952502	-7.35651513	-7.35364858	-7.35091536	-7.34830638	-7.34581336	-7.34342873	-7.34114558	-7.33895756	-7.33685885	-7.33484409
aug-cc-pVTZ	-7.23638039	-7.37349579	-7.36627911	-7.36294835	-7.35978817	-7.35677427	-7.35390774	-7.35117454	-7.34856557	-7.34607257	-7.34368795	-7.34140481	-7.33921680	-7.33711809	-7.33510334
aug-cc-pVQZ	-7.23638446	-7.37344982	-7.36628314	-7.36295239	-7.35978817	-7.35677831	-7.35391178	-7.35117859	-7.34856962	-7.34607662	-7.34369200	-7.34140886	-7.33922085	-7.33712215	-7.33510740
aug-cc-pV5Z	-7.23641072	-7.37352602	-7.36630936	-7.36297861	-7.35981440	-7.35680455	-7.35393802	-7.35120482	-7.34859587	-7.34610286	-7.34371825	-7.34143511	-7.33924710	-7.33714840	-7.33513364
daug-cc-pVDZ	-7.23612173	-7.37323750	-7.36602074	-7.36268994	-7.35952570	-7.35651581	-7.35364926	-7.35091604	-7.34830706	-7.34581404	-7.34342942	-7.34114627	-7.33895825	-7.33685954	-7.33484478
daug-cc-pVTZ	-7.23638047	-7.37349587	-7.36627919	-7.36294843	-7.35978422	-7.35677435	-7.35390782	-7.35117462	-7.34856566	-7.34607265	-7.34368803	-7.34140489	-7.33921688	-7.33711818	-7.33510342
daug-cc-pVQZ	-7.23638449	-7.37344985	-7.36628317	-7.36295241	-7.35979398	-7.35677834	-7.35391181	-7.35117462	-7.34856965	-7.34607665	-7.34369203	-7.34140889	-7.33922088	-7.33712218	-7.33510742
daug-cc-pV5Z	-7.23641072	-7.37352603	-7.36630936	-7.36297861	-7.35981440	-7.35680455	-7.35393803	-7.35120483	-7.34859587	-7.34610286	-7.34371825	-7.34143511	-7.33924710	-7.33714840	-7.33513365
mrcm 1e - 6	-7.23641516	-7.37924155	-7.37141997	-7.36781859	-7.36440059	-7.36111705	-7.35800820	-7.35516961	-7.35237616	-7.34971364	-7.34716832	-7.34473542	-7.34240937	-7.34017943	-7.33804181
mrcm 1e - 5	-7.23641194	-7.37924017	-7.37142201	-7.36781826	-7.36439551	-7.36116017	-7.35806498	-7.35514597	-7.35236608	-7.34966534	-7.34716447	-7.34473317	-7.34240177	-7.34016617	-7.33802382
mrcm 1e - 4	-7.23638816	-7.37916498	-7.37130396	-7.36776934	-7.36439379	-7.36113481	-7.35802716	-7.35507529	-7.35236608	-7.34932259	-7.34682049	-7.34440964	-7.34246577	-7.34029489	-7.33821243
mrcm 1e - 3	-7.23275328	-7.40020255	-7.38922393	-7.38512749	-7.38197984	-7.37970579	-7.37822277	-7.37739254	-7.37702563	-7.37686741	-7.37648843	-7.37596264	-7.37510586	-7.37390906	-7.37290366
variational 1e - 5	-7.23641194	-7.37437711	-7.37067004	-7.36708660	-7.36333777	-7.359720628	-7.356240852	-7.35338948	-7.34981709	-7.34613375	-7.34376021	-7.34146506	-7.33928143	-7.33720038	-7.33521667

Table A.5: Reaction field energy of  $\text{Li}^+$ . Radius on top row in Bohr and energies in Hartree

Basis	3.6	3.7	3.8	3.9	4	4.1	4.2	4.3	4.4	4.5	4.6	4.7	4.8	4.9	5
cc-pVDZ	-0.13711584	-0.13340992	-0.12989906	-0.12656825	-0.12340400	-0.12039411	-0.11732755	-0.11479433	-0.11218535	-0.10969232	-0.10730769	-0.10502454	-0.10283652	-0.10073781	-0.09872304
cc-pVTZ	-0.13711542	-0.13340955	-0.12989873	-0.12656797	-0.12340375	-0.12039389	-0.11732736	-0.11479415	-0.11218519	-0.10969218	-0.10730756	-0.10502442	-0.10283641	-0.10073770	-0.09872295
cc-pVQZ	-0.13711537	-0.13340950	-0.12989869	-0.12656793	-0.12340371	-0.12039386	-0.11732733	-0.11479413	-0.11218517	-0.10969216	-0.10730754	-0.10502440	-0.10283639	-0.10073769	-0.09872294
cc-pV5Z	-0.13711531	-0.13340945	-0.12989865	-0.12656789	-0.12340369	-0.12039383	-0.11732731	-0.11479411	-0.11218515	-0.10969215	-0.10730753	-0.10502439	-0.10283638	-0.10073768	-0.09872293
aug-cc-pVDZ	-0.13711579	-0.13340987	-0.12989902	-0.12656822	-0.12340398	-0.12039409	-0.11732754	-0.11479432	-0.11218534	-0.10969232	-0.10730769	-0.10502454	-0.10283652	-0.10073781	-0.09872305
aug-cc-pVTZ	-0.13711540	-0.13340953	-0.12989872	-0.12656796	-0.12340374	-0.12039388	-0.11732735	-0.11479415	-0.11218518	-0.10969218	-0.10730756	-0.10502442	-0.10283641	-0.10073770	-0.09872295
aug-cc-pVQZ	-0.13711536	-0.13340949	-0.12989868	-0.12656792	-0.12340371	-0.12039385	-0.11732732	-0.11479412	-0.11218516	-0.10969216	-0.10730754	-0.10502440	-0.10283639	-0.10073769	-0.09872294
aug-cc-pV5Z	-0.13711531	-0.13340945	-0.12989865	-0.12656789	-0.12340368	-0.12039383	-0.11732731	-0.11479411	-0.11218515	-0.10969215	-0.10730753	-0.10502439	-0.10283638	-0.10073768	-0.09872293
daug-cc-pVDZ	-0.13711577	-0.13340986	-0.12989901	-0.12656821	-0.12340397	-0.12039408	-0.11732753	-0.11479431	-0.11218533	-0.10969231	-0.10730769	-0.10502454	-0.10283652	-0.10073781	-0.09872305
daug-cc-pVTZ	-0.13711540	-0.13340953	-0.12989872	-0.12656796	-0.12340374	-0.12039388	-0.11732735	-0.11479415	-0.11218518	-0.10969217	-0.10730756	-0.10502442	-0.10283641	-0.10073770	-0.09872295
daug-cc-pVQZ	-0.13711536	-0.13340949	-0.12989868	-0.12656792	-0.12340371	-0.12039385	-0.11732732	-0.11479412	-0.11218516	-0.10969216	-0.10730754	-0.10502440	-0.10283639	-0.10073769	-0.09872294
daug-cc-pV5Z	-0.13711531	-0.13340945	-0.12989864	-0.12656789	-0.12340368	-0.12039383	-0.11732731	-0.11479411	-0.11218515	-0.10969215	-0.10730753	-0.10502439	-0.10283638	-0.10073768	-0.09872293
mrcm 1e - 6	-0.16744927	-0.16150098	-0.15647065	-0.15237421	-0.14922656	-0.14695251	-0.144546949	-0.144663926	-0.14427235	-0.14411413	-0.14399685	-0.14373515	-0.14320936	-0.14235258	-0.141115578
mrcm 1e - 5	-0.14277682	-0.13873915	-0.13491580	-0.13138118	-0.12800563	-0.12474665	-0.12163900	-0.11868713	-0.11597792	-0.11293444	-0.11043233	-0.10822148	-0.10607761	-0.103990674	-0.10182427
mrcm 1e - 4	-0.14282823	-0.13881092	-0.13501107	-0.131440632	-0.12798365	-0.124747823	-0.12165304	-0.11873404	-0.115959414	-0.11325340	-0.11075253	-0.10831923	-0.10598984	-0.10375423	-0.10161189
mrcm 1e - 3	-0.14282639	-0.13880610	-0.13500481	-0.131440342	-0.12798544	-0.12475789	-0.12168304	-0.11875445	-0.11596100	-0.11329848	-0.11075316	-0.10832026	-0.10599421	-0.10376427	-0.10162265
variational 1e - 5	-0.13796517	-0.13425810	-0.13067466	-0.12722727	-0.12392583	-0.12079434	-0.11779658	-0.11449754	-0.11230515	-0.109772181	-0.10734827	-0.10505312	-0.10286949	-0.10078845	-0.09880473





Basis	gas phase $E$	$R = vdw * 1.2$	$R + 0.2$
cc-pVDZ	-207.99616289	-208.01040179	-208.00814905
cc-pVTZ	-208.05993722	-208.07499198	-208.07263760
cc-pVQZ	-208.07568572	-208.09100701	-208.08864351
cc-pV5Z	-208.07958414	-208.09495792	-208.09259553
aug-cc-pVDZ	-208.01289874	-208.02840106	-208.02600367
aug-cc-pVTZ	-208.06363709	-208.07902704	-208.07666608
aug-cc-pVQZ	-208.07677471	-208.09212622	-208.08977064
aug-cc-pV5Z	-208.07974233	-208.09509647	-208.09273570
daug-cc-pVDZ	-208.01390429	-208.02935006	-208.02695457
daug-cc-pVTZ	-208.06394178	-208.07931599	-208.07695391
daug-cc-pVQZ	-208.07684910	-208.09220249	-208.08984495
daug-cc-pV5Z	b		
mrchem	-208.08017977	-208.09767608	-208.09479511
variational	-208.08017977	-210.77259049	-209.84193252

Table A.9: Total energies for  $\text{CH}_3\text{CONH}_2$  with molecular shaped cavity, radii in Bohr and energies in Hartree

Basis	$R = vdw * 1.2$	$R + 0.2$
cc-pVDZ	-76.03545667	-76.03391682
cc-pVTZ	-76.06602470	-76.06443065
cc-pVQZ	-76.07367749	-76.07208832
cc-pV5Z	-76.07593194	-76.07434960
aug-cc-pVDZ	-76.05031036	-76.04872816
aug-cc-pVTZ	-76.06942047	-76.06784671
aug-cc-pVQZ	-76.07476625	-76.07319603
aug-cc-pV5Z	-76.07608931	-76.07451471
daug-cc-pVDZ	-76.05079835	-76.04920787
daug-cc-pVTZ	-76.06951976	-76.06794328
daug-cc-pVQZ	-76.07479262	-76.07322153
daug-cc-pV5Z	-76.07609362	-76.07451872
mrchem	-76.07766927	-76.07575971
variational	-76.38690086	-76.20453544

Table A.10: Total energies for  $\text{H}_2\text{O}$  with molecular shaped cavity

Basis	$R = vdw * 1.2$	$R + 0.2$
cc-pVDZ	-129.05771485	-129.05081346
cc-pVTZ	-129.09602536	-129.08913108
cc-pVQZ	-129.10611331	-129.09925769
cc-pV5Z	-129.10825575	-129.10142747
aug-cc-pVDZ	-129.06402725	-129.05721593
aug-cc-pVTZ	-129.09702058	-129.09016851
aug-cc-pVQZ	-129.10636989	-129.09952705
aug-cc-pV5Z	-129.10829226	-129.10146332
daug-cc-pVDZ	-129.06486302	-129.05805796
daug-cc-pVTZ	-129.09756228	-129.09072176
daug-cc-pVQZ	-129.10644180	-129.09960328
daug-cc-pV5Z	-129.10829964	-129.10147033
mrchem	-129.11368615	-129.10627004
variational	-129.16283468	-129.13294308

Table A.11: Total energies for  $\text{NO}^+$  with molecular shaped cavity

Basis	$R = vdw * 1.2$	$R + 0.2$
cc-pVDZ	-92.41445816	-92.40992391
cc-pVTZ	-92.44769726	-92.44367546
cc-pVQZ	-92.45716524	-92.45344058
cc-pV5Z	-92.45953785	-92.45601357
aug-cc-pVDZ	-92.43512935	-92.43166729
aug-cc-pVTZ	-92.45354978	-92.45010599
aug-cc-pVQZ	-92.45889853	-92.45544029
aug-cc-pV5Z	-92.45996252	-92.45650057
daug-cc-pVDZ	-92.43548996	-92.43203218
daug-cc-pVTZ	-92.45370877	-92.45027272
daug-cc-pVQZ	-92.45891310	-92.45545650
daug-cc-pV5Z	-92.45996917	-92.45650576
mrchem	-92.46291128	N/A
variational	-95.40033415	-94.77304157

Table A.12: Total energies for  $\text{CN}^-$  with molecular shaped cavity

Basis	$R = vdw * 1.2$	Vdw+0.2
cc-pVDZ	-0.00881874	-0.00727889
cc-pVTZ	-0.00905358	-0.00745953
cc-pVQZ	-0.00904675	-0.00745758
cc-pV5Z	-0.00904362	-0.00746128
aug-cc-pVDZ	-0.00904491	-0.00746271
aug-cc-pVTZ	-0.00899134	-0.00741758
aug-cc-pVQZ	-0.00896485	-0.00739463
aug-cc-pV5Z	-0.00897029	-0.00739568
daug-cc-pVDZ	-0.00905495	-0.00746447
daug-cc-pVTZ	-0.00899654	-0.00742006
daug-cc-pVQZ	-0.00896847	-0.00739738
daug-cc-pV5Z	-0.00897112	-0.00739623
mrchem	-0.01038606	-0.00847650
variational	-0.31961766	-0.13725224

Table A.13: Reaction field energies for H<sub>2</sub>O with molecular shaped cavity

Basis	$R = vdw * 1.2$	Vdw +0.2
cc-pVDZ	-0.12928814	-0.12238674
cc-pVTZ	-0.12916234	-0.12226806
cc-pVQZ	-0.12908887	-0.12223324
cc-pV5Z	-0.12900377	-0.12217549
aug-cc-pVDZ	-0.12887447	-0.12206315
aug-cc-pVTZ	-0.12901516	-0.12216309
aug-cc-pVQZ	-0.12902757	-0.12218473
aug-cc-pV5Z	-0.12899823	-0.12216930
daug-cc-pVDZ	-0.12888719	-0.12208214
daug-cc-pVTZ	-0.12900294	-0.12216243
daug-cc-pVQZ	-0.12901808	-0.12217956
daug-cc-pV5Z	-0.12899910	-0.12216979
mrchem	-0.13411413	-0.12669802
variational	-0.18326265	-0.15337106

Table A.14: Reaction field energies for NO<sup>+</sup> with molecular shaped cavity

Basis	$R = vdw * 1.2$	Vdw + 0.2
cc-pVDZ	-0.11581532	-0.11128108
cc-pVTZ	-0.11421917	-0.11019738
cc-pVQZ	-0.11297662	-0.10925196
cc-pV5Z	-0.11175803	-0.10823375
aug-cc-pVDZ	-0.11087798	-0.10741592
aug-cc-pVTZ	-0.11093450	-0.10749072
aug-cc-pVQZ	-0.11094754	-0.10748930
aug-cc-pV5Z	-0.11097029	-0.10750835
daug-cc-pVDZ	-0.11099781	-0.10754003
daug-cc-pVTZ	-0.11094507	-0.10750902
daug-cc-pVQZ	-0.11094845	-0.10749185
daug-cc-pV5Z	-0.11097408	-0.10751067
mrchem	-0.11376103	N/A
variational	-3.05118390	-2.42389132

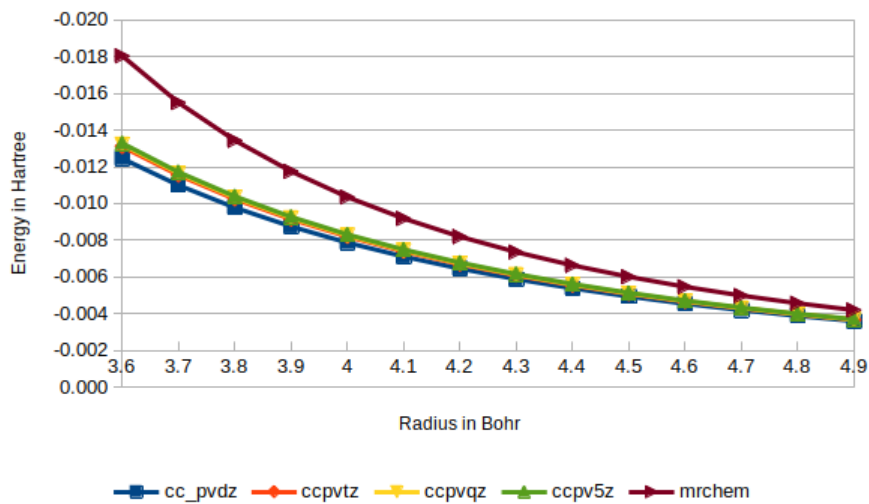
Table A.15: Reaction field energies for  $\text{CN}^-$  with molecular shaped cavity

Basis	$R = vdw * 1.2$	Vdw+0.2
cc-pVDZ	-0.01423889	-0.01198616
cc-pVTZ	-0.01505476	-0.01270038
cc-pVQZ	-0.01532129	-0.01295779
cc-pV5Z	-0.01537378	-0.01301139
aug-cc-pVDZ	-0.01550232	-0.01310493
aug-cc-pVTZ	-0.01538995	-0.01302900
aug-cc-pVQZ	-0.01535152	-0.01299593
aug-cc-pV5Z	-0.01535415	-0.01299338
daug-cc-pVDZ	-0.01544577	-0.01305028
daug-cc-pVTZ	-0.01537421	-0.01301212
daug-cc-pVQZ	-0.01535340	-0.01299585
daug-cc-pV5Z	N/A	N/A
mrchem	-0.01749631	-0.01461535
variational	-2.69241073	-1.76175275

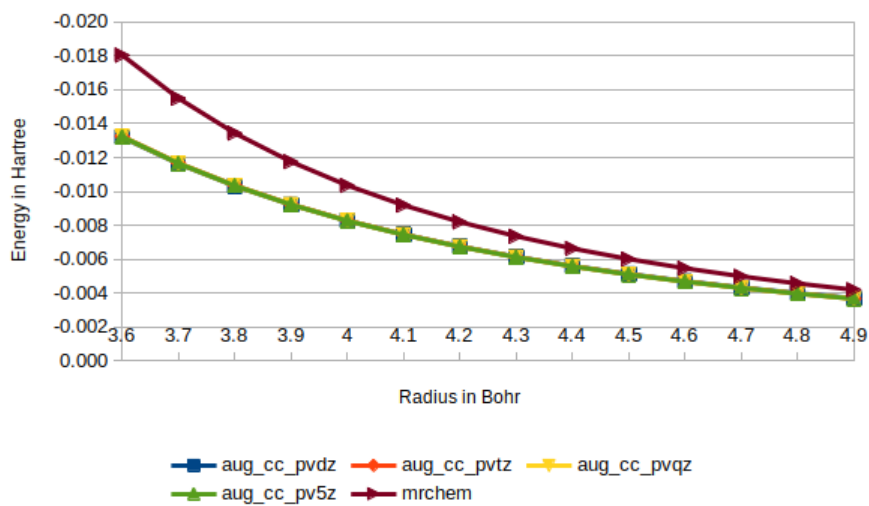
Table A.16: Reaction field energies for  $\text{CH}_3\text{CONH}_2$  with molecular shaped cavity

# Appendix B

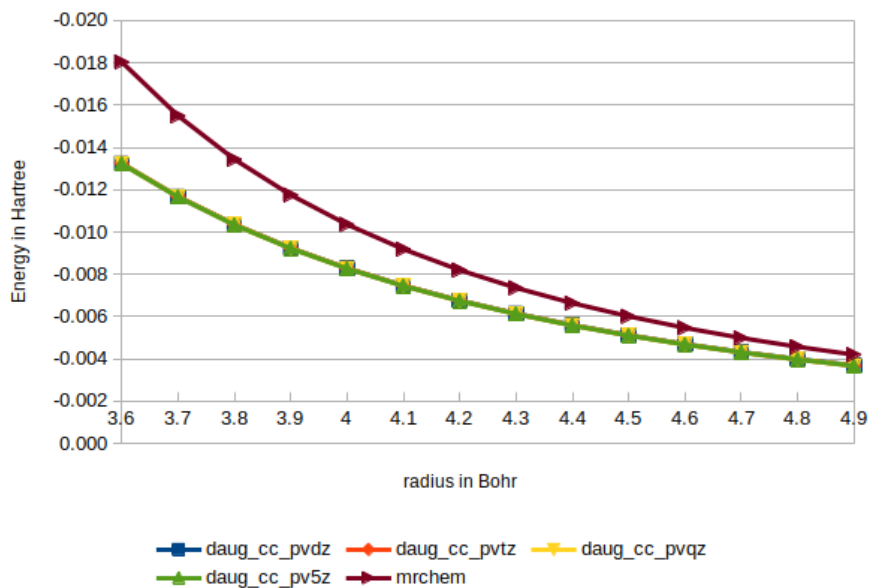
## Test Figures



(a) MRCHEM against normal basis sets

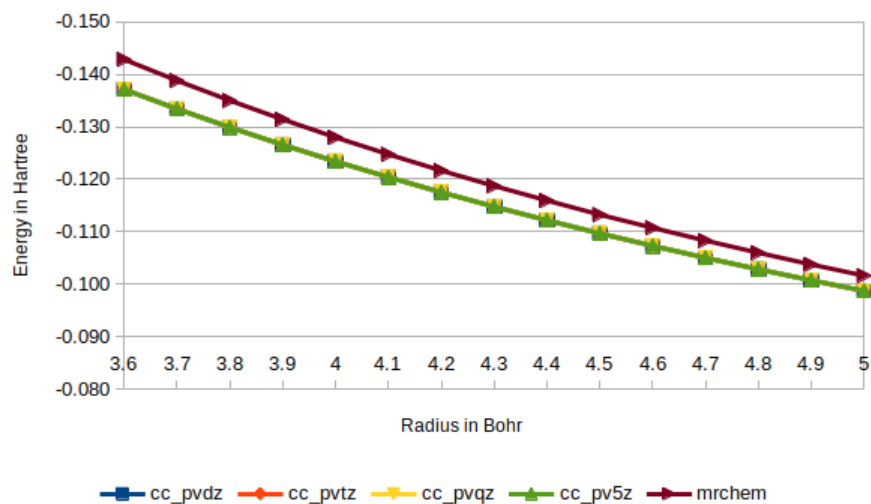


(b) MRCHEM against augmented basis sets

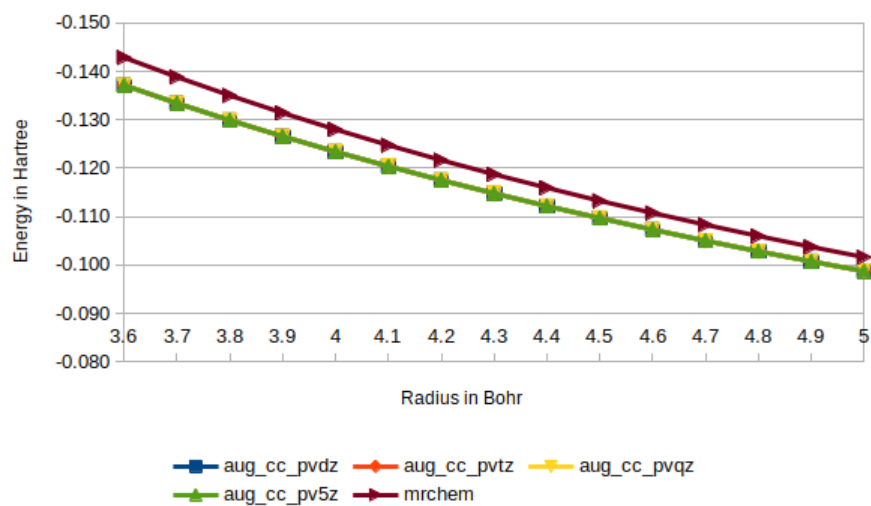


(c) MRCHEM against double augmented augmented basis sets

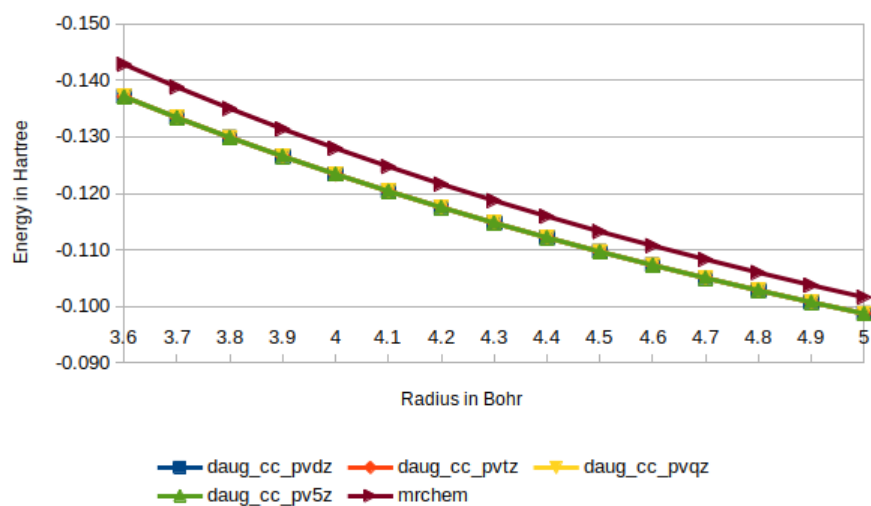
Figure B.1: Reaction field energy of H<sub>2</sub>O in a water solution, calculated with relative precision  $e - 05$  in MRCHEM and with different basis sets in Gaussian



(a) MRCHEM against normal basis sets

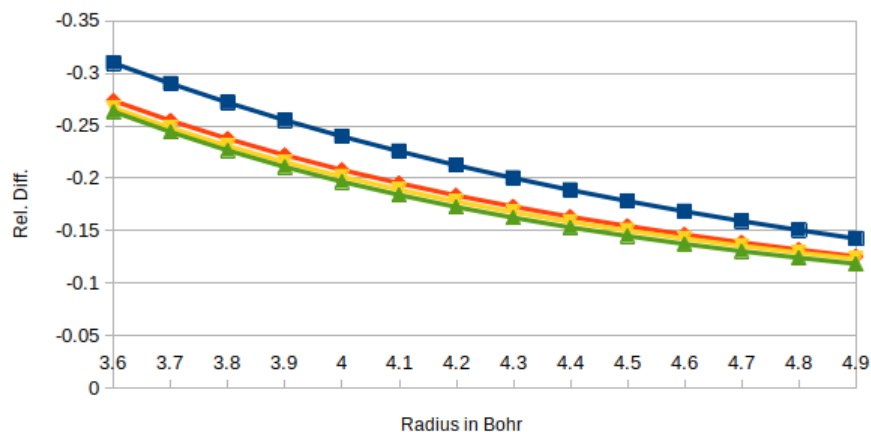


(b) MRCHEM against augmented basis sets

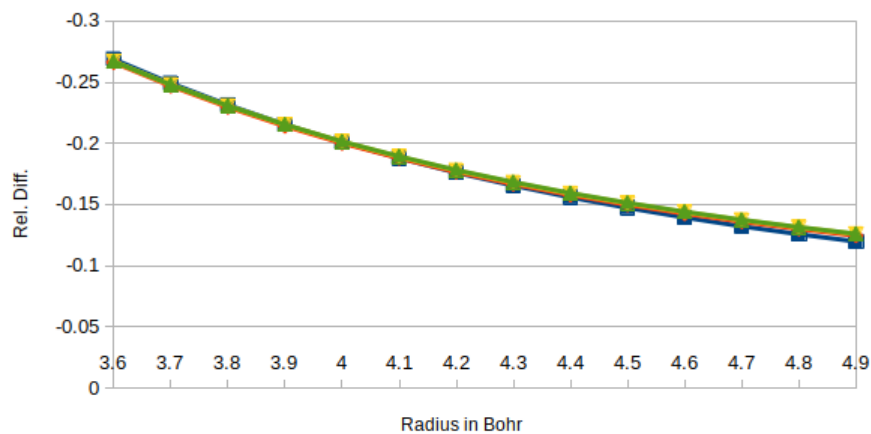


(c) MRCHEM against double augmented augmented basis sets

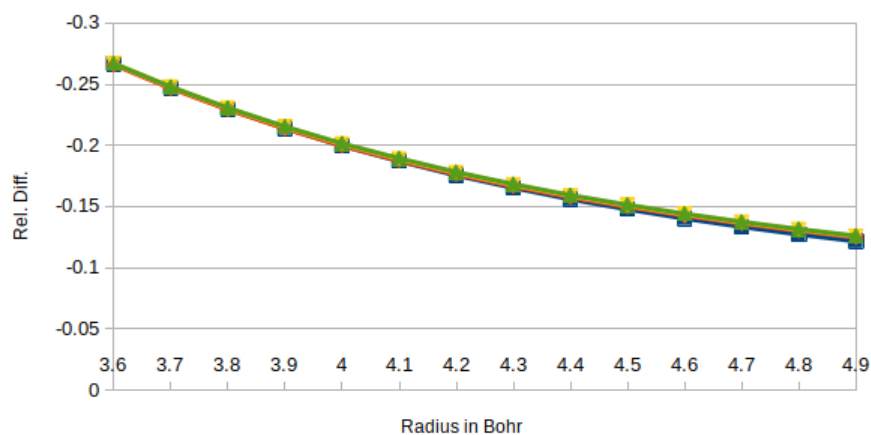
Figure B.2: Reaction field energy of  $\text{Li}^+$  in a water solution, calculated with relative precision  $e - 05$  in MRCHEM and with different basis sets in Gaussian



(a) MRCHEM against normal basis sets



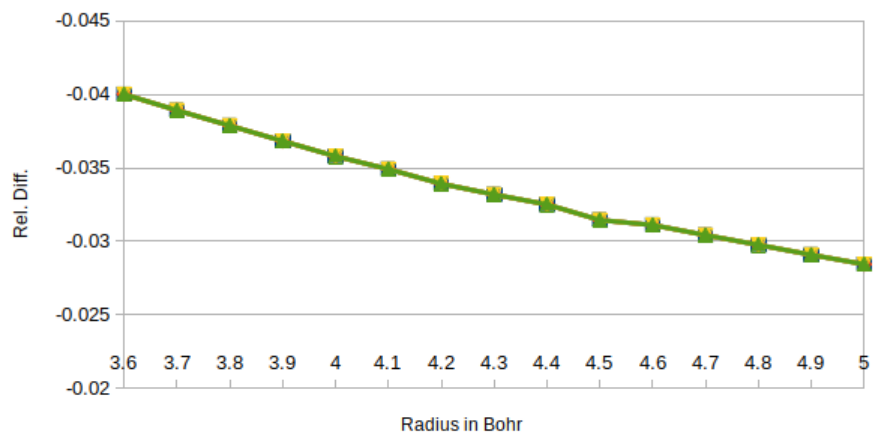
(b) MRCHEM against augmented basis sets



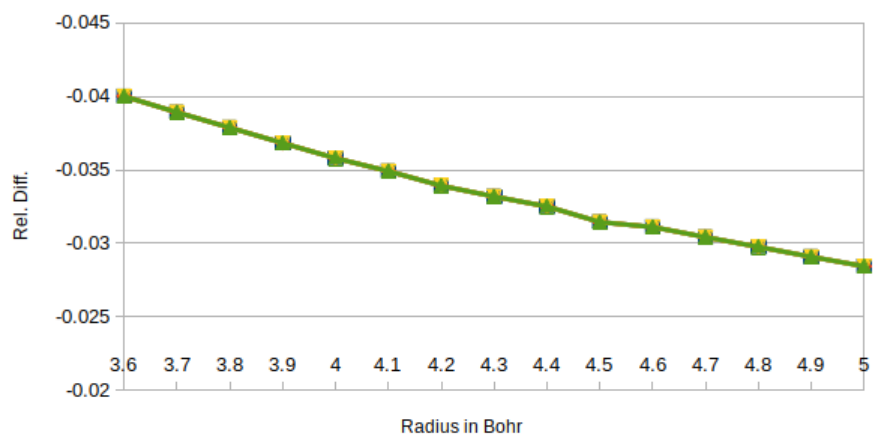
(c) MRCHEM against double augmented augmented basis sets

Figure B.3: Relative difference between the Reaction field energy of  $\text{H}_2\text{O}$  in a water solution calculated with with relative precision  $e - 05$  in MRCHEM and with different basis sets in Gaussian

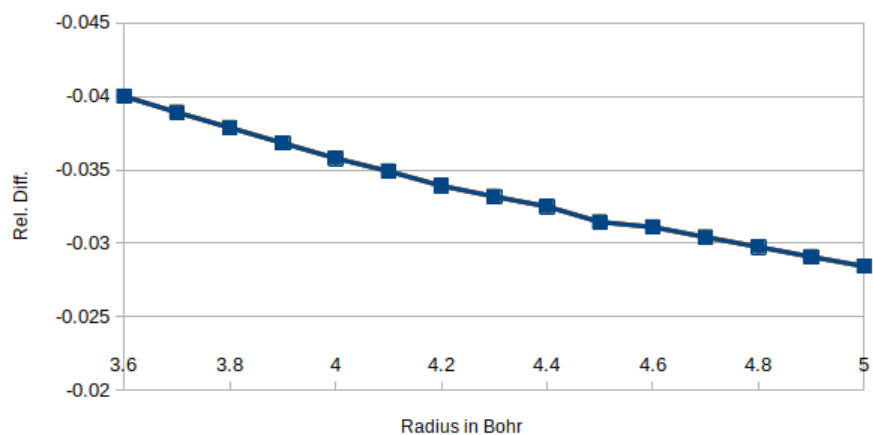




(a) MRCHEM against normal basis sets

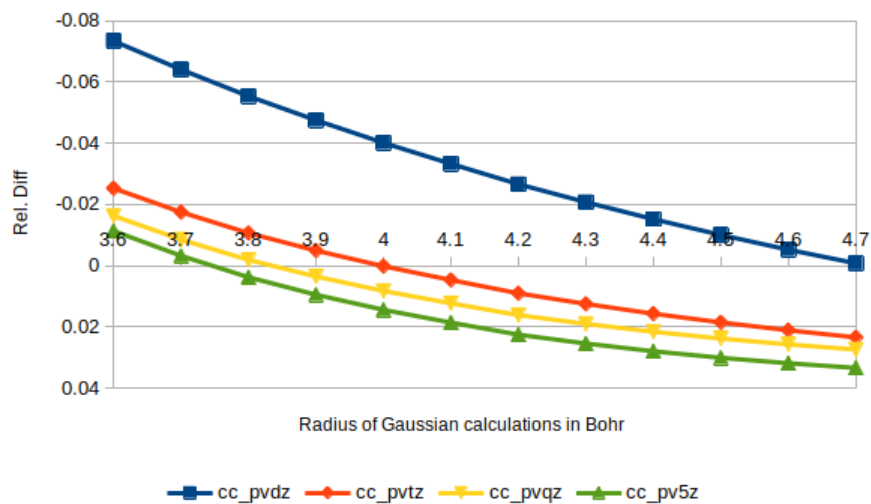


(b) MRCHEM against augmented basis sets

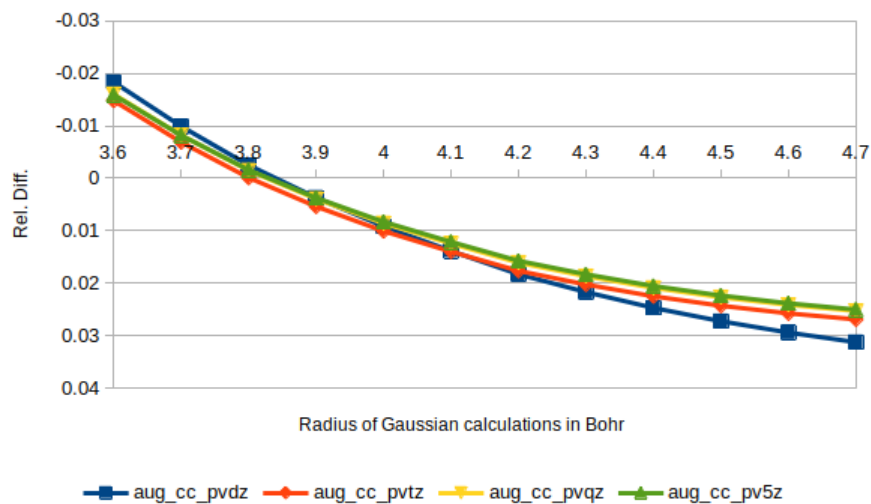


(c) MRCHEM against double augmented augmented basis sets

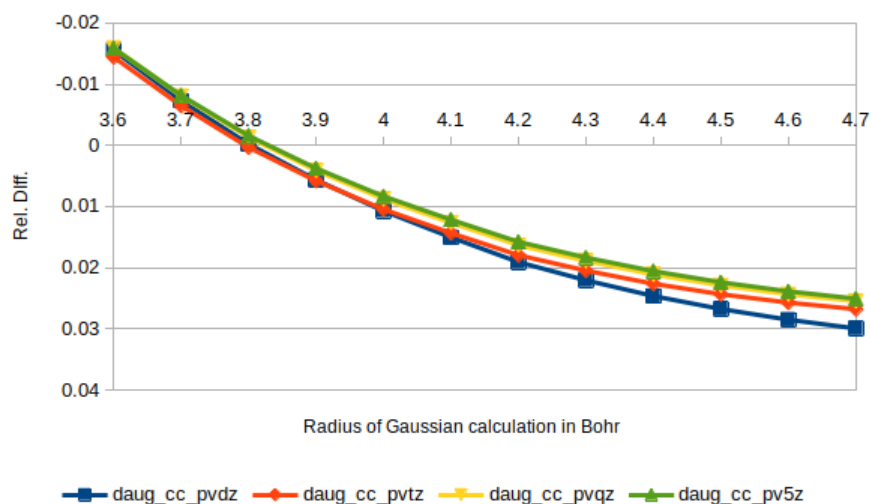
Figure B.4: Relative difference between the Reaction field energy of  $\text{Li}^+$  in a water solution calculated with relative precision  $e - 05$  in MRCHEM and with different basis sets in Gaussian



(a) MRCHEM against normal basis sets

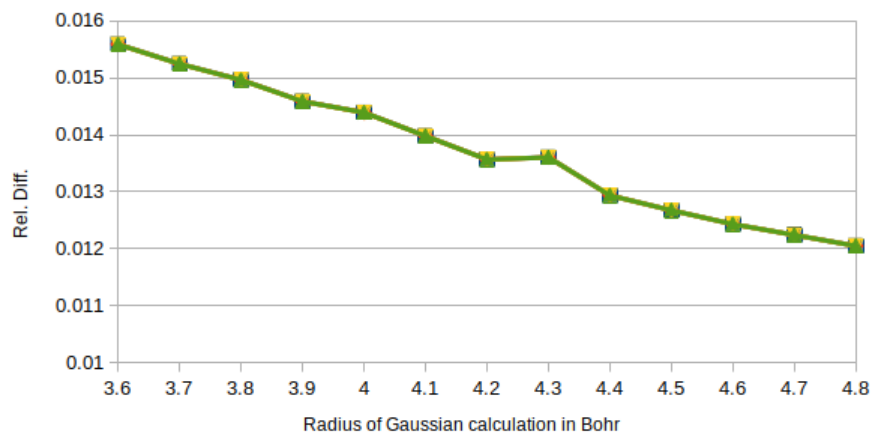


(b) MRCHEM against augmented basis sets

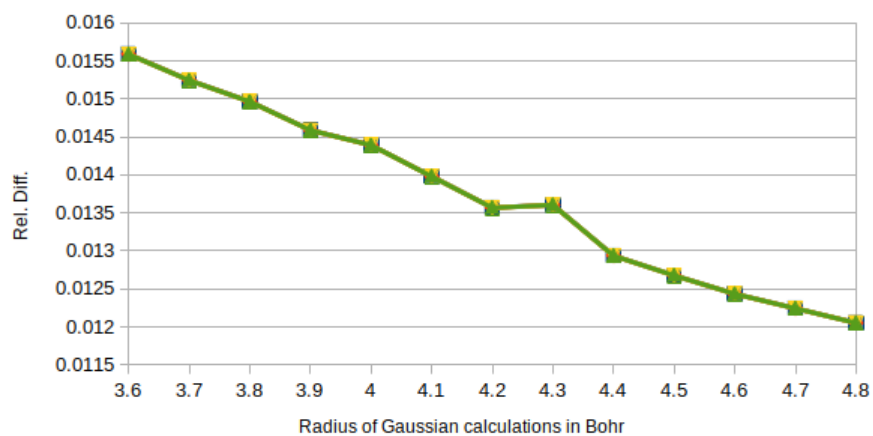


(c) MRCHEM against double augmented augmented basis sets

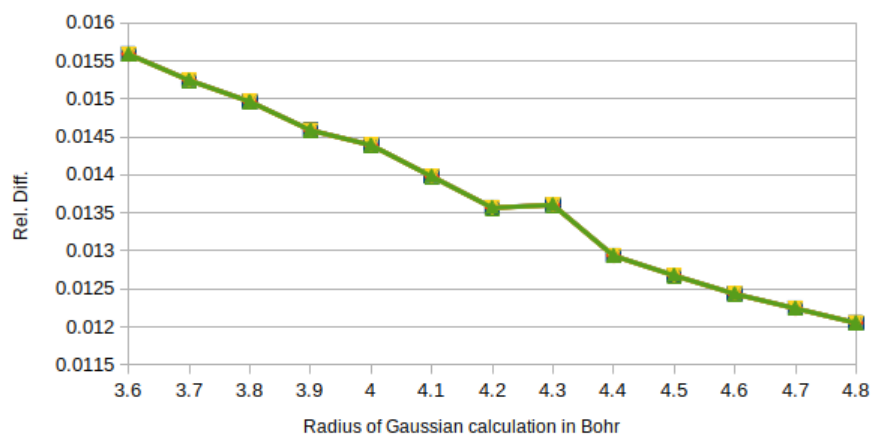
Figure B.5: Relative difference between the Reaction field energy of  $\text{H}_2\text{O}$ ] with a shifted radius by 0.2 Bohr in a water solution calculated with with relative precision  $e - 05$  in MRCHEM and with different basis sets in Gaussian



(a) MRCHEM against normal basis sets

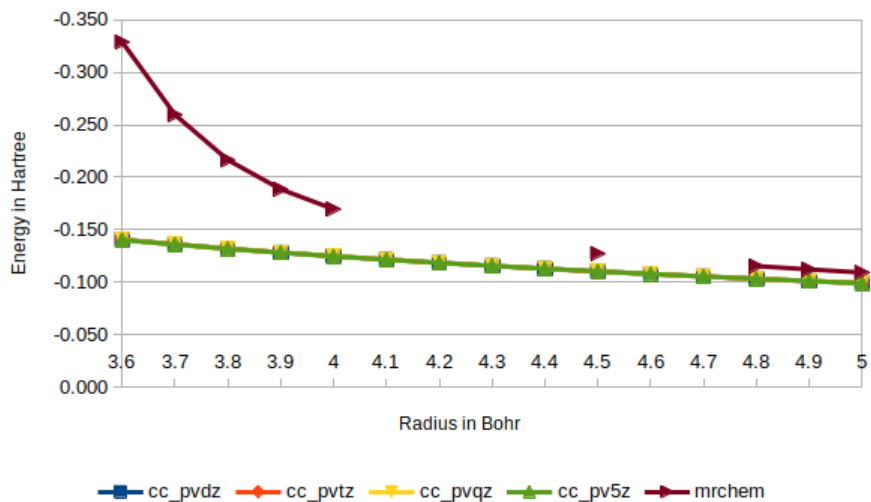


(b) MRCHEM against augmented basis sets

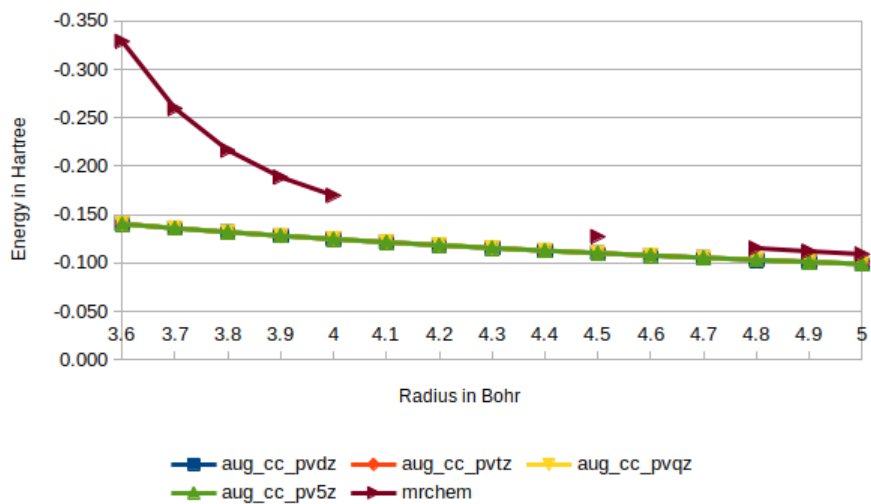


(c) MRCHEM against double augmented augmented basis sets

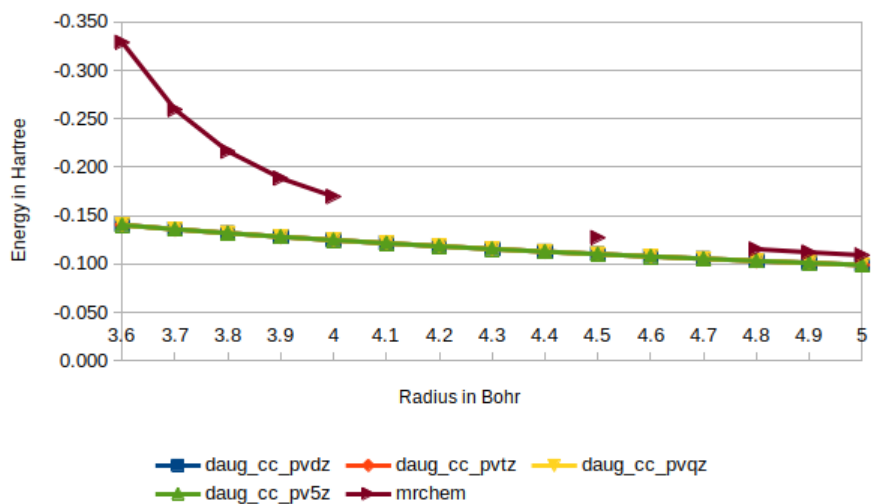
Figure B.6: Relative difference between the Reaction field energy of  $\text{Li}^+$  with a shifted radius by 0.2 Bohr in a water solution calculated with relative precision  $e - 05$  in MRCHEM and with different basis sets in Gaussian



(a) MRCHEM against normal basis sets

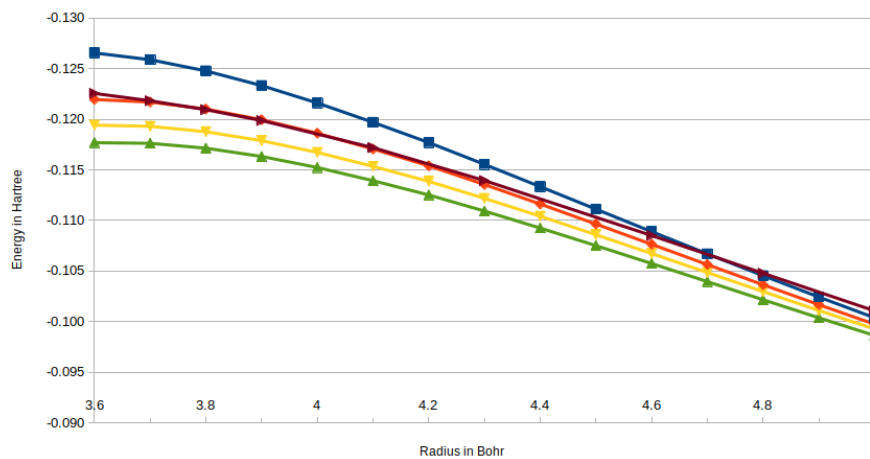


(b) MRCHEM against augmented basis sets

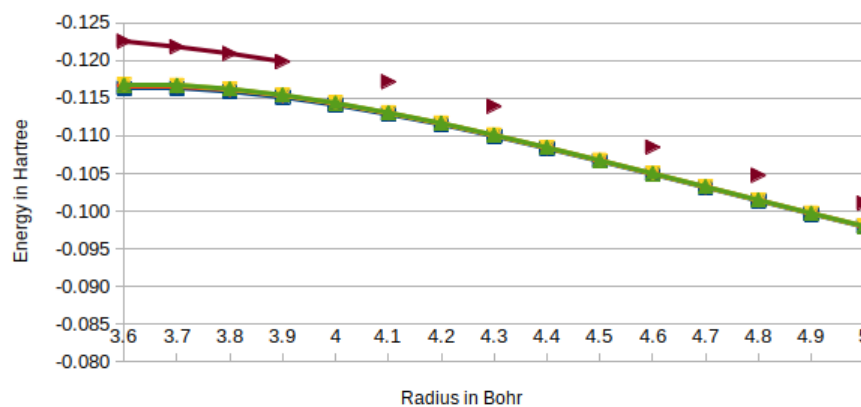


(c) MRCHEM against double augmented augmented basis sets

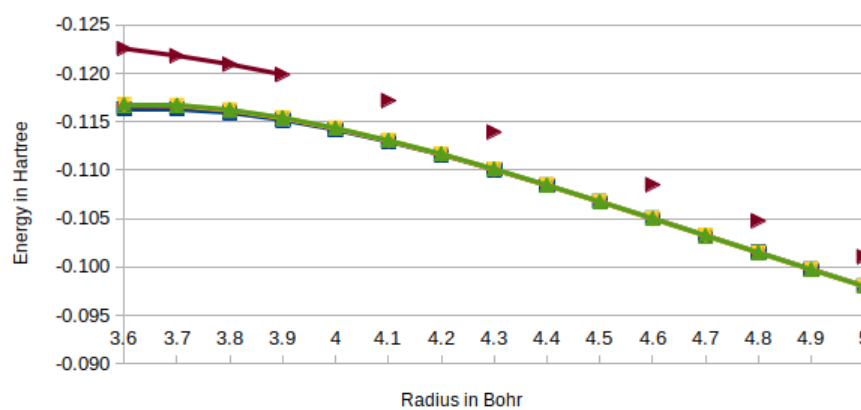
Figure B.7: Reaction field energy of  $\text{NO}^+$  in a water solution, calculated with MRCHEM and with different basis sets in Gaussian



(a) MRCHEM against normal basis sets

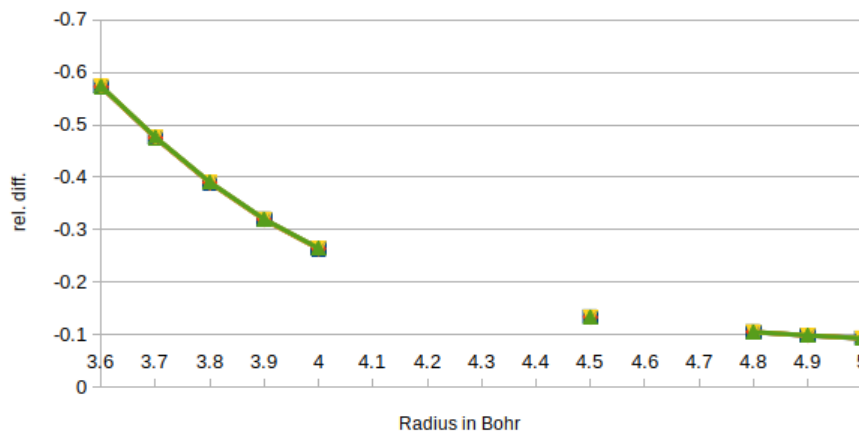


(b) MRCHEM against augmented basis sets

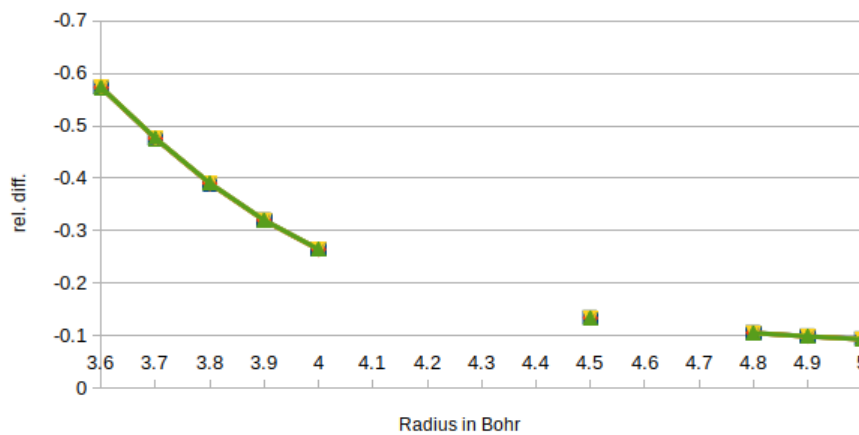


(c) MRCHEM against double augmented augmented basis sets

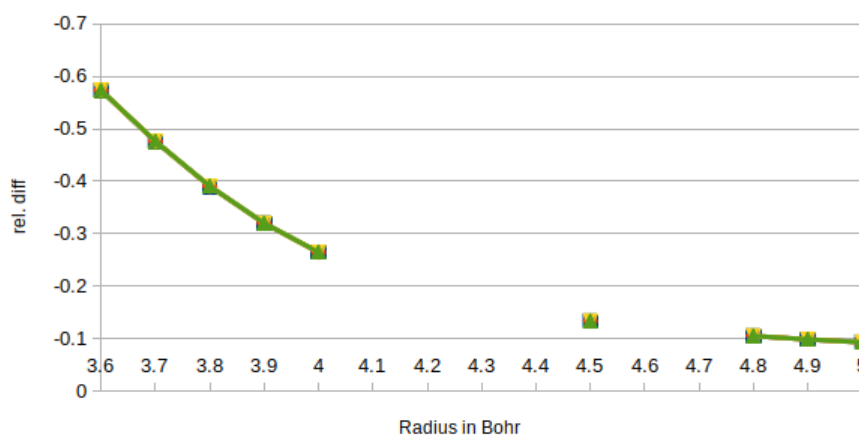
Figure B.8: Reaction field energy of  $\text{CN}^-$  in a water solution, calculated with MRCHEM and with different basis sets in Gaussian



(a) MRCHEM against normal basis sets

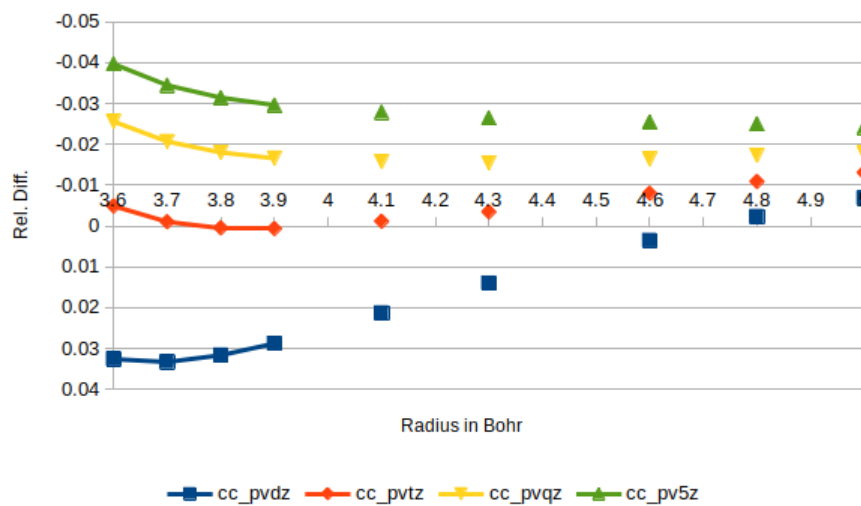


(b) MRCHEM against augmented basis sets

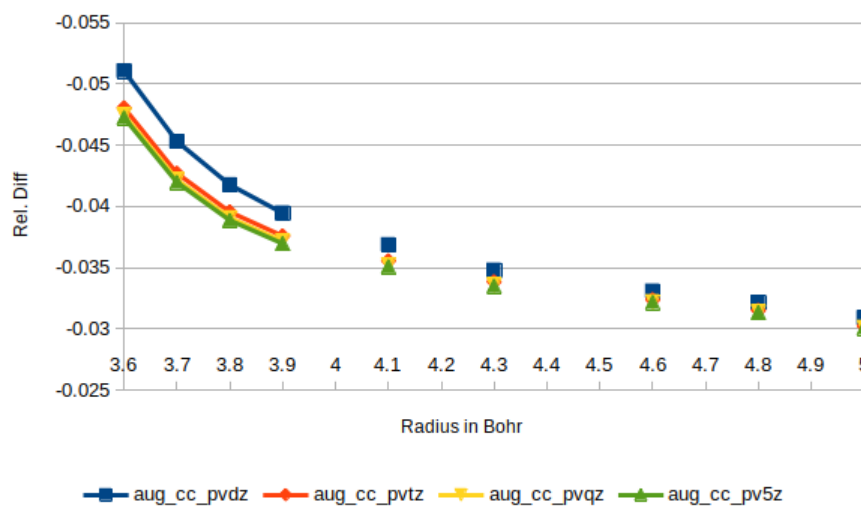


(c) MRCHEM against double augmented augmented basis sets

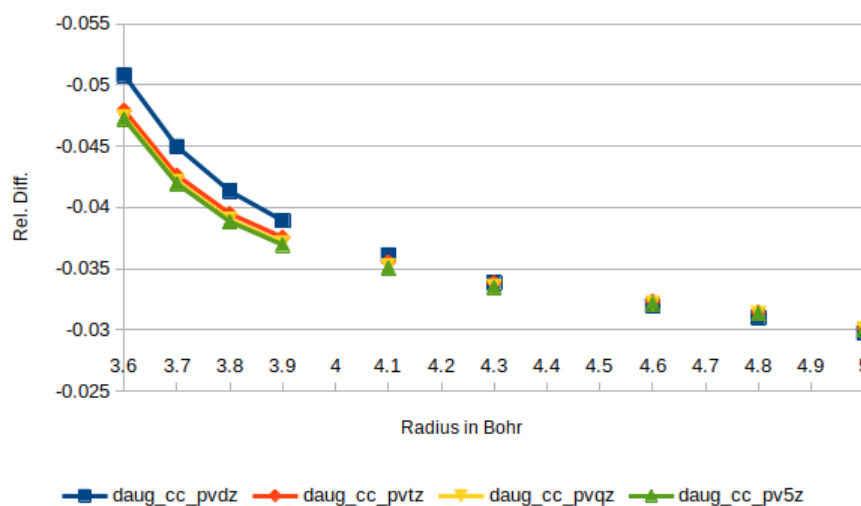
Figure B.9: Relative difference between the Reaction field energy of  $\text{NO}^+$  in a water solution calculated with MRCHEM and with different basis sets in Gaussian



(a) MRCHEM against normal basis sets



(b) MRCHEM against augmented basis sets



(c) MRCHEM against double augmented augmented basis sets

Figure B.10: Relative difference between the Reaction field energy of  $\text{CN}^-$  in a water solution calculated with MRCHEM and with different basis sets in Gaussian